

TNO Defence Research

AD-A266 837



TNO-report

PML 1991-28

January 1993

Copy no.: 1.0

TNO Prins Maurits Laboratory

Lange Klerweg 137
P O Box 45
2280 AA Rijswijk
The Netherlands

Fax +31 15 84 39 91
Telephone +31 15 84 28 42

TD 91-1682 II

An experimental and analytical study on the
penetration of rods into ceramic faced
armours



TDCK RAPPORTCENTRALE

Frederikkazerne, gebouw 140
v/d Burchlaan 31 MPC 16A
TEL. : 070-3166394/6395
FAX. : (31) 070-3166202
Postbus 90701
2509 LS Den Haag



DTIC
ELECTE
S JUL 14 1993 D
A

This document has been approved
for public release and sale; its
distribution is unlimited

All rights reserved.
No part of this publication may be
reproduced and/or published by print,
photoprint, microfilm or any other means
without the previous written consent of
TNO.

In case this report was drafted on
instructions, the rights and obligations of
contracting parties are subject to either the
'Standard Conditions for Research
Instructions given to TNO', or the relevant
agreement concluded between the
contracting parties.
Submitting the report for inspection to
parties who have a direct interest is
permitted.

TNO

93-15906



Netherlands organization for
applied scientific research

TNO Defence Research consists of
the TNO Physics and Electronics Laboratory,
the TNO Prins Maurits Laboratory and the
TNO Institute for Perception.



Author(s):

Paul C. den Reijer

DO-assignment no.

Classification

Report:

ONGERUBRICEERD

Title:

ONGERUBRICEERD

Summary:

ONGERUBRICEERD

Annex(es):

ANNEXES A-C: ONGERUBRICEERD

Number of copies:

25

Number of pages:

(incl. annex(es), excl. distr. list and RDP)

103

Number of Annexes:

3

The classification designation:

ONGERUBRICEERD

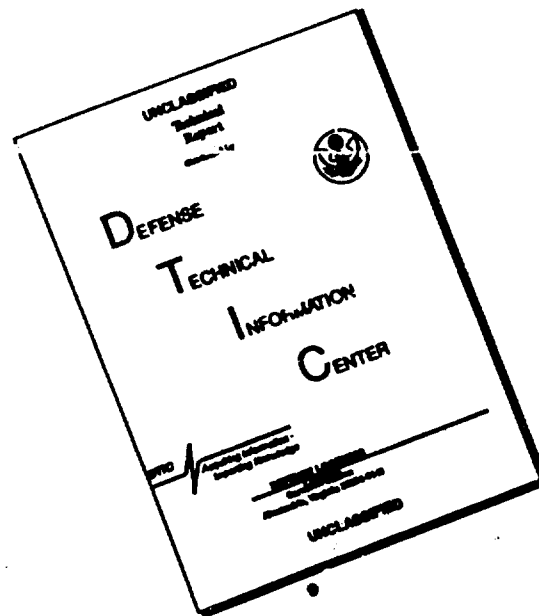
is equivalent to:

UNCLASSIFIED

All information which is classified according to Dutch regulations shall be
treated by the recipient in the same way as classified information of
corresponding value in his own country.

1 of this information may be disclosed to any party

DISCLAIMER NOTICE



THIS DOCUMENT IS BEST
QUALITY AVAILABLE. THE COPY
FURNISHED TO DTIC CONTAINED
A SIGNIFICANT NUMBER OF
PAGES WHICH DO NOT
REPRODUCE LEGIBLY.

Summary

AKZO's ballistic Arall programme has led to the development of an analytic lightweight armour response model (ALARM) which can be used to predict the behaviour of these armour systems when impacted by various projectiles. In order to verify and improve the understanding of phenomena governing the projectile/armour interaction process, an experimental programme was proposed and set up.

This report deals with the second and final phase of this programme. The impact of steel rod projectiles into four types of ceramic faced armours with velocities above and below the armour's ballistic limit velocity is studied using a flash X-ray technique. The experimental results are discussed extensively and compared with the ALARM model predictions. Recommendations for future improvement of the analytic model and for experimental research on ceramic faced armours are presented too.

Samenvatting

Ten behoeve van AKZO's ballistisch Arall programma is bij het PML een analytisch penetratiemodel ontwikkeld. Dit zogenaamde "Analytic Lightweight Armour Response Model (ALARM)" kan gebruikt worden om het gedrag van keramische pantsersystemen na inslag van een projectiel te voorspellen. Om de kennis aangaande het penetratieproces van projectielen in keramische pantsers te verifiëren en vergroten is een experimenteel programma opgezet.

Dit rapport handelt over de tweede en tevens laatste fase van dit programma. Het penetratieproces van stalen staaf projectielen in een viertal typen keramische pantsers is bestudeerd met behulp van een röntgenflitsmethode. De experimentele resultaten worden geanalyseerd, besproken en vergeleken met voorspellingen van het ALARM-model. Aanbevelingen voor verbetering van het analytische model en voor toekomstig experimenteel onderzoek aan keramische pantsers worden tevens gepresenteerd.

DTIC QUALITY INSPECTED 5

Accession For	
NTIS	CRA&I <input checked="" type="checkbox"/>
DTIC	TAB <input type="checkbox"/>
Unannounced <input type="checkbox"/>	
Justification	
By	
Distribution	
Availability Code	
Dist	Avail and/or Special
A-1	

CONTENTS

	SUMMARY/SAMENVATTING	2
	CONTENTS	3
1	INTRODUCTION	5
2	OBJECTIVES OF THE EXPERIMENTAL PROGRAMME	7
3	THE EXPERIMENTAL SET-UP	8
3.1	Introduction	8
3.2	The projectile: a blunt circular cylindrical rod	9
3.3	The rod-acceleration technique	10
3.4	The armour panels	11
3.5	The flash X-ray set-up	12
3.6	Triggering of the flash X-ray pulsers and velocity measurement	13
4	THE EXPERIMENTAL RESULTS	14
4.1	Introduction	14
4.2	Armours of 8.1 mm alumina and 6.0 mm aluminium	14
4.3	Armours of 8.1 mm alumina and a package of two 3.0 mm thick layers of aluminium	16
4.4	Armours of 8.1 mm alumina and 4.0 mm aluminium	17
4.5	Armours of 8.1 mm alumina and 8.0 mm aluminium	18
5	ANALYSIS OF THE EXPERIMENT RESULTS	19
5.1	Introduction	19
5.2	The behaviour of the ceramic facing during impact	19
5.3	The behaviour of the back-up plates during impact	22
5.4	The behaviour of the projectile during impact	24
5.5	The blunt steel rod as a simulator of the 7.62 mm AP projectile	25

6	ANALYTIC MODEL SIMULATIONS	26
6.1	Introduction	26
6.2	The ALARM model input parameters	27
6.3	ALARM simulation versus experiment	28
6.4	Discussion	30
7	CONCLUSION	32
8	RECOMMENDATIONS	33
9	AUTHENTICATION	35
10	REFERENCES	36
11	TABLES	41
12	FIGURES	43
ANNEX A	MATERIAL PROPERTIES OF ETG-100, HILOX-973 AND AL6061-T6	
ANNEX B	THE EXPERIMENT DATA AND CONSTANTS OF POLYNOMIALS	
ANNEX C	THE COMPLETE SET OF ALARM INPUT PARAMETERS	

1 INTRODUCTION

When ceramic tiles are used as overlays or incorporated as a layer between conventional armour materials, the ballistic protection is significantly enhanced^[1-5].

This finding has encouraged the use of ceramics as a component in armours and has resulted in some attention from the scientific community^[6-19]. The work of Wilkins and his colleagues is by far the most comprehensive research in the field, covering both experimental and theoretical studies on the relative effectiveness of various ceramics against armour piercing projectiles^[13-19].

The design of ceramic armour systems has been based predominantly on empirical ballistic performance data. However, the most fruitful results can be expected when the experiments are supplemented by an analytical approach, which includes the dynamic mechanisms accounting for the behaviour of these armours. The advantage of an analytic approach, over the use of empirical models, scaling procedures and hydrocode computations, is easily advocated. Empirical models need to be supported by a huge amount of experimental data in order to be able to accurately predict ballistic limit velocities (V_{50} s) of specific armour and projectile configurations. More detailed information than the V_{50} cannot easily be supplied by such models. By use of geometric-scaling, empirical models become more versatile, although such procedures do not allow the projectile geometry, armour geometry, armour composition or impact velocity to be varied independently. Hydrocode simulations have the potential of providing the most detailed information on the progress of a penetration process^[20-21]. Unfortunately, these computations are extremely time-consuming. An enormous effort to develop brittle material response models for use within hydrocodes is still being pursued at many laboratories^[22-25]. The tuning of the code predictions with experimental data is therefore still necessary. The long CPU execution times make the use of hydrocodes for parameter studies and ballistic limit velocity computations impractical to engineers in the development process of protective materials.

An analytic model requires only a limited amount of experimental data, yet is able to present the user with details of the penetration process in addition to the prediction of the ballistic limit velocity. The use of an analytic model allows a user to conduct parameter studies by varying projectile and armour composition, geometry and materials completely independently, without the immediate necessity to support this by experimental data.

Unfortunately, only very few analytic penetration models for armours with brittle facings have been published in the literature^[9, 26-28]. In 1987, the Prins Maurits Laboratory received an

assignment from AKZO and the Dutch Ministry of Defence to develop an analytic penetration model for ceramic faced armours. This penetration model was named ALARM (Analytic Lightweight Armour Response Model)[29-33]. It can predict the ballistic limit velocity of ceramic faced armours with (laminated) metal back-up plates. It also presents the user with details of the penetration process. The model has proven successful in aiding engineers to optimize armour concepts. The exercises carried out with the ALARM model in refs. [30] and [33], together with the results presented in this report, illustrate the potential of this model.

In order to improve and verify the behaviour predicted by the model, an experimental programme was proposed and awarded. The programme was intended to generate experimental data on the projectile/armour interaction process throughout the impact event. In the first phase of this programme, of which the results have been presented in refs. [34] and [35], the penetration process in ceramic faced armours of standard 7.62 mm armour piercing (AP) and Ball projectiles was studied, using a newly developed flash X-ray technique. Valuable information was obtained on the behaviour of the armour and the projectiles. The novel flash X-ray technique, essential to visualize the projectile/armour interaction process, proved to work satisfactorily. As was expected, the complex geometry and material composition of these projectiles prevented a detailed comparison of the results with the behaviour predicted by the model.

This report presents the results from the second and final phase of the programme. The penetration behaviour of blunt steel rods shot into ceramic faced armours with velocities above and below the armour's ballistic limit velocity is studied using the aforementioned experimental technique. The geometry and material composition of the steel rod was selected such that the rod's penetration capability resembled that of the 7.62 mm AP projectile. The experimental results are analysed and discussed in some detail, revealing the important mechanisms by which these armours and projectiles are defeated.

ALARM model simulations have been carried out in order to allow detailed comparison with the experimental data. The discrepancies between the ALARM model predictions and the experimental data are discussed and analysed.

2 OBJECTIVES OF THE EXPERIMENTAL PROGRAMME

Until now the predictions by the ALARM model could only be compared to experimental results based on the ballistic limit velocity data. The armour and projectile geometry and material composition in experiments reported on in literature were either too complex or unknown, preventing their use for detailed comparison with ALARM predictions. Wilkins' progress reports are the only available in open literature which show details of the projectile/armour interaction process. Unfortunately, some of these data contradict themselves, rendering them of limited value for our purposes [16, 36]. In order to further improve and validate the ALARM model, detailed data on projectile mass erosion, armour penetration and deformation throughout the impact process are necessary.

In experimenting, one generally prefers to repeat tests several times in order to reduce scatter and improve the accuracy of the results. However, the lack of detailed test data in literature and the limited resources available to this programme have caused us to prefer an extended broad experimental programme, above a limited programme with a higher accuracy. The objective of the series of experiments reported here was, therefore, to create a reliable data-base describing projectile and armour response to high velocity rod impact for a number of armour configurations.

The use of simple geometry, blunt circular-cylindrical rods and alumina-aluminium targets, allows the generated data to be easily used for comparison with analytic models and hydrocode simulations.

As the ALARM model was developed to predict the behaviour of small calibre (armour piercing) projectiles, such as the 7.62 mm AP, the rods should inflict a comparable response on the target. In order to ascertain the same time-scale of events and magnitude of stress in the target, the impact velocities of the rods were required to be close to those for the standard projectiles, typically some 840 m/s.

The rod and armour responses were monitored throughout the first 60 μ s of the impact event. This time-span covers the most interesting period of the projectile/armour interaction process.

An alumina-aluminium ceramic faced armour (8.1 mm Morgan Matroc Hilox 973 & 6.0 mm AL6061-T6), weighing 47 kg/m², just defeats the 7.62 mm AP projectile with muzzle velocity (840 m/s). This armour was used in this study as a base-line reference. The rods were also fired at a concept with two 3.0 mm thick layers of aluminium 6061-T6 instead of the single 6.0 mm thick layer. According to literature [50], the two-layer back-up plate, which has a four-times lower

bending stiffness than the single 6.0 mm thick back-up plate, would cause the armour's ballistic limit velocity to decrease by almost 100 m/s. Since the armour with the 6.0 mm thick aluminium 6061-T6 back-up plate was designed such that its ballistic limit velocity lies slightly above the 7.62 mm AP projectile's muzzle velocity (840 m/s), the armour with the double back-up plate was expected to be defeated by the rod. This presented the possibility to study projectile defeat and perforation at identical projectile velocity and armour areal density.

Experiments were also carried out with 8.1 mm thick ceramic facings supported by heavier, 8.0 mm thick, and lighter, 4.0 mm thick back-up plates. The thick back-up plate gives optimal support to the comminuted ceramic inside the ceramic conoid. The thin back-up plate cannot support the ceramic facing very well, but deforms and absorbs energy easily. Based on Wilkins' observations^[16], it is expected that the failure modes of these back-up plates differ. Hence, including armours with these back-up plates to the programme allowed study of the apparent differences in the projectile/armour interaction processes which are caused by these different back-up plates. In order to obtain a complete overview of the projectile/armour interaction process with these armours, the rods were fired into them with velocities just above and below their ballistic limit velocities.

3 THE EXPERIMENTAL SET-UP

3.1 Introduction

The geometry and material of the blunt rod selected in order to give it the required penetration properties (comparable to the 7.62 mm AP) are presented in this chapter. In addition, the acceleration technique is described which has been developed to let the projectile impact the armour within the specified velocity range (700 m/s-1100 m/s). The armour panel composition and manufacturing process are disclosed as well.

A flash X-ray radiography technique^[37] was used to obtain information on the penetration process. Customarily, flash X-ray pulsers are set up in plane with the armour's front surface (normal to the projectile's line of flight). When the X-ray source is strong enough to radiate through the armour (side to side), the resulting radiograph presents information regarding projectile rear-end position, projectile tip position, armour deformation and projectile mass erosion. However, due to the limited penetration power of a 600 kV flash X-ray system, the lateral dimensions of an alumina faced ceramic armour panel then have to be reduced to approximately 50 mm. In certain situations this resulted in an unwanted depreciated performance of the armour panel. Therefore, an alternative flash X-ray technique was developed^[34, 35]. This flash X-ray technique does not limit the armour's lateral dimensions.

The experimental set-up, together with the triggering and velocity measurement schemes are presented in this chapter too.

3.2 The projectile: a blunt circular cylindrical rod

The simple geometry and material composition of the rod, when compared to the standard 7.62 mm AP projectile, allowed the generated test data to be used easily for comparison with ALARM model predictions.

The selection procedure of the rods was based on its fulfilment of a number of requirements. The rod is required to have similar penetration capabilities as the 7.62 mm AP projectile. The 7.62 mm AP projectile consists of a hard steel ($R_C = 60$) ogive-nosed core, followed by a lead plug and is surrounded by a tombac jacket. The ogive-nosed projectile has a maximum diameter of 7.62 mm and is 32.0 mm long. It weighs 9.55 grams. In order to ascertain the same time-scale of events and magnitude of stress in the target, the impact velocity of the rod was required to be close to that of the standard projectile, typically some 840 m/s. The rod's length-over-diameter ratio had to be slightly higher than the 7.62 mm AP's ratio. This facilitated the determination of the projectile mass-erosion during the impact process. In order to reduce projectile-originated scatter in the experimental results, high strength steel alloys were rejected for use. These alloys are often very brittle which may result in unpredictable break-up during impact, and thus scatter with respect to the ballistic performance.

Ballistic impact experiments with various rods resulted in the selection of a rod. This rod weighs 7.0 grams, has a 6.0 mm diameter and is 31.5 mm long ($L/D = 5.3$). This rod is manufactured from steel (ETG-100 von Moos Stahl AG Luzern; $R_C = 28$). The quasi-static material properties of ETG-100 are presented in Annex A. Figure 1 shows the steel rod together with the 7.62 mm AP projectile.

Support for the selection of the 6 mm diameter rod was obtained by Van Zuidam^[38]. Using streak-photography he measured the maximum back-up plate deformation profiles of ceramic faced armours when impacted by various projectiles. The ceramic armours in his study consisted of a 10.0 mm alumina facing supported by 4.0 mm aluminium 6061-T6. Aside from the 7.62 mm AP projectile, blunt steel rods with 5 mm, 6 mm, 7 mm, and 8 mm diameters, all weighing seven grams, were fired at the armours at approximately 820 m/s. Figure 2 comprises the results of these experiments. The back-up plate response resulting from the 6 mm diameter rod impact follows the response caused by the 7.62 mm AP projectile almost completely.

3.3 The rod-acceleration technique

The weight and length-over-diameter ratio of the rod prevent its successful acceleration to the velocity-range of 700 m/s to 1100 m/s using a conventional full bore launch-tube. The highest allowable pressure in the launch-tube acting on the rear cross-section of the rod is not high enough to accelerate it to these velocities. The rod can be accelerated to higher velocities by increasing the rear cross-sectional area of the rod, using a lightweight sabot and a launch-tube with a larger bore diameter. Hence, in this study the rod/sabot packages were launched from a 13.0 mm diameter smooth bore launch-tube.

Slender blunt rods travelling through air at supersonic velocities do not have a stable flight behaviour. The projectile will soon start to yaw due to small disturbances. Without changing the geometry of the projectile, this can only be prevented by either spinning the projectile or by placing the target as close as possible to the launch-tube's muzzle. Spinning the projectile during launch was rejected for use within this programme. Hence, the target had to be placed close to the launch-tube. This, however, required that the sabot discards from the rod immediately after the rod/sabot package leaves the muzzle of the launch-tube, otherwise the sabot will impact the target soon after the rod, ruining the test results.

A four component sabot was developed at PML for this purpose. This sabot uses an aerodynamic separation technique. The package is presented in Figure 3, and consists of two fingers and a split obturator. A female conical air-scoop is added at the forward end. The ram air pressure produced by the sabot's travel through the air is contained by the cone and produces an outward directed force which causes the sabot to first pivot around its rear corners and then separate from the central rod. The sabot segments then tumble and fly away from the rod as the ensemble travels downrange. The split obturator, a unique design feature, separates into two sections after it leaves the launcher. These sections have a strong unstable flight trajectory due to their shape. At approximately 1.27 m down range from the launcher's muzzle, the sabot segments can easily be separated from the rod by letting them impact the sabot-catcher, a thick steel plate with a 20 mm central hole which allows only the rod to continue its flight undisturbed.

Unfortunately, aerodynamically opening sabots are very vulnerable to disturbances in bow to stern air flow. Disturbances in the air flow are caused by energetic gases immediately behind the sabot package which can accelerate rapidly once the sabot package has left the launcher's muzzle. This energetic gas flow bursts past the sabot package to form a "reverse flow" region where the

atmosphere surrounding the sabot moves from the stern of the sabot to the bow. This "reverse flow" region destabilizes the rod/sabot package during its early flight, often causing unacceptable loss of package orientation.

In order to suppress "reverse flow", the launch-tube designated to these experiments has been adapted. Four slots have been drilled in the launch-tube wall near its muzzle to vent almost all of the gas-charge while the rod/sabot package is still supported. This procedure was proposed by Swift and Strange^[39-40]. The modifications to the launch-tube are shown in Figure 4.

3.4 The armour panel

The ceramic faced armour test panels were composed of 8.1 mm thick Morgan Matroc Hilox 973 alumina and aluminium 6061-T6. For the bonding layer, Scotchdamp BA-9323 from 3M was used. Based on the experimental observations discussed in refs. [32-34], the lateral dimensions of the armour panel was set at 155 mm. Because the alumina was available as tiles of 50 * 50 mm only, nine tiles had to be used to completely cover the panel. Four back-up plate configurations were used; a single 4.0 mm thick plate, a 6.0 mm thick plate, a package of two unbonded 3.0 mm thick plates, and an 8.0 mm thick back-up plate. The material properties of the alumina and the aluminium are presented in Annex A.

To ensure proper bonding of the ceramic tiles to the aluminium plate, the ceramic tiles were cleaned with methylchloroform (CH_3CCl_3). The aluminium plates were degreased (30 minutes in a bath of P₃RST (40 grams/l) at 75° C) and etched (20 minutes in a bath of chromic acid CrO_3 (55 grams/l) and sulphuric acid H_2SO_4 (275 grams/l) at 60° C). Afterwards the aluminium plates were rinsed with cold water and dried. The bonding material was applied to the aluminium plate, after which the individual tiles were placed by hand. Proper alignment was ensured by wrapping tape around the plates to prevent motion of the ceramic tiles before the bonding layer had hardened.

To ensure good bonding, a vacuumbag technique was used to apply the proper amount of pressure to all the tiles. For this purpose, the panels were placed on a thick aluminium plate which was protected by a teflon foil. On top of the armour plates another teflon foil was placed together with a woven glass fabric. The entire plate was then covered by a thin plastic foil. By means of a small vacuum pump, the enclosed volume was evacuated. For the entire 24 hours of hardening time of the bonding layer (at room temperature) the vacuum pump was left attached to the vacuumbag. The resulting bonding layer is thin (approximately 0.2 mm).

Armour panels like the one shown in Figure 5 are the result of this manufacturing process. The facilities of the Department of Aerospace Engineering at Delft University of Technology were used for the manufacturing.

3.5 The flash X-ray set-up

At the time this programme was carried out, a four channel 600 kV flash X-ray system (Field Emission corporation model 730/2660) and two 1.2 MV Scandiflash units (model 1200) were available at PML. The flash X-ray technique used, which is extensively described in ref. [34], does not limit the armour's lateral dimensions. It requires two flash X-ray pulsers to obtain all the information regarding projectile mass erosion, projectile position and armour deformation at a specific moment in time: the radiograph created by the obliquely positioned pulser provides information regarding projectile length and mass erosion, whereas the second pulser set up in plane with the armour panel's front surface provides information on the position of the projectile's rear-end, projectile debris formation and armour deformation. By using four pulsers, data can be obtained at two moments in time during one experiment.

The sharpness of the shadow depends on the spot size of the X-ray source and the position of the object between the source and the film. The shadows cast when the source is not a point, but a small area, are not perfectly sharp because each point of the source casts its own shadow of the object, and all of the shadows are slightly displaced relative to each other, thus producing an ill-defined image. All Field Emission pulsers have a 5 mm diameter anode, giving them a 5 mm spot source size. The Scandiflash pulsers had a 4 mm diameter anode installed, giving them a 4 mm diameter spot source size. With the experimental set-up presented in this report, the unsharpness is smaller than 0.5 mm. In the analysis of the radiographs, corrections are made for this unsharpness. The blurriness of the image also depends on the displacement of the object during the exposure time. In this study, where objects move with velocities of typically 1000 m/s, the X-ray pulser's exposure time of only 20 ns prevents motion-unsharpness becoming noticeable.

All FE (Field Emission) pulsers were operated at their maximum voltage, 600 kV. The Sc (Scandiflash) pulsers were operated at 1100 kV. All pulsers produce a wide beam of radiation at the moment of triggering. In order to prevent X-ray cassettes being exposed twice, diaphragms are placed such that beam widths are limited to those areas on the cassettes where the projectile/armour interaction image is recorded. The diaphragms used consist of thick (20 mm) steel plates. The X-ray pulser heads were protected from projectile and armour debris by 5 mm thick aluminium plates. The X-ray cassettes, with the Kodak Lanex Regular X-ray films and Ortho-G intensifying screens, were protected from armour and projectile debris by 2 mm thick plates of aluminium. Two cassettes were used in every experiment. One (300 x 900 mm) contained two films (300 x 400 mm each) to record the images of the three pulsers set up in the horizontal plane. The other cassette

(300 x 400 mm) contained a full-size negative to record the image from the pulser set-up in the vertical plane.

The positions of the pulser heads, diaphragms, cassettes, target and launch-tube are presented in Figure 6. Figure 7 presents a view of the experimental set-up inside and outside of PML's medium calibre test chamber. The obliquely positioned FE pulser was replaced by an SC pulser in experiments with armours with 8.0 mm thick back-up plates.

3.6 Triggering of the flash X-ray pulsers and velocity measurement

In order to be able to fire the flash X-ray pulsers at the desired moments in time during consecutive experiments (2, 4, 6, 8, 10, 12, 14, 16, 20, 25, 30, 35, 40 and 60 μ s), an accurate triggering mechanism was needed to pin-point the moment of impact.

A triggerfoil technique was used for this purpose. A triggerfoil consists of two thin layers of aluminium foil separated by a thin layer of paper. These three layers are taped to the ceramic facing of the armour plate and connected to a pulse generator. As the projectile impacts, the two aluminium foils connect, causing a short-circuit, and thus a trigger pulse. This trigger pulse is fed into three delay generators (two Hewlett Packard model 43114A digital delay generators and one Scandiflash DG-1000C delay generator) which set the delays for the flash X-ray pulsers. The discharge-pulses were monitored by a processing storage oscilloscope (Krenz Electronics PSO 5070) and were used to accurately determine the time between the moment of impact and the moment of pulser discharge. Two of the three FE pulsers had to flash at the first moment in time after impact (T_1) while the third FE pulser was to flash at the second moment in time, T_2 , together with the Sc pulser.

The projectile velocity measurement was carried out by measuring the interval of time needed by the rod to travel a distance of 1000 mm.

For this purpose two infrared lightscreens (Drello LS-19i) were set up in the path of the rod (see Figure 6). The signals from the lightscreens were fed into a Racal-Dana nanosecond counter (model 1991) and a processing storage oscilloscope (Krenz Electronics PSO 5070). A schematic flowchart of the triggering and measuring equipment is presented in Figure 8.

4 THE EXPERIMENTAL RESULTS

4.1 Introduction

The results of eight series of ballistic impact experiments are presented in this chapter. Armours with an 8.1 mm thick Morgan Matroc Hilox 973 alumina facing supported by four different aluminium 6061-T6 back-up plate configurations (4.0 mm, 6.0 mm, 2*3.0 mm and 8.0 mm thick) were impacted by steel rod projectiles just above and below their ballistic limit velocities.

Flash radiography was used to generate data on the projectile's position, length, armour penetration and armour deformation throughout the impact event.

The information captured in the radiographs was analysed using PML's digital image processing facilities. Corrections have been carried out in order to compensate for geometric distortion, penumbra, armour misalignment and obliquity. The procedure applied for these corrections is presented in ref [34].

More than 130 experiments using the X-ray equipment were necessary to obtain the data showing the projectile/armour interaction process at 2, 4, 6, 8, 10, 12, 14, 16, 20, 25, 30, 35, 40 and 60 μ s after impact for each of the eight series of experiments.

The experiments showed that on many occasions the rods impacted the armours with a small amount of yaw. Rod impact with a yaw angle smaller than four degrees, however, was considered acceptable.

The experimental data presented in this chapter are further analysed, discussed and compared to ALARM simulations in Chapters 5 and 6.

4.2 Armours of 8.1 mm alumina and 6.0 mm aluminium

4.2.1 Impact below the ballistic limit velocity

The complete sequence of radiographs was compiled from eight experiments and is presented in Figure 9. The average projectile impact velocity was 815 m/s (± 26 m/s). In all of these experiments the projectile was stopped by the armour. Figure 10 presents the projectile rear-end position, armour penetration and armour deformation in time as deduced from these radiographs. The resulting projectile length reduction in time is presented in Figure 11. Polynomials are best-fitted through the data-points. The data and constants in these polynomials are presented in Annex B.

During the first 16 μ s, no significant armour penetration and armour deformation could be measured. Projectile fragments are seen moving away laterally from the impact area from the

moment of impact onwards. Projectile length reduction occurs until 45 to 50 μ s after impact. A typical recovered projectile, as presented in Figure 12, weighs on average 2.6 grams and is approximately 12 mm long. Hence, approximately 60% of its mass has been eroded.

With all experiments the ceramic facing has completely delaminated from the back-up plate after impact. Figure 13 shows an example of a recovered ceramic facing viewed from front and rear. A typical example of a recovered back-up plate is shown in Figure 14. Some fractured ceramic material is still attached to the plate. In this example it has approximately the original ceramic thickness, indicating that the projectile was unable to penetrate the ceramic material directly underneath it. The area of back-up plate covered with ceramic material has a 20 mm radius around the impact point. This suggests that this section of the back-up plate was initially loaded by the projectile through the ceramic conoid. The area corresponds to the base area of a 65° ceramic fracture conoid. Figure 14 also shows the back-up plate deformation. The maximum deformation is 5 mm. No cracks or shear-zones were detected in the back-up plate.

4.2.2 Impact above the ballistic limit velocity

The armour is no longer capable of defeating the projectile, when the impact velocity is increased by 101 m/s to 916 m/s (± 18 m/s). The results of seven experiments were used to obtain the sequence of radiographs presented in Figure 15. The projectile's rear-end position, armour penetration and armour deformation versus time are presented in Figure 16. The projectile length reduction in time is presented in Figure 17. Again, polynomials are fitted through the measured data. The constants are presented in Annex B.

During the first 14 μ s of the impact process, no armour penetration or armour deformation was measured. After this period they both increase rapidly. The back-up plate deformation is limited to a relatively small area of the back-up plate. At 60 μ s, the maximum back-up plate deformation is 11 mm. Back-up plate failure is noticeable in the normal radiograph at that time. Figure 18 shows a typical recovered back-up plate. A section with an approximate diameter of 10 mm has been sheared out. Figure 19 presents an example of a recovered projectile. It has an average weight of 2.3 grams and is approximately 10 mm long; hence, 70% of its mass is eroded.

In most experiments in this series, the projectile pushes all ceramic material ahead of it without penetrating the material on the impact axis. After some experiments a (comminuted) ceramic plug was recovered together with the eroded projectile. Radiographs taken after back-up plate perforation show these plugs flying in front of the eroded projectile. In some, the projectile appears to have been capable of penetrating a limited amount of thickness of ceramic facing. This has caused some scatter in the armour penetration data.

4.3 Armours of 8.1 mm alumina and a package of two 3.0 mm thick layers of aluminium

4.3.1 Impact below the ballistic limit velocity

Steel rod projectiles impacting the double back-up plate armours at a velocity as high as 819 m/s (± 13 m/s) are unable to perforate it. Hence, contrary to the expectations, this armour is not significantly easier to penetrate when compared with the armour with the single 6.0 mm thick back-up plate.

The sequence of radiographs, presented in Figure 20, was compiled from seven impact experiments. Figure 21 presents the projectile rear-end position, armour penetration and armour deformation in time as deduced from the radiographs. Polynomials are fitted through the data-points. Again, the data and polynomial constants are presented in Annex B. The data show that the projectile was unable to penetrate the ceramic facing as the distance between the location of the projectile tip and back-up plate remains constant. The projectile length reduction in time is presented in Figure 22. It continues longer than 60 μ s. The average recovered projectile weighs 2.4 grams and is approximately 11 mm long (Figure 23). A typical recovered back-up plate is shown in Figure 24. A clearly visible, comminuted ceramic plug is seen still bonded to the back-up plate. The smooth ceramic front facing visible on top of this plug confirms the above observations. The maximum deformation of the back-up plate was 11 mm for the top layer and 11 mm for the second layer.

4.3.2 Impact above the ballistic limit velocity

By increasing the impact velocity by 119 m/s, this armour is defeated by the steel rod. Eight impact experiments where rods impacted the armour with an average velocity of 938 m/s (± 23 m/s) were used to obtain the complete sequence of radiographs. This sequence is presented in Figure 25. At 60 μ s, failure of the back-up plates become visible. At 120 μ s, the projectile is observed to have perforated the target completely. The projectile rear-end position, armour penetration and armour deformation in time are presented in Figure 26. The projectile length reduction in time is shown in Figure 27. The constants in the polynomials drawn in these figures are presented in Annex B. The radiographs show some scatter in the projectile's behaviour. The image at 30 μ s shows a much larger projectile than the earlier and later radiographs. The reason for this scatter is not clear. Figure 28 shows a recovered projectile, on average weighing 2.3 grams and 10 mm long. The radiographs show that the back-up plate deformation has a more local nature than when impacted with the lower velocity. The perforated two-layer back-up plate is shown in Figure 29. A 10 mm hole has been created by the rod. Some star cracks can be seen radiating

outward from the impact area. The two layers have failed by a combination of shear and star-cracking.

4.4 Armours of 8.1 mm alumina and 4.0 mm aluminium

4.4.1 Impact below the ballistic limit velocity

The sequence of radiographs presented in Figure 30 were taken from the results of nine ballistic experiments. The average projectile impact velocity was 786 m/s (± 26 m/s). All projectiles were defeated by the armour. The projectile rear-end position, armour penetration and armour deflection are presented in Figure 31. The projectile length reduction in time is presented in Figure 32. Polynomials are fitted through the measured data. The projectile does not appear to penetrate the ceramic material directly underneath it. Projectile length reduction continues for more than 55 μ s. A recovered projectile is shown in Figure 33. It weighs on average 2.4 grams and is approximately 11 mm long. A recovered back-up plate is shown in Figure 34. The maximum deformation is 11 mm. In some back-up plates star-cracks are visible, indicating that the armour had just failed, even though the projectile was unable to penetrate.

Several impact experiments at very low impact velocities (<600 m/s) show interesting details of the conoid cracks in the oblique radiograph at later times after impact (>25 μ s). A representative set of radiographs, taken at 25 μ s after impact, is presented in Figure 35. After a straightforward analysis of this radiographic image, the (half) angle of this displaced ceramic conoid was calculated to be 57°.

4.4.2 Impact above the ballistic limit velocity

A 43 m/s increase of the projectile velocity (to 829 m/s ± 17 m/s) results in armour perforation. The complete sequence of radiographs is presented in Figure 36. The data deduced are presented in Figure 37. They show that the projectile is not able to penetrate the ceramic material directly underneath it. The projectile length reduction in time is given in Figure 38. A recovered back-up plate is shown in Figure 39. This plate has failed by a combination of shear and star-cracking. A back-up plate area with a 35 mm diameter seems to be initially loaded by the projectile. A recovered projectile is shown in Figure 40. It weighs 2.4 grams and is 11 mm long. According to Figure 38, this erosion is the result of some 55 μ s of length reduction.

4.5 Armours of 8.1 mm alumina and 8.0 mm aluminium

4.5.1 Impact below the ballistic limit velocity

The sequence of radiographs presented in Figure 41 show a steel rod impacting the described armour with an average velocity of 995 m/s (± 16 m/s). At this velocity the projectile is not able to perforate the armour. The results are presented in Figure 42. The position of the projectile-tip cannot be determined at times greater than 40 μ s, since from that moment onwards the projectile's rear-end position is no longer visible in the radiographs.

Projectile length reduction in time is presented in Figure 43. The reduction continues less than 50 μ s. A recovered projectile weighs, on average, 1.8 grams and is approximately 8 mm long (Figure 44). A typical example of a recovered back-up plate is presented in Figure 45. A section of the back-up plate has been sheared off. Signs of local tensile stress failure are also observed at the back-up plate's rear face. Over an area with a 20 mm radius, fragments of the bonding layer are visible. This suggests that the impact load was initially spread over this area. The results presented in Figure 42 show that the projectile was unable to penetrate through the ceramic material directly underneath the point of impact.

4.5.2 Impact above the ballistic limit velocity

With an increase of 96 m/s of the impact velocity, the projectile is able to perforate the armour. The sequence of radiographs presented in Figure 46 show the projectile/armour interaction process for the steel rod impacting the armour with an average velocity of 1091 m/s (± 14 m/s). The data deduced from the radiographs are also presented in the Figures 47 and 48. After 35 μ s, the position of the projectile can no longer be determined. At 40 μ s, back-up plate failure is clearly visible. The back-up plate deformation has a very local nature. Figure 49 shows an example of a recovered back-up plate. It shows some evidence of spallation and a 10 mm diameter plug is sheared out of it. The initial stages of failure resemble those observed in the previous section. The spalled back-up plates show only a minimum amount of overall back-up plate deformation. The projectile's length as observed in the oblique radiographs shows some scatter between images. This scatter is probably due to the spallation mechanism. Projectile length reduction continues for some 40 μ s. A recovered projectile weighs some 2.6 grams and is approximately 12 mm long (Figure 50).

5 ANALYSIS OF THE EXPERIMENT RESULTS

5.1 Introduction

The radiograph sequences, the recovered back-up plates and ceramic facings were used to analyse the projectile/armour interaction process. The most probable mechanism used by the ceramic facing to distribute the impact load over the back-up plate is discussed. The differences between deformation profiles of the various back-up plate concepts are discussed and linked to the load distribution process by the ceramic facing. The influence of the various back-up plate properties on the armour's performance is assessed by analysis of the back-up plate deformations and failure modes. The deformation and erosion of the rods during impact is discussed.

The use of the blunt steel rod as a simulator for the 7.62 mm AP projectile is assessed, and forms the last topic in this chapter.

5.2 The behaviour of the ceramic facing during impact

On the basis of the experimental observations, the ceramic facings recovered, the fragments found attached to the back-up plate and the literature, the following description of events is presented for the response of the ceramic facing during the shock-wave period of time and the following structural response period of time.

On impact, the stress fields in the ceramic are initially elastic, and the largest tensile stresses are in the radial direction (the Boussinesq stress field)^[44-45]. The tensile strength of ceramics is very low when compared to their compressive strength. Therefore, the cracks that form (normal to the direction of maximum principal stress) are ring cracks concentric around the impact site, near the rod's periphery. According to Shockey et al.^[46] and Frechette & Cline^[47], these cracks are shallow, extending only a millimetre or so beneath the ceramic's surface. The ring cracks continue to grow, following paths normal to the direction of principal tensile stress, assuming angled trajectories from the initial normal-to-the-surface direction. Thus, several large Hertzian conoid cracks extend into the ceramic material. Frechette & Cline observed that as the impact velocity approaches the armour's ballistic limit velocity, other conoids of larger cone angle formed around the primary conoid. The conoid fractures, visible in some of the recovered ceramic facings, belong to this group of conoids.

Star cracks, caused by high tensile hoop stresses, also run into the ceramic material. Slight discontinuities in the recovered conoid fragments at their intersections with members of the star cracks indicate that these star cracks occur earlier in time. According to Frechette & Cline, these star cracks emanate from the conoid surface, the intersection of the conoid with the back-up plate and from within the conoid enclosed volume. They assume that these cracks then spread faster than the conoid cracks, in order to account for the fracture discontinuities described above. However, it is very unlikely that the star crack velocity is higher than the Hertzian conoid crack velocity as both are caused by principal tensile stresses in the ceramic. It is more likely that the star cracks originate at the ceramic back-up plate interface, soon after the first reflection of the impact stress wave. They then spread radially and towards the impact surface. They meet the conoid cracks as these have just extended into the ceramic over a limited depth, causing the described discontinuities in the lower section of the conoid when the conoidal cracks extend. Mescall & Tracy^[20] support this reasoning with their HEMP computations, showing tensile hoop stress failure shortly after reflection of the stress wave at the ceramic back-up plate interface. Wilkins^[16] also shows failure proceeding from the ceramic back-up plate interface towards the impact face in his HEMP computations. Although he excluded failure by hoop-stresses from his computation, the failure is caused by the loss of support by the back-up plate and therefore very similar to the failure described above.

The recovered sections of the fracture conoids that survived impact, Figures 14 and 24, show that the projectile was unable to penetrate through the ceramic material directly underneath it. These fracture conoids include a cylindrical section of ceramic material which appears partly pulverized but recompacted. Its diameter is comparable to that of the projectile. This pulverization of the ceramic may be explained in the following manner. Rosenberg et al.^[43] showed that shocking ceramics above the HEL (Hugoniot Elastic Limit) will introduce an extensive amount of micro-fracture to the material. Together with Bless, he also showed that the HEL is exceeded in AD85 alumina when a steel projectile impacts at a velocity above 370 m/s^[42]. Hence, in the impact velocity range used for the experiments reported here, 700 m/s - 1100 m/s, a peak shock-stress is introduced into the alumina target which exceeds the HEL to a significant degree. Taking into account that the diameter of the blunt projectile (D) is comparable to the thickness of the ceramic facing (T), and assuming that the peak transient stress falls to D/T of its peak value at the ceramic rear-surface, a substantial amount of ceramic underneath the blunt projectile is expected to experience a peak shock stress above HEL, explaining the partial comminution of the ceramic material.

When the shock-waves no longer dominate the response of the ceramic, the structural response follows. The recovered pie-shaped segments of the fracture conoids show details of overlying conoid-like fractures (Figures 14a and 24a). The fracture pattern shows that these conoid-like cracks occur later than the star cracks. Their slope, similar to the Hertzian conoid cracks, indicate that these cracks do not originate from the ceramic's impact face. Some of the recovered fragments show initial fracture to be oriented perpendicular to the ceramic's back face, suggesting a tensile radial stress as the instigator. According to Wilkins' HEMP computations^[16], these fractures could have been generated early in the impact process. However, photographs of the development of axial cracks and conoids in alumina targets backed by thick steel plates and impacted by conical projectiles, show no signs of these rear-surface initiated cracks^[15, 46, 47].

It is likely that these conoid-like fractures start occurring some time after the primary Hertzian fracture conoid intersects with the back-up plate. The high impact load accelerates the conoid and the underlying back-up plate. The back-up plate deforms correspondingly, introducing high tensile radial stresses near the edges of the fracture conoid's base. The relatively low tensile strength of the ceramic results in conoid-like cracks growing opposite to the direction of impact towards the axis of impact. During this process, which is illustrated in Figure 51, relatively thin "conoid-shell elements" are formed, which due to their constraint to follow the back-up plate's deformation, introduce a high shear load on the periphery of the central ceramic volume underneath the impact area. When lateral confinement of the "conoid-shell element" is sufficient, shear failure around this periphery occurs. As a result, the impact load is now spread over a smaller area of back-up plate. The process repeats itself, depending on the loading and back-up plate response. It may end when the ceramic plug has completed its formation. This plug then loads the back-up plate over an area nearly equal to that of the projectile. As a result, this plug may shear through the back-up plate or be defeated by it. Ceramic plugs have indeed been observed flying in front of the projectile on radiographs taken late after penetration.

The proposed behaviour suggests that aside from a group of static properties (hardness, sound velocity, Young's modulus, Poisson's ratio, density and porosity^[48]), a high tensile strength and a high shear strength are also important for ceramic materials, in order to be able to distribute the impact load effectively. Rosenberg et al.^[43] confirm that ceramic materials exhibiting a lower (after shock) shear strength are easier to penetrate with blunt projectiles.

5.3 The behaviour of the back-up plates during impact

The observed back-up plate responses to rods impacting with velocities below the V_{50} s are for the various concepts, to some extent, similar to each other. These responses are shown together in Figure 52. The response velocities, deduced from the polynomials, are presented in Figure 53. Due to the moderate accuracy of the radiograph analysis procedure (± 0.5 mm), an accurate analysis of the armour responses during the first 16 μ s of the impact process cannot be given. After this period the responses of the armours with the 4.0 mm, 6.0 mm and 2*3.0 mm thick back-up plates are similar to each other, as the projectiles have impacted these armours with almost identical velocities (786 m/s, 815 m/s and 819 m/s, respectively). One can see then that the armour with the 2*3.0 mm thick back-up plate, which has the lowest bending stiffness of the three, shows the fastest response up to 40 μ s after impact. The single 6.0 mm thick back-up plate, which only differs from the 2*3.0 mm thick back-up plate in its 4 times higher bending stiffness, responds slower to the impact event. The 4.0 mm thick back-up plate's response lies between the two during the first 40 μ s of the impact process. Its slightly higher bending stiffness than the 2*3.0 mm combination, apparently compensates its 33 per cent lower mass, tensile and shear strength.

At 26 μ s after impact, the 6.0 mm thick back-up plate starts its deceleration, followed by the 2*3.0 mm combination at 32 μ s. The 4.0 mm thick back-up plate starts its deceleration later than 40 μ s after impact, due to its relatively poor tensile load carrying capabilities. The response of this back-up plate therefore exceeds the response of the 2*3.0 mm thick back-up plate, late after impact (>60 μ s). The response of the 8.0 mm thick back-up plate lies between the others. This response is caused by an impact at 995 m/s, almost 200 m/s (24 per cent) higher than for the other armours, preventing a direct comparison with the responses of the other back-up plates.

The comparisons show that a high bending stiffness results in better support of the ceramic fracture conoid, as it reduces the deformation transient and the accumulation of strains. At later times after impact (>30 μ s) the back-up plate's ability to dissipate the kinetic energy of the eroded projectile, the ceramic fracture conoid and the back-up plate itself becomes important. For metallic back-up plates a quick dissipation of energy is essential in order to prevent the strains from accumulating to a catastrophic level.

When the impact velocity is increased, all the armours are defeated by the rods. Their back-up plate responses are presented in Figure 54. The response of the armour with the 4.0 mm thick back-up plate when impacted at a velocity of 829 m/s illustrates the necessity for a back-up plate to dissipate the energy quickly. Its failure can be completely attributed to the high strain accumulation during

the back-up plate acceleration accompanied by its poor tensile load carrying capabilities, which result in a too slow deceleration and energy dissipation. The other three armour responses are very similar. Analysis showed that the impact load can account for this high back-up plate acceleration when only a very small area of back-up plate is involved. Hence, the shear load carrying capabilities of the back-up plate must have been exceeded by the impact loading. Very local deformation is witnessed in the radiograph sequences. Shear failure zones are also visible in recovered back-up plates. The experimental results indicate that shortly after impact ($\pm 16 \mu s$) the ceramic facing appears to have lost its ability to distribute the high impact load over a large section of the back-up plate. Although it appears as if the ceramic facing experiences a dramatic change of behaviour when impacted at these higher velocities, its behaviour can be completely explained by the phenomenological description of events presented in Section 5.3. The increased impact velocity results in a higher impact load, which is accordingly distributed through the ceramic conoid over a section of the supporting back-up plate. However, the increase of loading is such that at a certain back-up plate radius, local shear deformation of the back-up plate results in high tensile and shear stresses near the edges of the ceramic fracture conoid base. These stresses cause failure of the ceramic conoid, as described in Section 5.2, and reduce the area over which the impact load is spread. As a result, the high impact load is now distributed over an even smaller area, immediately causing more shear deformation and more conoid base area reduction. This process may continue until only a small section of the ceramic conoid remains, distributing the load over an area of back-up plate comparable to that of the projectile. The unstable nature of this process results in a fast concentration of the impact load on a very small area of back-up plate, as was observed experimentally.

The results of the experiments indicate that there are a number of back-up plate properties, being tensile strength, shear strength, strain to failure and bending stiffness, that can strongly influence a ceramic faced armour's performance. Increasing the back-up plate's tensile strength, shear strength and strain to failure (for strain rates of 10^4) will improve the armour's ballistic performance.

Good tensile load carrying capabilities of the back-up plate reduce the growth of tensile strains, as they aid the back-up plate's resistance to deformation, especially when the deformation grows larger. The majority of impact experiments above the ballistic limit have shown that a too high shear load on the back-up plate, early in the impact process causes catastrophic back-up plate failure. Hence, the shear load carrying capabilities of the back-up plate are very important as well. A high strain to failure allows the back-up plate to absorb more energy before failing. A high bending stiffness reduces the deformation transient as the back-up plate is more reluctant to deform. It aids the confinement of the ceramic fracture conoid to its original volume. The lateral extend of the

deformation field increases with bending stiffness. Thus, a high bending stiffness effectively reduces the tensile strains in the back-up plate.

However, the bending stiffness has to be considered as a subtle parameter. Both an increased and decreased stiffness may, depending on the armour configuration, improve performance.

When the armour's back-up plate fails by tensile strains exceeding the material's ultimate strain, the armour's ballistic protection level can be enhanced. An increase of the bending stiffness of this back-up plate will improve the armour's ballistic performance as it hinders the back-up plate deformation and thus accumulation of strain.

On the other hand, when one considers an armour with a back-up plate that fails by plug-shearing, an increase of its bending stiffness will not enhance the performance. The shear strength of the back-up plate is the weak link. Increase of the back-up plate's bending stiffness will further reduce the response of the surrounding back-up plate, shortening the time necessary to complete plug separation. However, by decreasing the back-up plate's bending stiffness such that the shear strength remains the back-up plate's weak link, the armour's performance can possibly be enhanced. The decrease of bending stiffness, facilitates the response of the back-up plate material surrounding the plug, thereby lengthening the time necessary to complete plug separation. As a result, the projectile-plug is decelerated for a much longer period of time and the back-up plate dissipates a larger amount of kinetic energy.

The experimental results show that for armours with 6.0 mm thick and 2*3.0 mm thick back-up plates, the ballistic limit velocities lie close together. The change in ballistic performance, resulting from a change of bending stiffness as described above, is not witnessed in these experiments due to the fact that the failure mode changes also.

5.4 The behaviour of the projectile during impact

All the series of radiographs presented in the previous chapter show a similar projectile behaviour. From the moment of impact onwards, projectile material is seen being ejected in a radial direction from the impact area. Projectile plastic deformation appears to remain confined to a small area near the projectile-ceramic interface. The high circumferential stresses and the grain texture of the projectile material - long stretched grains in the axial (impact) direction - cause radial fracture of the ejected material. The high radial velocity gradient in the resulting strips of ejected material cause them to stretch and fail at some point in flight. The fringes of free-flying projectile material created by this process are visible in almost all the later time radiographs. With the exception of fracture, the projectile's deformation process resembles that of a water-jet impacting a rigid wall.

The radiographs and recovered projectiles indicate that the radial ejection process continues in a similar fashion after the formation of the fringes. Plastic deformation of the projectile remains

limited to a small area adjacent to the projectile-ceramic interface. The radial fracturing process of the ejected projectile material also continues. As time progresses, the strips of ejected material may either fracture, break loose or curl backwards due to their interaction with the armour. A schematic description of the projectile behaviour is given in Figure 55.

Information on the projectile length reduction in time was also obtained from the radiographs. All projectile length reduction polynomials are merged in Figure 56. As can be seen, the differences in projectile length are very small at later times ($> 50 \mu\text{s}$) after impact for all situations and velocities considered. The recovered projectiles vary in length between 8 mm and 12 mm. Their shanks show very little plastic deformation (mushrooming). Some still have a few curls of ejected material attached to them. On average, these recovered projectiles account for about 34 per cent of the projectile's original mass (7 grams). The length reduction rates are presented in Figure 57. It shows that the length reduction process continues for a period of at least 40 to 60 μs . The longer length reduction periods are associated with impact on armours with more flexible supports (e.g. the 2*3.0 mm thick and 4.0 mm thick back-up plates).

The series of experiments show that the blunt steel rods appear to erode mass for a considerable amount of time. The rods do not break up into a discrete number of fragments during impact. The recovered shanks show little plastic deformation. The fringes of eroded projectile material, visible on the radiographs, fly away from the impact area with maximum velocities of 560-960 m/s.

5.5 The blunt steel rod as a simulator of the 7.62 mm AP projectile

Wilkins^[15] carried out experiments with blunt and sharp projectiles. He observed that the projectile nose-shape is responsible for differences of up to 40% of the ballistic limit velocity for targets with AD85 alumina facings. Hornemann et al.^[41] showed that the stress wave generated in the target depends strongly on the nose-shape of the projectile. In this section the projectile/armour interaction process as observed for the blunt 6.0 mm diameter rod is compared with the results obtained for the ogive-nosed 7.62 mm AP projectile in ref. [34]. This allows us to assess the applicability of the results obtained with the blunt steel rods as representative for the penetration of the ogive-nosed 7.62 mm AP projectile.

The position-versus-time curves for 7.62 mm AP and 6 mm rod impact into armours of 8.1 mm alumina supported by 6.0 mm aluminium are compared in Figure 58. This comparison shows that the experimental results match extremely well. The armour responds almost identically to both projectiles. Neither projectile nor rod was able to penetrate the ceramic material directly underneath the point of impact. Slight differences are observed between the position of the rear-end of the

projectile and the rod at later times after impact ($>25 \mu\text{s}$). This can be expected as the lead plug in the rear-section of the 7.62 mm AP projectile decelerates slower than the rod as it bulges around the central hard steel core of the 7.62 mm AP. The comparison therefore shows that the projectile/armour interaction process obtained from experiments with blunt steel rods can be taken as representative for 7.62 mm AP projectile impact into these armours.

The similarity of the behaviour of the AP and rod projectiles may, however, be limited to the velocity regime of these experiments. The strength and shape of the shock wave introduced into the armour by the blunt rod are different from the shock wave introduced into the target by the 7.62 mm AP projectile. Bless et al. [42] have shown that at impact velocities of 800 m/s, blunt rods (of diameter comparable to the thickness of the ceramic facing) cause much more material to experience a peak shock-stress well above the Hugoniot elastic limit (HEL) when compared with ogive-nosed projectiles. According to Rosenberg et al. [43], this (above HEL) shock wave may cause "catastrophic" loss of shear strength and a corresponding poor ballistic performance with some materials. By increasing the impact velocity, the peak shock-stress in the ceramic increases. This may cause such an increase of "catastrophic" loss of shear strength in the ceramic for the blunt rod projectile impact, that the similarity between the projectile/armour interaction processes for the 7.62 mm AP and rod projectile is lost.

6 ANALYTIC MODEL SIMULATIONS

6.1 Introduction

To run the ALARM model, a number of input parameters have to be quantified. These parameters govern the geometry, composition and material properties of the rod and armour. In addition, the penetration resistance properties of the comminuted ceramic, as defined in ref. [30], have to be specified. The obtained set of input parameters is used to compute ballistic limit velocities with the model and compare them with the experimental results.

An important feature of the developed model is that it can present the user with detailed information on the impact process. In order to verify the behaviour predicted by the penetration model, the steel rod impact experiments presented in Chapter 4 were simulated, and compared with the experimental data.

6.2 The ALARM model input parameters

A number of parameters governing the armour and projectile material properties and impact conditions have to be quantified in order to use the model. Most of them can be obtained easily, as they describe the armour and projectile geometry and composition. A number of input parameters describing material properties, such as densities, ceramic bulk modulus, ceramic longitudinal wave velocity and all of the back-up plate material properties are obtained from available data sheets (Al6061-T6 is not strain-rate sensitive).

The fracture conoid angle has to be specified as well. The (half) conoid angle is set at 65° . At this angle, the size of its base area matches the experimental observations in Section 4.2. The radius of the back-up plate allowed to respond to the impact event is set at $5/3$ of the base radius of the ceramic fracture conoid. The radiographs and recovered back-up plates show that most of the plastic deformation is limited to within this area.

In the ALARM model, the projectile's elastic wave velocity is used to set the initial armour penetration velocity at the moment that the ceramic fracture conoid has completely formed, typically some $5 \mu\text{s}$ after impact. For this purpose, the ALARM model uses an equation which is, strictly speaking, valid at the moment of impact only. In order to obtain initial penetration velocities close to the ones observed experimentally at $5 \mu\text{s}$ after impact, the elastic wave velocity is used as a tune-parameter and set at 500 m/s , which is approximately ten per cent of its original value.

Neither the dynamic yield strength nor the plastic wave velocity are given in the available ETG-100 data sheet. Hence, they had to be obtained from the experimental results. During the first $40 \mu\text{s}$ of the impact process, the experimentally observed projectile behaviour, presented in Section 5.4, complies reasonably well with the projectile behaviour modelled in the so-called mass erosion phase [30] of the impact process. The projectile material's dynamic yield strength was determined from the experimentally obtained projectile rear-end position and length reduction polynomials using equation [33] of ref. [30]. The dynamic yield strength was found to be $0.17 \cdot 10^{10} \text{ N/m}^2$, very close to the value of $0.19 \cdot 10^{10} \text{ N/m}^2$ given by Rosenberg & Tsaliah,[49] for a similar but slightly stronger steel.

At the moment that the projectile length reduction velocity equals the plastic wave velocity, the end of the projectile mass erosion phase is initiated in the ALARM model. Therefore, the plastic wave velocity was set to 133 m/s , equal to the average length reduction velocity measured from the polynomials at $40 \mu\text{s}$ after impact.

The input parameters that still have to be determined are the comminuted ceramic's penetration resistance properties, represented by the constants β and γ in equation [43] of ref. [30], and

(optional) the radius of the hole r_{hole} surrounding the impact point through which the ejection of comminuted ceramic may take place (equation [61] of ref. [30]).

These parameters have not been linked to known material properties. They have to be obtained using a tuning-procedure. The parameters were chosen such that the ballistic limit velocities of the armours with the thin back-up plate (4.0 mm) and thick back-up plate (8.0 mm) match the experimental results. The comminuted ceramic ejection option was not used. The complete set of input parameters used for the ALARM simulations is presented in Annex C.

6.3 ALARM simulation versus experiment

The ballistic limit velocities of armours composed of 8.1 mm thick Morgan Matroc Hilox 973 alumina supported by a whole variety of thicknesses of aluminium 6061-T6 were computed by the model. The results are presented in Table 1, and compared with the experimental results in Figure 59. The ALARM model correctly predicts that the ballistic limit velocity of the armour with the double back-up plate lies close to the V_{50} of the armour with the 6.0 mm thick back-up plate. Based on the limited amount of experimental ballistic limit velocity data, the agreement between experiment and simulation appears to be good. The ALARM model computations show that the armour with the 4.0 mm thick back-up plate fails due to the accumulation of high tensile strains, when impacted just above the ballistic limit velocity. The armour with the double back-up plate (2*3.0 mm) fails in a combined shear-tensile mode when impacted just above the ballistic limit velocity. The first back-up plate is sheared off, the second layer fails in tension. The armours with the 6.0 mm and 8.0 mm thick back-up plates both fail by plug-shearing. These failure modes match the experimentally observed failure modes.

In order to compare details of the penetration processes as predicted by the ALARM model with the experimental observations, simulations were carried out for all four armour configurations with the same impact velocities that were used in the experiments. The results of these simulations are presented in Table 2 which shows that the ALARM model correctly predicts armour or projectile defeat in all situations. Comparisons between experimentally determined and predicted projectile rear-end position, armour penetration and back-up plate deformation profiles are presented in Figure 60 for the impacts with velocities below the ballistic limit.

For all four impact events, the computed back-up plates responses are somewhat slow when compared with the experimental data. This is very evident at early times after impact, as is illustrated in Figure 61. The ALARM model correctly predicts that the differences in back-up plate response become more significant at later times after impact. The computed positions of the rear-end of the projectile match the experimental observations very well. The armour penetration by the

projectile is somewhat overpredicted by the model, especially when the (slow) back-up plate response is taken into account.

A comparison between the projectile length reduction transients as experimentally determined and computed by the model is presented in Figure 62. With the exception of the projectile impacting the armour with the 8.0 mm thick back-up plate, projectile length reduction is slightly underestimated. The too high armour penetration by the projectile early in the impact process, as the model computed, is accountable for this result.

The comparison of the simulations with the experimental results show that for impact below the armour's ballistic limit velocity, the ALARM model is capable of predicting details of the impact process with acceptable accuracy.

ALARM simulations were also carried out for projectiles impacting with velocities above the armour's ballistic limit. The comparisons between the simulations and the experimental results are presented in Figure 63. Also here, the computed projectile rear-end positions match the experimental data very well. The maximum back-up plate deformation, however, clearly lags behind when compared with the experimental results for all but the armour with the 4.0 mm thick back-up plate. At the specified velocities, the ALARM model predicts that the shear failure mode dominates in all four back-up plates. This failure mode was also observed experimentally for the armours with the 6.0 mm and 8.0 mm thick back-up plates. According to the experimental data presented in Sections 4.3 and 4.4, the armours with the 4.0 mm and 2*3.0 mm thick back-up plates fail by accumulation of high tensile strains in combination with some plug shearing. The ALARM model predicts the correct back-up plate failure modes when the armours are impacted with velocities just above the computed ballistic limit velocity. However, at the higher velocities used in the experiments, the model predicts the shear failure mode to be dominant. This results in large differences between simulated and measured response, as observed in Figure 64, especially for the armour with the 4.0 mm thick back-up plate.

This figure also shows that a time-delay of approximately 25 μ s exists between the measured and computed responses of the armours with the 2*3.0 mm, 6.0 mm and 8.0 mm thick back-up plates. The projectile length reduction and armour penetration profiles presented in Figures 65 and 66 match the experimental results fairly well. The armour penetration profile calculated for the impact onto the armour with the 4.0 mm thick back-up plate is somewhat overestimated. The armour penetration calculated for the impact into the armour with the 8.0 mm thick back-up plate is somewhat underestimated. Due to these deviations from the experimental results, the projectile length reductions calculated for impact into these two armours differ somewhat from the experimental data.

The comparison of the simulations with the experimental results show that for impact above the armour's ballistic limit velocity, the ALARM model is capable of predicting details of the impact process correctly, with the exception of the back-up plate response. The back-up plate response is found to clearly lag behind, especially in those situations where the experimental results indicate that the armour's back-up plate has failed by plug-shearing.

6.4 Discussion

The results of the ALARM simulations show that the calculated behaviour complies with the experimental observations. The computed ballistic limit velocities for the armours with the 6.0 mm and 2*3.0 mm thick back-up plates match the experimental data very well.

The back-up plate responses computed by the model for impacts below the ballistic limit velocity are somewhat slow when compared with the experimental observations. This is easily explained. The ALARM model assumes that the section of back-up plate, loaded by the projectile through the ceramic fracture conoid is rigid, and cannot deform. This implies that the ceramic fracture conoid loaded by the projectile and all of the back-up plate material directly underneath it, are constrained to experience the same acceleration. However, the series of radiograph sequences show the back-up plate bulging from the moment that deformation becomes noticeable. Only a small central area of back-up plate seems to experience the maximum acceleration. Hence, a comparatively large section of back-up plate encounters the maximum acceleration in the model. With similar impact loading conditions, this inevitably results in a slower acceleration of the back-up plate by the ALARM model when compared with the experimental results. By introducing a modification to the back-up plate deformation field used in the ALARM model, such that it better simulates a bulging back-up plate, the model can be expected to produce a better match with the experimental back-up plate deformation.

The discrepancies observed between the calculated and experimentally obtained armour penetration profiles are related to the projectile/armour interaction mechanism used in the model. In the series of experimental results presented in this report, the projectiles appear (almost) unable to penetrate the ceramic material directly underneath it. As presented in Section 5.2, the impact load is distributed through the ceramic conoid over a limited area of back-up plate shortly after impact. As the back-up plate deflects, the edges of the base of this ceramic conoid are no longer able to distribute the impact load. This results in the impact load being distributed over an increasingly smaller area of back-up plate, without the projectile having to penetrate through the ceramic material.

The ALARM model assumes that the projectile is able to penetrate through the ceramic material inside the fracture conoid. The ceramic material underneath the projectile is assumed to distribute

the impact load over an area of back-up plate. The size of this area decreases as the projectile penetrates through the ceramic material and closes in on the back-up plate. Hence, by over-estimating the projectile penetration, the model distributes the impact load over the back-up plate in a similar fashion as is observed experimentally.

The differences between the calculated and the measured back-up plate deformation profiles, for impacts above the armour's ballistic limit velocity, are also related to the aforementioned projectile/armour interaction mechanism. The quick response of the back-up plates, observed in the experiments, is caused by a too high shear load on the back-up plate, which results in a quick localization of the impact load on a small area of back-up plate, as described in Section 5.2. This immediately initiates the plug-shearing mechanism. In the ALARM model, the projectile has to penetrate through almost the complete thickness of ceramic facing before it can effectively distribute the load over a similar small area of back-up plate. On average it takes the rod 25 μ s to accomplish this ceramic penetration, matching the time-delay observed in the comparisons of the results presented in Figures 65, 66 and 68.

The change of failure mode, calculated by the ALARM model for the armours with the 4.0 mm and 2*3.0 mm thick back-up plates, when the impact velocity of the rods is increased to those used with the experiments, is caused by the use of a slightly too low back-up plate shear strength. Simulations with a 15% increased shear strength do not show this change of failure mode. Of course, by increasing the impact velocity far above the ballistic limit velocity, these armours will also show shear failure.

7 CONCLUSION

The results and observations from the eight series of impact experiments with blunt steel rods extend the existing database containing detailed information on the penetration processes of standard 7.62 mm AP and 7.62 mm Ball projectiles. Both analytical and hydrocode modelling of impact phenomena on ceramic faced armours can benefit from this database.

The results presented in this report show that the projectile/armour interaction process for rod impact is representative for the interaction process of a 7.62 mm AP projectile impact.

The phenomenological behaviour and break-up process of the Morgan Matroc Hilox 973 alumina facing following a rod impact is described and understood. In most of the impact experiments the projectile was not able to penetrate through the ceramic material directly underneath it. The influence of back-up plate properties such as bending stiffness, shear strength, ultimate strain and tensile strength on the obtained protection level is assessed. The increase of bending stiffness has a positive effect on the obtained protection level for as long as the back-up plate does not fail by plug-shearing. The ballistic performance of armours with back-up plates that do fail by plug-shearing may be enhanced by decreasing the bending stiffness of the back-up plate. This becomes especially important for applique armour systems and armours where the thickness of the ceramic facing is constrained.

The analysis of the experimental results show that the shear failure mode in the back-up plate is caused by a catastrophic loss of load distributing capabilities of the ceramic facing. As early as 20 μ s after impact the armour's inability to defeat the projectile is clearly visible.

The simulations with the ALARM model show that with a limited amount of empirical data, the model is able to accurately predict ballistic limit velocities ($\pm 10\%$). The armour failure modes at the ballistic limit velocities calculated with the ALARM model match the experimental data. For impacts below the armour's ballistic limit velocity, the projectile and armour deformation processes match the experimental evidence very well. For rod impacts which cause back-up plate plug-shearing, the predicted deformation process shows the shear failure mode to occur later in time. In its present form, the ALARM model is not capable of predicting the rapid decrease of load-distribution capability of the ceramic facing as indicated by the experimental evidence.

The change of failure mode, calculated by the ALARM model for the armours with the 4.0 mm and 2*3.0 mm thick back-up plates, when the impact velocity of the rods is increased, shows the

importance of using the "correct" material properties. One should apply extreme care when analysing the results of simulations which include for example, strain-rate sensitive materials.

8 RECOMMENDATIONS

Based on the observations and results presented, a number of recommendations for future research and model development are proposed.

The accuracy of the radiograph analysis procedure prevents the discrimination between early time ($<16 \mu\text{s}$) responses of the various back-up plates. Streak photography or VISAR interferometry experiments can be used to accurately measure the armour response during the first $20 \mu\text{s}$ of the impact process.

Impact experiments with short projectiles ($L/D < 1$) allow the development of the initial ceramic fracture conoid to be studied. Combined analysis with the streak photography or VISAR results may result in an improved understanding of the events, leading to the further confirmation of the presented phenomenological description of events. In particular, the events leading to the ceramic's catastrophic loss of load-carrying capabilities need further investigation.

In addition, the influence of projectile material and geometry on the ballistic limit velocity of ceramic faced armours need to be assessed. A preliminary study on this topic, showing the influence of the projectile geometry on the ballistic limit velocity, is presented in ref. [38]. According to this study, the ballistic protection level changed only marginally when the rod's length over diameter ratio was varied from 2.2 to 9.7. All these armours had relatively thin back-up plates (4.0 mm aluminium 6061-T6). Their failure was observed to be primarily caused by too high tensile strains. The results presented in this report indicate that the failure of armours with stiff back-up plates is caused by a catastrophic loss of load distribution capabilities of the ceramic facing which results in a too high shear-loading of the back-up plate. It is therefore expected that a much larger influence on the ballistic protection level is experienced when these stiff armours are impacted by rods with various length-over-diameter ratios.

Even though the 7.62 mm AP projectile, 7.62 mm Ball projectile and the steel rod inflict a similar response on the target, the influence of the projectile material on the penetration behaviour needs to be assessed further. All the experimental work presented by the author was carried out with one type of alumina (Morgan Matroc Hilox 973). In order to allow the use of other ceramic materials within the ALARM model, ballistic experiments with those materials need to be conducted in order to determine the necessary input parameters. In order to be able to assess the applicability of the model for use with armours with composite back-up plates, ballistic experiments need to be conducted with those materials too.

The comparison between experimental observations and the calculations by the model highlight a number of areas where the analytic model may be improved. The prediction of the armour response for impacts above the ballistic limit velocity may improve significantly when the ceramic's catastrophic loss of load distribution capability is included in the model. This could be accomplished by instantaneously reducing the base area of the ceramic fracture conoid to an area corresponding to that of the projectile when the shear load on the periphery of the loaded section of the back-up plate exceeds its ultimate value.

The model could be improved by the use of a more comprehensive model for the initial phase (the first few microseconds) of the impact process. The evaluation of the back-up plate responses indicate that a more elaborate two-dimensional (elastic-plastic) back-up plate deformation model is expected to match the experimentally observed deformation better.

It is, however, questionable whether the implementation of these improved models leads to more accurate predictions, considering that the ceramic break-up process, governing the creation and deterioration of the ceramic fracture conoid, is understood on a phenomenological basis only.

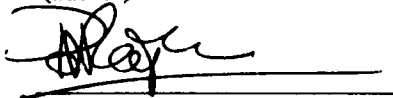
With the behaviour of the (confined) fractured ceramic so difficult to characterize and model, the use of empirical relations are inevitable and unfortunately, to some extent, inaccurate. Hence, it is the author's belief that, depending on the available resources for continued development, the best return on investment is to be expected only from the inclusion in the model of the catastrophic loss of load distribution capabilities by the ceramic.

9 AUTHENTICATION

The development of the steel rod, the sabot, the launch technique and the experimental set-up was supervised by Mr Van Riet and carried out by Mr Broos, Mr Zandvliet and Mr Bakker. The flash X-ray experiments described in this report were largely supervised by Mr Van Dijk, and executed by Mr Van der Heijden, Mr Hilvers and Mr Baas. Mr IJsselstein is thanked for the coaching, the discussions and valuable suggestions.

Paul C. den Reijer

(author)

A handwritten signature in dark ink, appearing to read 'P. den Reijer', is written over two horizontal lines.

10 REFERENCES

- 1 Abbot, K.H.: Composite Aircraft Armor, Ordnance, May-June 1968, pp. 582-584.
- 2 Alesi, A.L. and Barron, E.R.: Plastic-Ceramic Composite Armor, SPE Journal, vol. 24, July 1968.
- 3 Rolston, R.F.: Breakthrough in Armor, Space/Aeronautics, July 1968, pp. 55-63.
- 4 Taussig Jr., J.K.: Breakthrough in Armor, Ordnance, July-August 1970, p.71.
- 5 Taussig Jr., J.K.: Ceramics for Defense, Ordnance, July-August 1970, pp. 292-294.
- 6 Bodine, E.G. et al.: The Optimization of Composite Ceramic-Armor Materials, p. 21 in Ceramic-Armor Technology Proceedings of Symposium, DCIC Report 69-1 part I, 1969.
- 7 Bless, S.J.: Impact Behaviour of Ceramics, University of Dayton Research Institute, 1986.
- 8 Florence, A.L. and Ahrens, T.J.: Interaction of Projectiles and Composite Armor, Final Report, Stanford Research Institute, AMRA CR 67-05 (F), January 1967.
- 9 Florence, A.L.: Interaction of Projectiles and Composite Armor, Part II, Stanford Research Institute, AMRA CR 69-15, August 1969.
- 10 Johnson, W.: Impact Strength of Materials, Edward Arnold, 1972.
- 11 Wimmer, J.M. et al.: Impact Resistance of Structural Ceramics, Air Force Materials Laboratory, AD-A037165, December 1976.
- 12 Woidneck, C.P.: Keramikbeschichtete Metall- und Faserverstaerkte Panzerungen, Deutsch-Franzoesisches Forchungsintitut Saint-Louis (ISL), ISL-S-CO-916/78, October 1978.
- 13 Wilkins, M.L.: Mechanics of Penetration and Perforation, Int. J. Engng. Sci., vol. 16, pp. 793-807.

- 14 Wilkins, M.L. et al.: An Approach to the Study of Light Armor, Lawrence Radiation Laboratory, UCRL-50284, 1967.
- 15 Wilkins, M.L. et al.: Second Progress Report on Light Armor Program, Lawrence Radiation Laboratory, UCRL-50349, 1967.
- 16 Wilkins, M.L. et al.: Third Progress Report on Light Armor Program, Lawrence Radiation Laboratory, UCRL-50460, 1968.
- 17 Wilkins, M.L. et al.: Fourth Progress Report on Light Armor Program, Lawrence Radiation Laboratory, UCRL-50694.
- 18 Wilkins, M.L. et al.: Fifth Progress Report on Light Armor Program, Lawrence Radiation Laboratory, UCRL-50980.
- 19 Wilkins, M.L.: Use of Boron Compounds in Lightweight Armor, in Boron and Refractory Borides, edited by V.I. Matkovich, Springer-Verlag, 1977.
- 20 Mescall, J.F. and Tracy, C.A.: Improved Modelling of Fracture in Ceramic Armours, U.S. Army Materials Technology Laboratory, Watertown, MA, U.S.A., June 1986.
- 21 Anderson Jr, C.E. and Bodner, S.R.: Ballistic Impact: The Status of Analytical and Numerical Modelling, Int. J. Impact Engng., vol. 7, no. 1, 1988, pp. 9-35.
- 22 Graaf, H. van de: Validation of Ceramics Material Modelling in Impact/Penetration Calculations, Technical report TR-88-591.2/01, Pisces International B.V., January 1988.
- 23 Johnson, G.R. and Holmquist, T.J.: A Computational Constitutive Model for Brittle Materials Subjected to Large Strains, High Strain Rates, and High Pressures, proceedings Explomet, San Diego, California, August 1990.
- 24 Kennedy, C.M. et al.: Analysis of Impacts on Alumina, Armor and Materials Department, FMC Ordnance Division, San Jose, California.

- 25 Reijer, P.C. den: Studiereis Keramische Pantser in de Verenigde Staten, PML 1988-RV5, Prins Maurits Laboratory, The Netherlands, November 1988, in Dutch.
- 26 Prior, A.M. and Hetherington, J.G.: The Penetration of Composite Armour by Small Arms Munition, proceedings of the ninth International Symposium on Ballistics, 1986.
- 27 Ravid, M. et al.: Application of Two-Dimensional Analytical Models of Ballistic Penetration to Ceramic Armor, Proceedings 11th International Symposium on Ballistics, Brussels, Belgium, May 9-11, 1989.
- 28 Mayselless, M. et al.: Impact on Ceramic Faced Targets, Journal of Applied Mechanics, vol. 54, June 1987.
- 29 Reijer, P.C. den: Ballistic Arall First Progress Report, PML 1987-C101, Prins Maurits Laboratory, The Netherlands, August 1987.
- 30 Reijer, P.C. den: The TNO Analytic Ceramic Faced Lightweight Armour Response Model (Theory and Results), PML 1989-C145, Prins Maurits Laboratory, The Netherlands, September 1989.
- 31 Reijer, P.C. den: The TNO Analytic Ceramic Faced Lightweight Armour Response Model (Source and Examples), PML 1989-C156, Prins Maurits Laboratory, The Netherlands, September 1989.
- 32 Reijer, P.C. den: Penetration of 7.62 mm Projectiles into Ceramic Faced Armour, proceedings 11th International Symposium on Ballistics, Brussels, May 1989.
- 33 Reijer, P.C. den: Further Development of the TNO Analytic Ceramic Faced Lightweight Armour Response Model (ALARM), PML 1990-C17, Prins Maurits Laboratory, The Netherlands, February 1990.
- 34 Reijer, P.C. den: An Experimental Study of 7.62 mm Projectiles Penetrating Ceramic Faced Lightweight Armours, PML 1990-C79, Prins Maurits Laboratory, The Netherlands, August 1990.

- 35 Reijer, P.C. den and IJsselstein, R.R: A Novel Flash X-ray Technique to Determine Projectile Ceramic Armour Interaction, proceedings 12th International Symposium on Ballistics, San Antonio, October 1990.
- 36 Wilkins, M.L.: Personal Correspondance to P.C. den Reijer, 1988.
- 37 Held, M.: Flash X-Radiography in Ballistics, Materials Evaluation, no. 43, August 1985, pp. 1104-1123.
- 38 Zuidam, D-J.A. van: Een Onderzoek naar de Invloed van de Projectielgeometrie op de Penetratiecapaciteit in Keramische Pantsers, Koninklijke Militaire Academie, September 1990, in Dutch.
- 39 Swift, H.F. and Strange, D.E.: Analysis of Sabot Operation, Physics Applications Inc., Dayton, Ohio.
- 40 Swift, H.F. and Strange, D.E.: Sabot Disc. rd Technology, Physics Applications Inc., Dayton, Ohio, October 1, 1987.
- 41 Hornemann, U. et al.: Experimental Investigation of Wave and Fracture Propagation in Glass Slabs by Steel Cylinders at High Impact Velocities, proceedings third Conf. Mech. Prop High Rates of Strain, Oxford, 1984.
- 42 Bless, S.J.: Hypervelocity Penetration of Ceramics, Int. J. Impact Engng., Vol. 5, pp. 165-171, 1987.
- 43 Rosenberg, Z. et al.: On the Influence of the Loss of Shear Strength on the Ballistic Performance of Brittle Solids, Int. J. Impact Engng., Vol. 9, No. 1, pp. 45-49, 1990.
- 44 Timoshenko, S.P. and Goodier, J.N.: Theory of Elasticity, McGraw-Hill, ISBN 0-07-Y85805-5.
- 45 Evans, A.G.: Strength Degradation by Projectile Impacts, Journal of the American Ceramic Society, vol. 56, no. 8, August 1973.

- 46 Shockey, D.A. et al.: Failure Phenomenology of Confined Ceramic Targets and Impacting Rods, Int. J. Impact Engng., vol. 9, no. 3, pp. 263-275, 1990.
- 47 Frechette, V.D. and Cline, C.F.: Fractography of Ballistically Tested Ceramics, Ceramic Bulletin, vol. 49, no. 11, 1970.
- 48 Viechnicki, D. et al.: Armor Ceramics 1987, Proceedings of the Third TACOM Armor Coordinating Conference, 17-19 February 1987, Monterey, California.
- 49 Rosenberg, Z. and Tsaliah, J.: Applying Tate's Model for the Interaction of Long Rod Projectiles with Ceramic Targets, Int. J. Impact Engng., vol. 9, no. 2, pp. 247-251, 1990.
- 50 Laible, R.C. (editor): Ballistic Materials and Penetration Mechanics, Elsevier Scientific Publishing Company, ISBN 0-444-41928-4, 1980.

11 TABLES

Table 1 Comparison of the experimentally obtained and ALARM-operated ballistic limit velocities and failure model for armours of 8.1 mm thick alumina supported by aluminium when impacted by blunt steel rods

Back-up plate thickness [mm]	ballistic limit velocity [m/s]		failure mode	
	experiment	simulation	experiment	simulation
3.0		668		
3.5		729		
4.0	786 - 829	788	strain and shear	strain
4.5		829		
5.0		852		
5.5		878		
6.0	815 - 916	905	shear	shear
2*3.0	818 - 938	902	shear and strain	shear and strain
6.5		935		
7.0		964		
7.5		996		
8.0	995 - 1091	1033	shear	shear
8.5		1071		
9.0		1115		
9.5		1163		

Table 2 Comparison of experimentally obtained and ALARM-generated max. back-up plate deformation, residual projectile mass and failure mode for armours of 8.1 mm thick alumina supported by aluminium when impacted by blunt steel rods with velocities below and above their ballistic limit

Back-up plate thickness [mm]	impact velocity [m/s]	max. deformation		residual projectile mass		failure mode	
		[mm]		[*10 ⁻³ kg]			
		experiment	simulation	experiment	simulation	experiment	simulation
4.0	786	11	16	2.4	3.6	-	-
4.0	829	-	-	2.4	3.5	strain & shear	shear
6.0	815	5	5	2.6	3.0	-	-
6.0	916	-	-	2.3	2.7	shear	shear
2*3.0	819	11	12	2.4	3.2	-	-
2*3.0	938	-	-	2.3	2.8	shear & strain	shear
8.0	995	7	5	1.8	2.0	-	-
8.0	1091	-	-	2.6	2.1	shear	shear

12 FIGURES

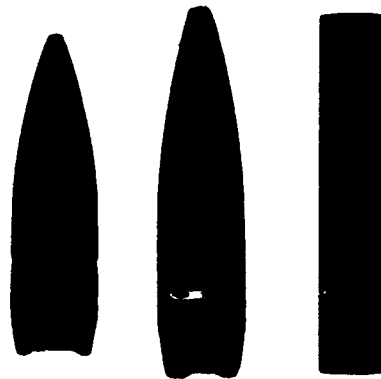


Figure 1 The 7.62 mm armour piercing projectile (left) and the blunt circular cylindrical steel rod

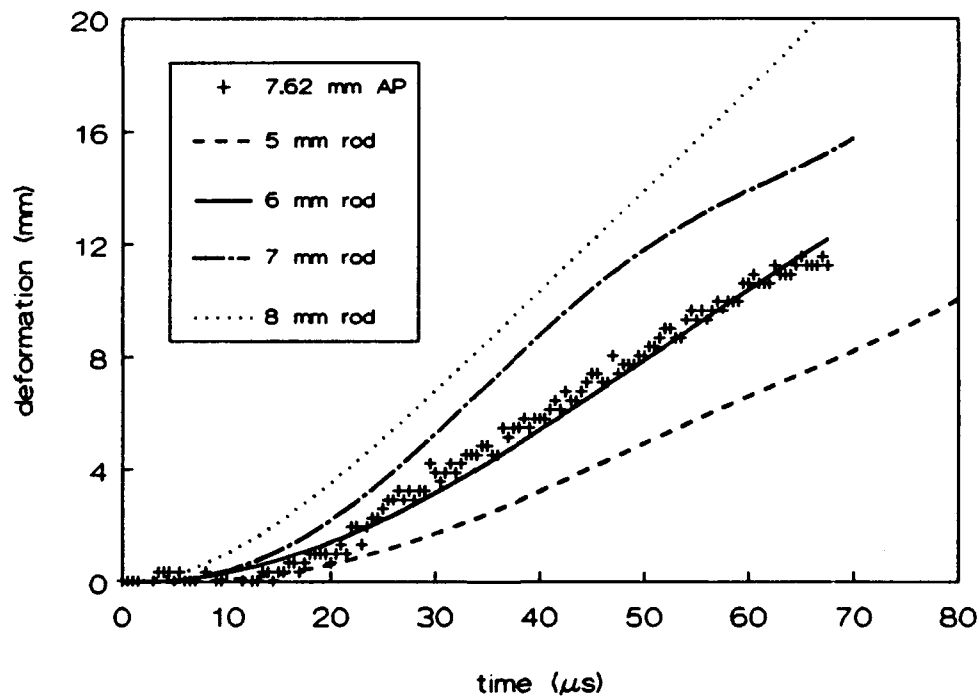


Figure 2 Comparison between the maximum back-up plate deformations of targets of 10 mm alumina backed by 4.0 mm aluminium when impacted by the 7.62 mm AP projectile and several blunt steel rods at approximately 820 m/s[38]



Figure 3 The projectile/sabot package

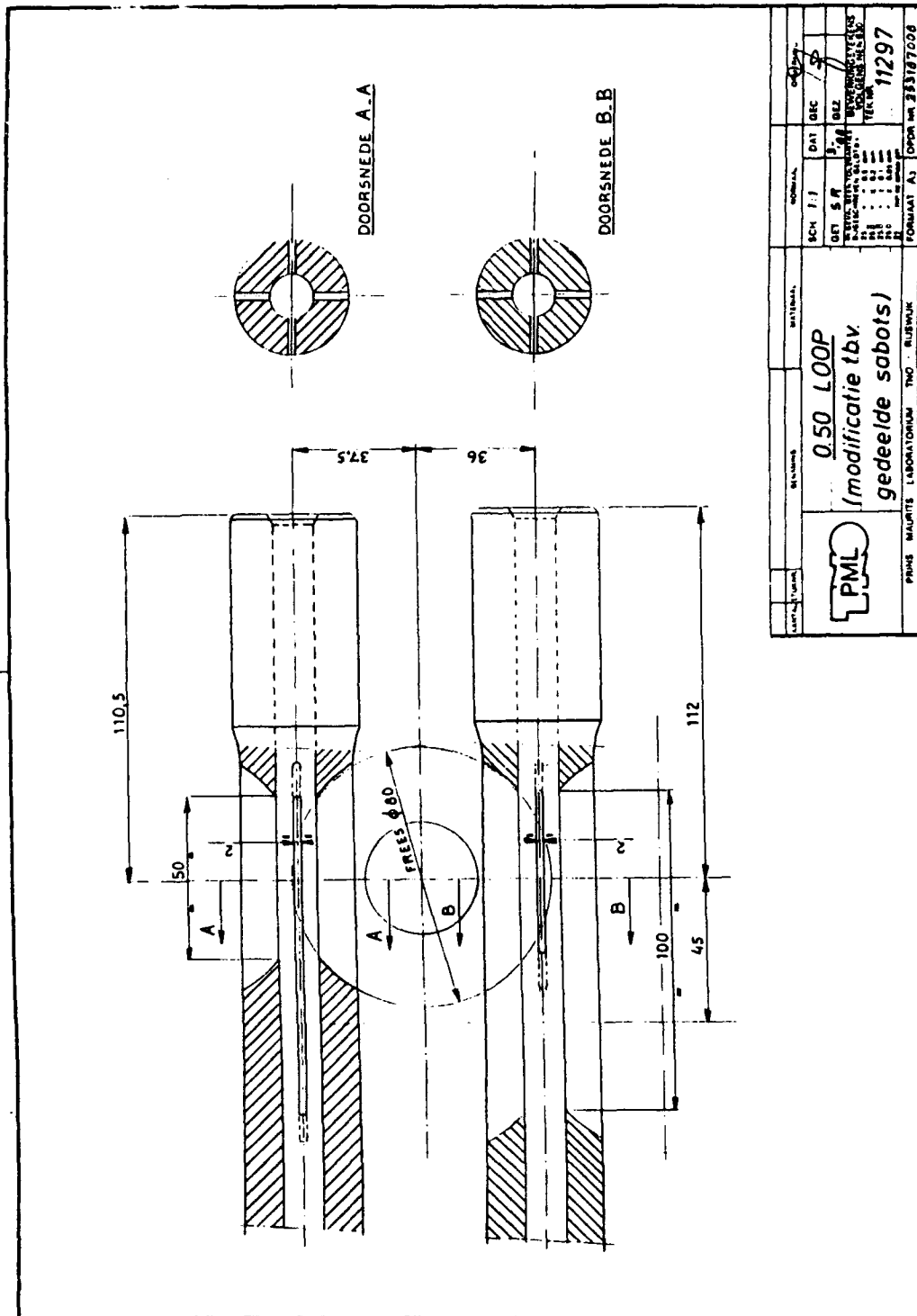


Figure 4 The modified 13.0 mm smooth bore launch-tube



Figure 5 Typical example of an armour panel resulting from the vacuumbag manufacturing process (8.1 mm alumina & 4.0 mm aluminium)

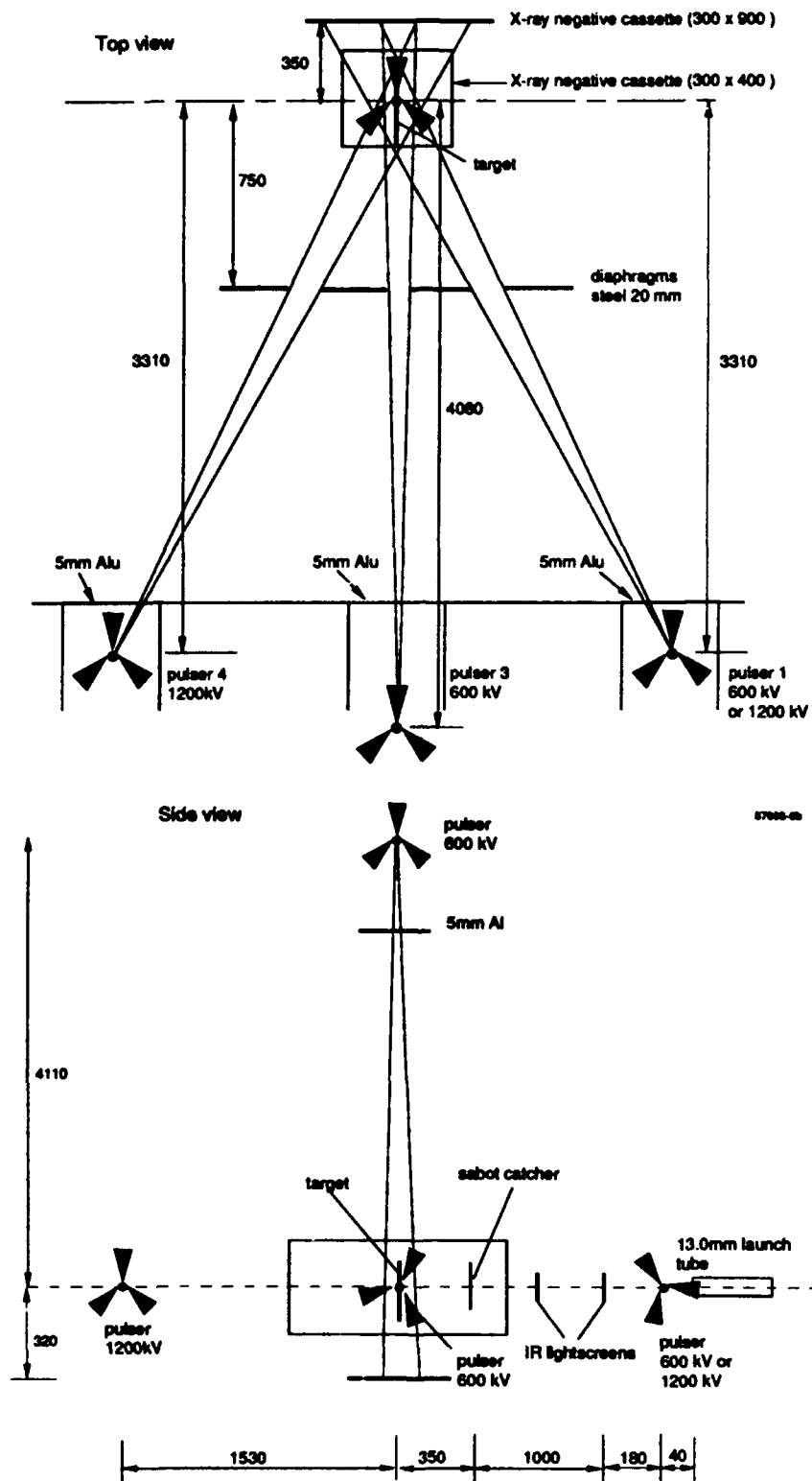


Figure 6

Positions of launch-tube, target, pulsed, diaphragms, X-ray negatives and velocity measurement screens in and around the test chamber



Figure 7a The experimental set-up in and around the test chamber during experiments



Figure 7b The armour panel in its supporting rig

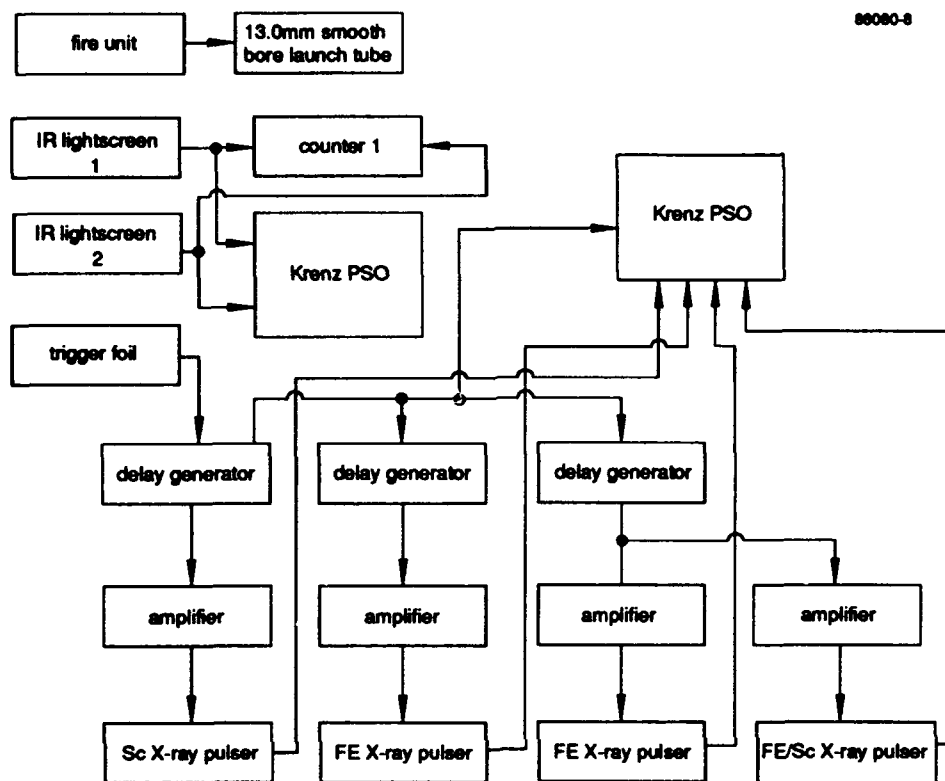


Figure 8 Schematic flowchart of the triggering and measuring equipment set-up

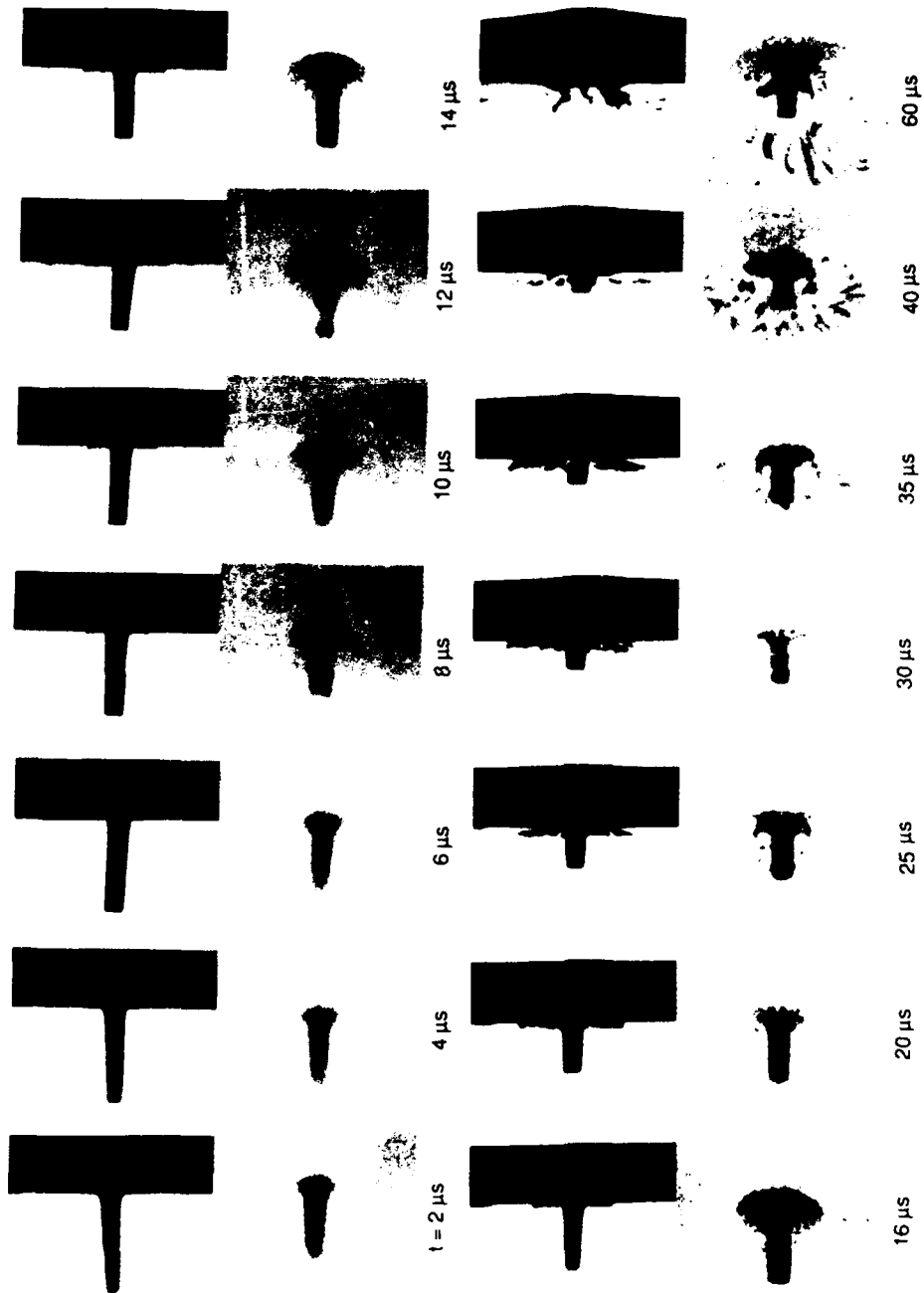


Figure 9 Sequence of normal and oblique (26°) flash radiograph cut-outs showing the projectile/armour interaction of a steel rod impacting 8.1 mm alumina and 6.0 mm aluminium at a velocity below the v_{50} (815 m/s)

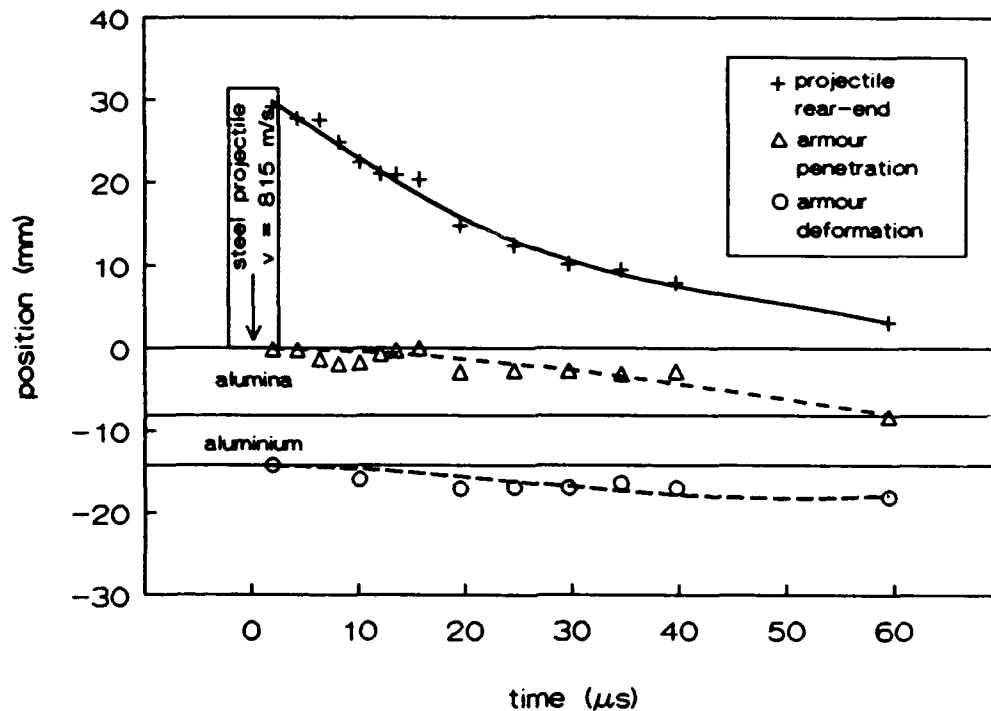


Figure 10 Position versus time curves of a steel rod impacting a target of 8.1 mm alumina backed by 6.0 mm aluminium at a velocity below the v_{50} (815 m/s)

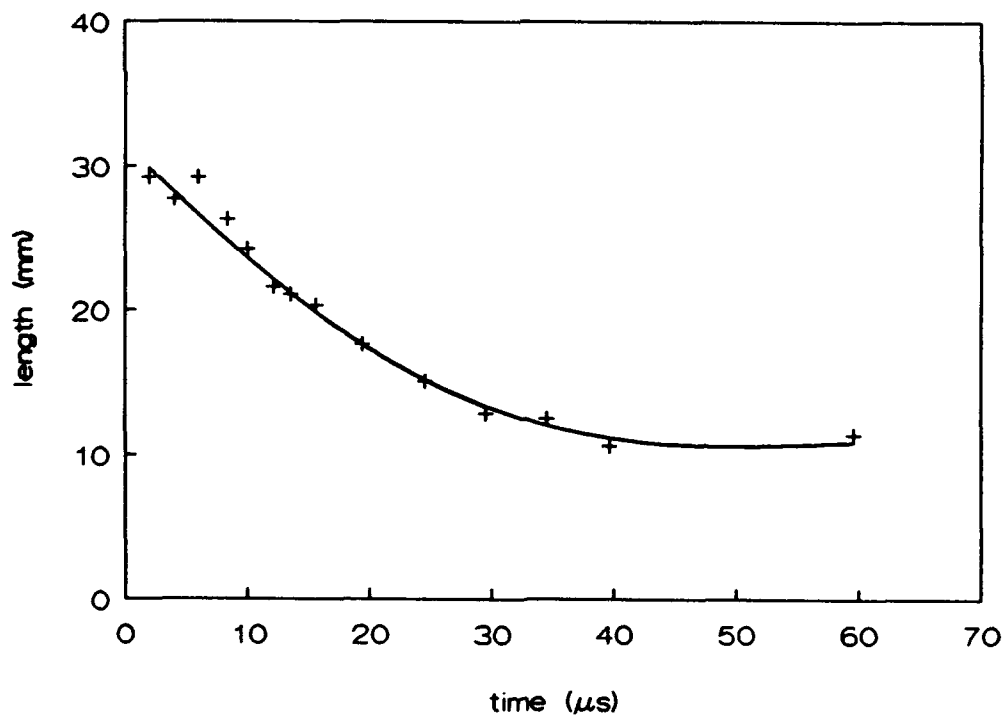


Figure 11 Projectile length versus time curve of the steel rod impacting a target of 8.1 mm alumina backed by 6.0 mm aluminium at a velocity below the v_{50} (815 m/s)



Figure 12 Recovered steel rod after impact of a target of 8.1 mm alumina backed by 6.0 mm aluminium at a velocity below the v_{50} (815 m/s)

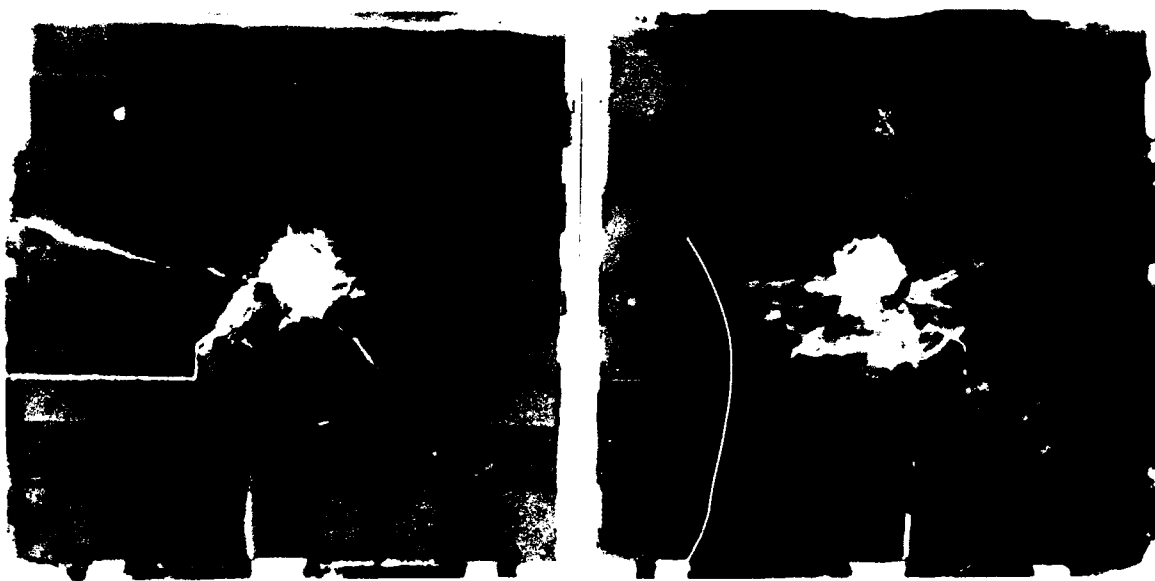


Figure 13 Front and back-face view of a ceramic facing recovered after a steel rod impact into 8.1 mm alumina backed by 6.0 mm aluminium at a velocity below the v_{50} (815 m/s)

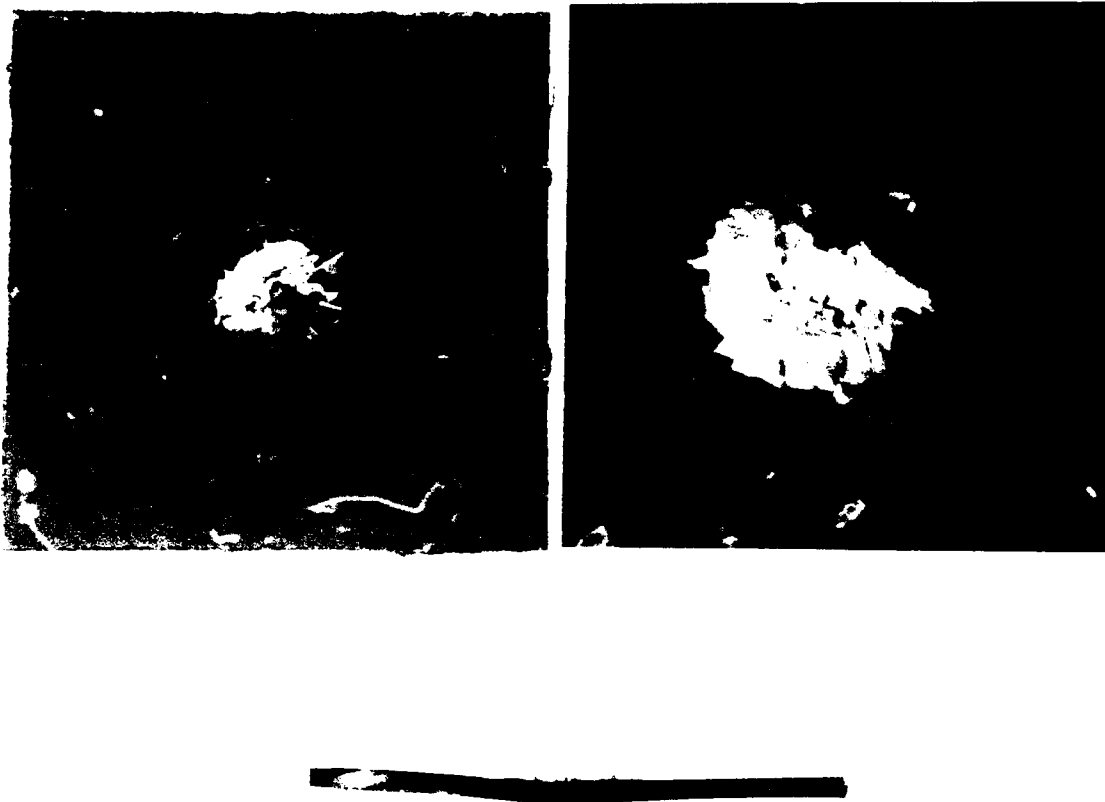


Figure 14 Front, detail and side view (cut through) of a back-up plate recovered after a steel rod impact into 8.1 mm alumina backed by 6.0 mm aluminium at a velocity below the v_{50} (815 m/s)

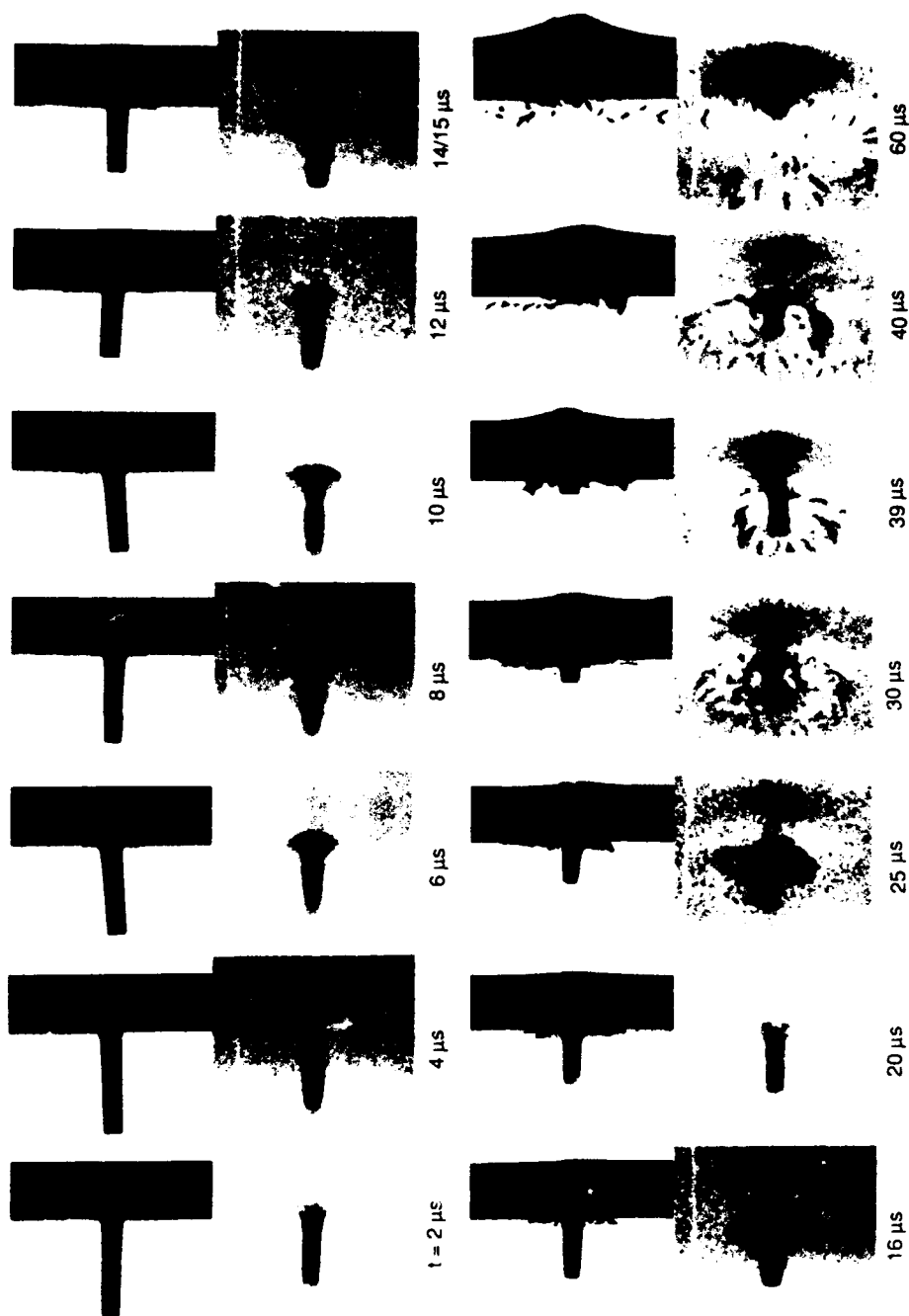


Figure 15 Sequence of normal and oblique (26°) flash radiograph cut-outs showing the projectile/armour interaction of a steel rod impacting 8.1 mm alumina and 6.0 mm aluminium at a velocity above the v_{50} (> 1.5 m/s)

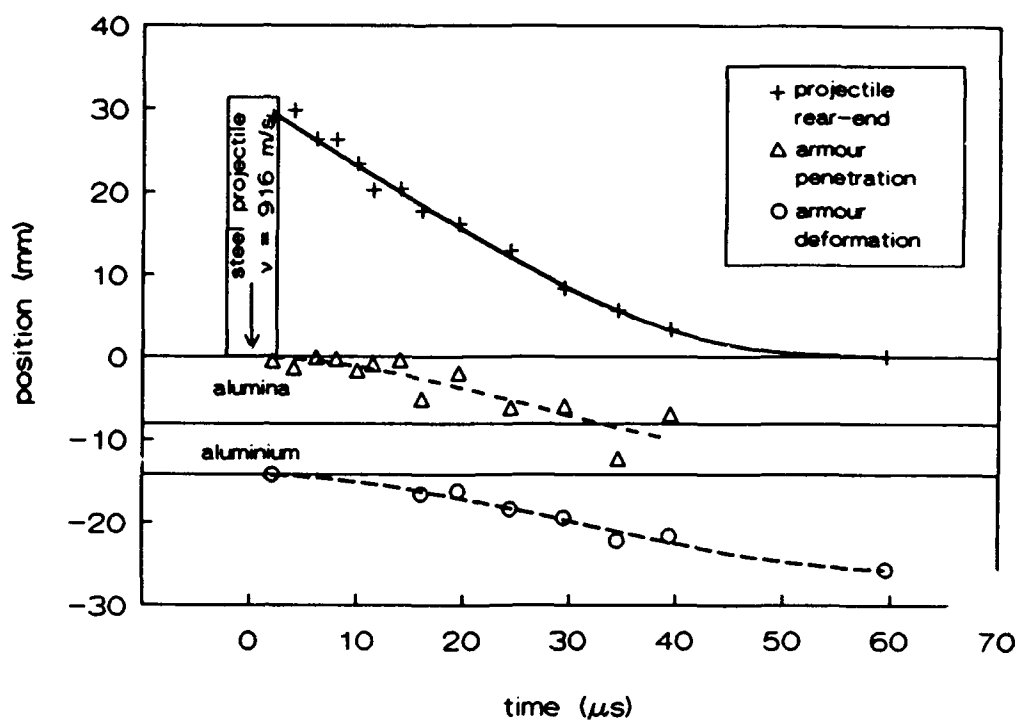


Figure 16 Position-versus-time curves of the steel rod impacting a target of 8.1 mm alumina backed by 6.0 mm aluminium at a velocity above the v_{50} (916 m/s)

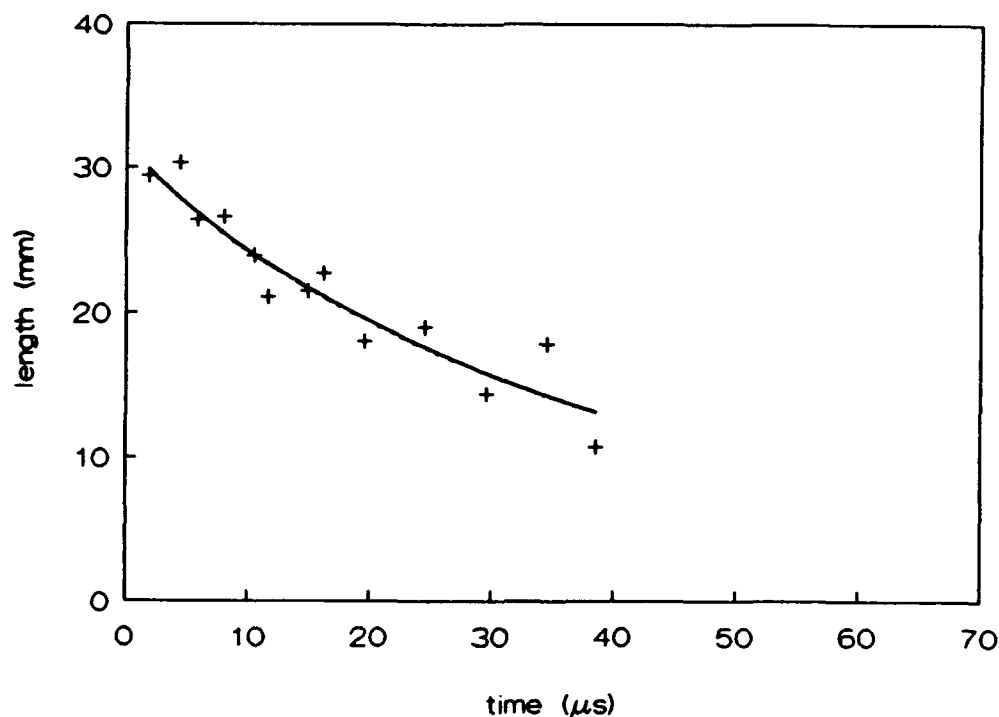


Figure 17 Projectile length versus time curve of the steel rod impacting a target of 8.1 mm alumina backed by 6.0 mm aluminium at a velocity above the v_{50} (916 m/s)

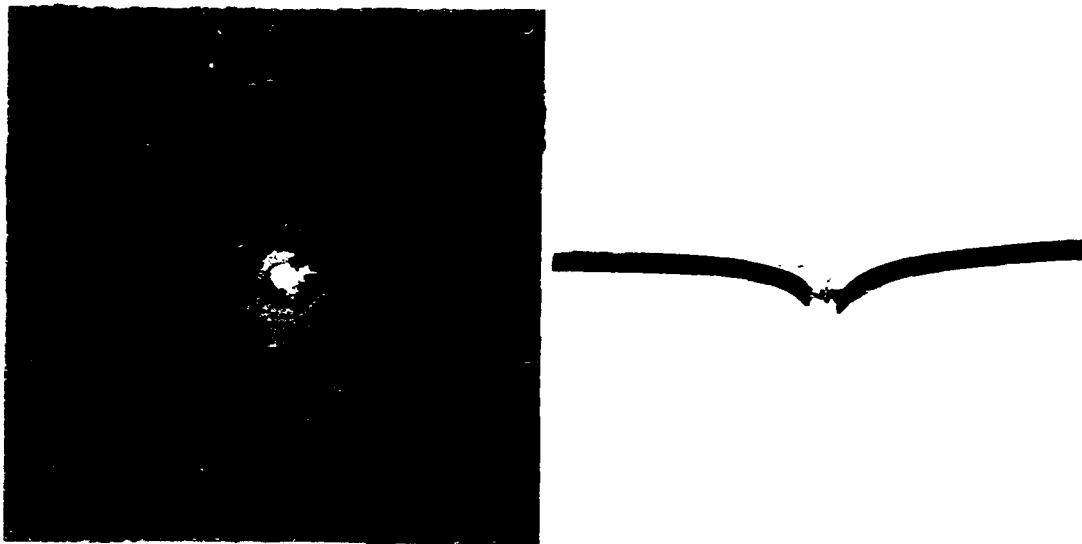


Figure 18 Front and side view (cut through) of a back-up plate recovered after a steel rod impact into 8.1 mm alumina backed by 6.0 mm aluminium at a velocity above the v_{50} (916 m/s)

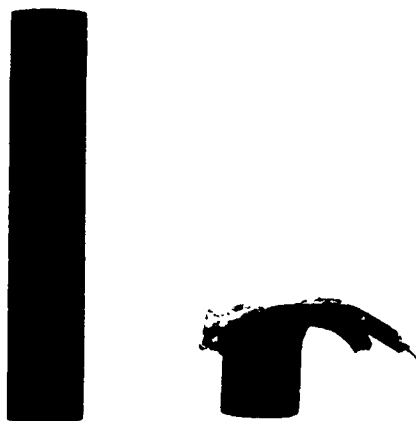


Figure 19 Recovered steel rod after impact of a target of 8.1 mm alumina backed by 6.0 mm aluminium at a velocity above the v_{50} (916 m/s)

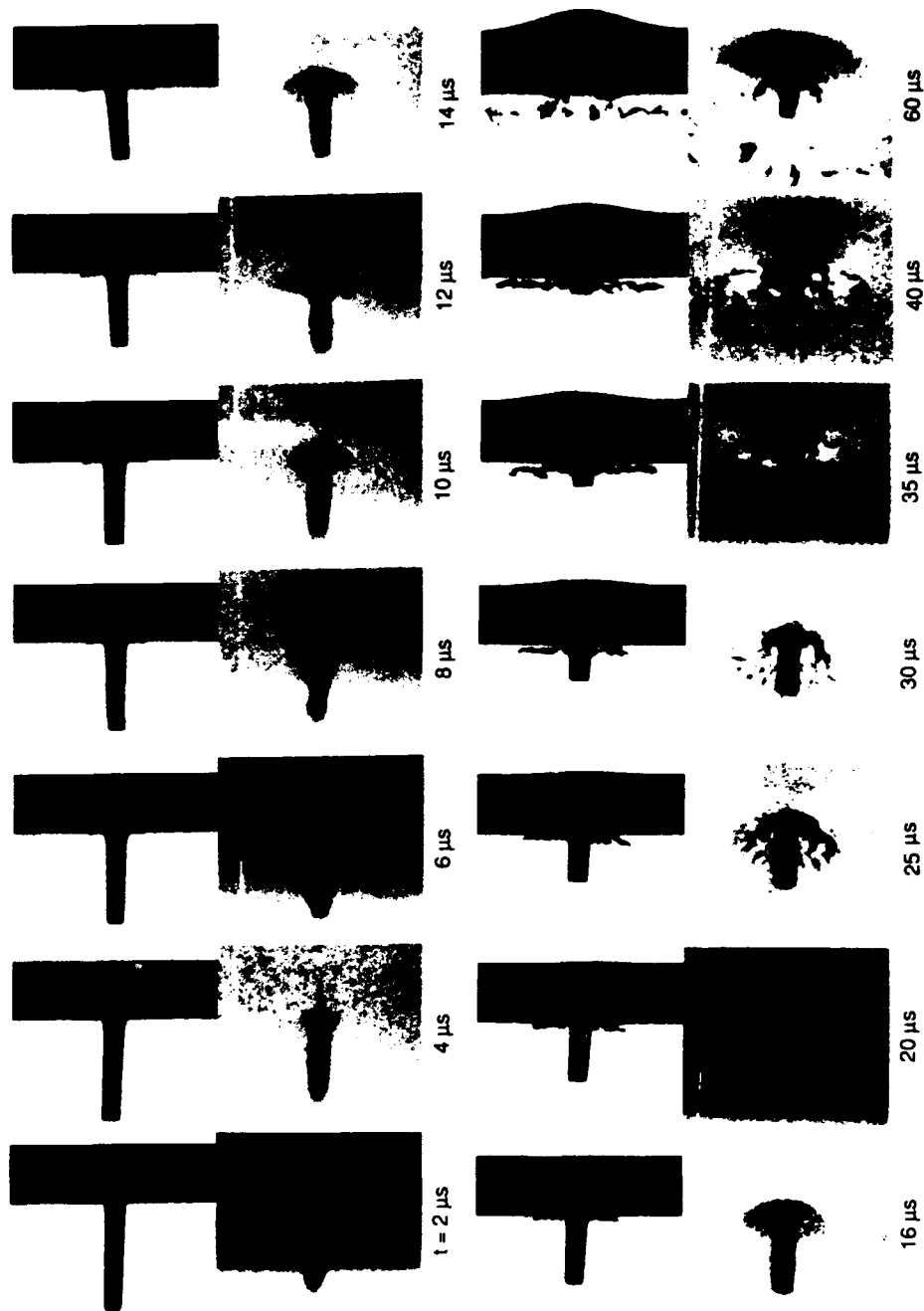


Figure 20 Sequence of normal and oblique (26°) flash radiograph cut-outs showing the projectile/armour interaction of a steel rod impacting 8.1 mm alumina and two 3.0 mm thick layers aluminium at a velocity below the v_{50} (819 m/s)

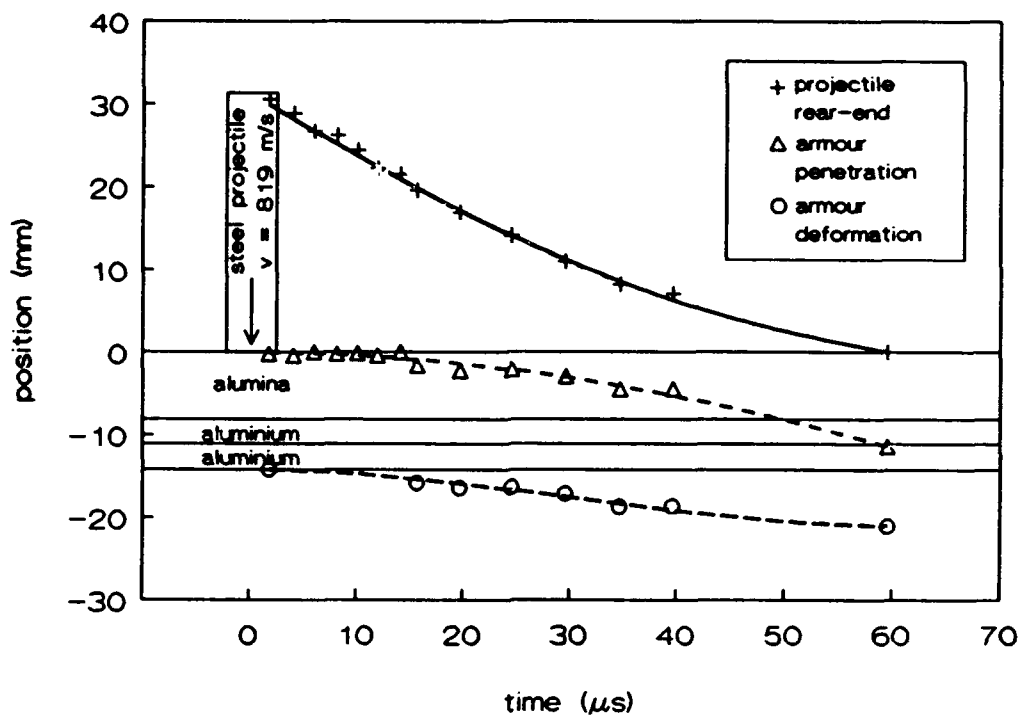


Figure 21 Position-versus-time curves of a steel rod impacting a target of 8.1 mm alumina backed by two 3.0 mm thick layers of aluminium at a velocity below the v_{50} (819 m/s)

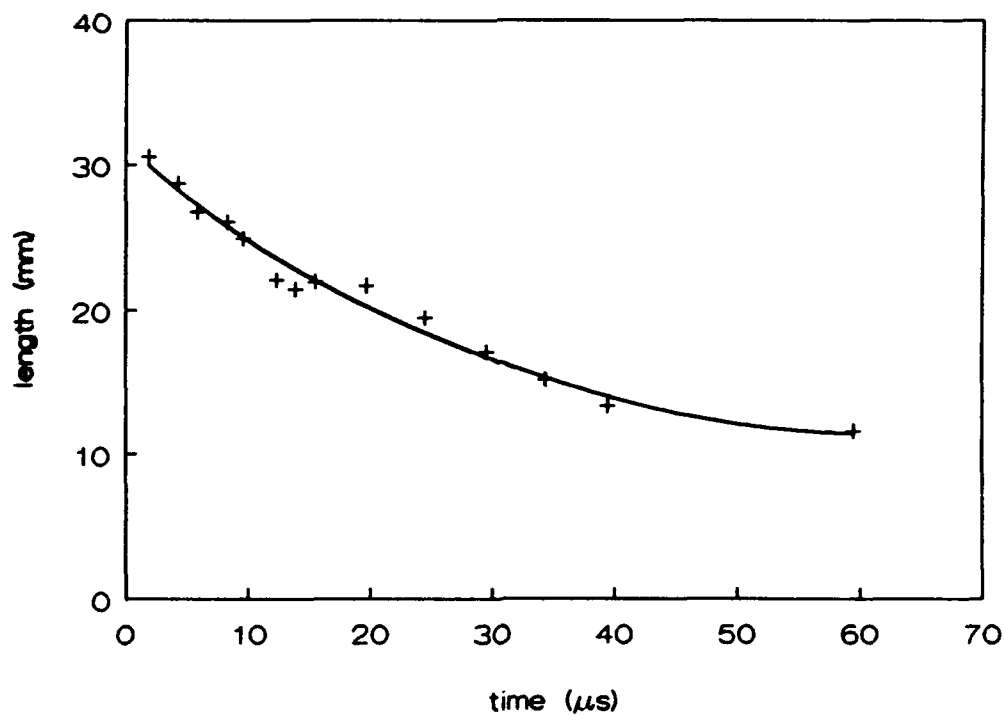


Figure 22 Projectile length-versus-time curve of a steel rod impacting a target of 8.1 mm alumina backed by two 3.0 mm thick layers of aluminium at a velocity below the v_{50} (819 m/s)



Figure 23 Recovered steel rod after impact of a target of 8.1 mm alumina backed by two 3.0 mm thick layers of aluminium at a velocity below the v_{50} (819 m/s)



Figure 24 Front, detail and side view of a back-up plate recovered after a steel rod impact into 8.1 mm alumina backed by two 3.0 mm thick layers of aluminium at a velocity below the v_{50} (819 m/s)

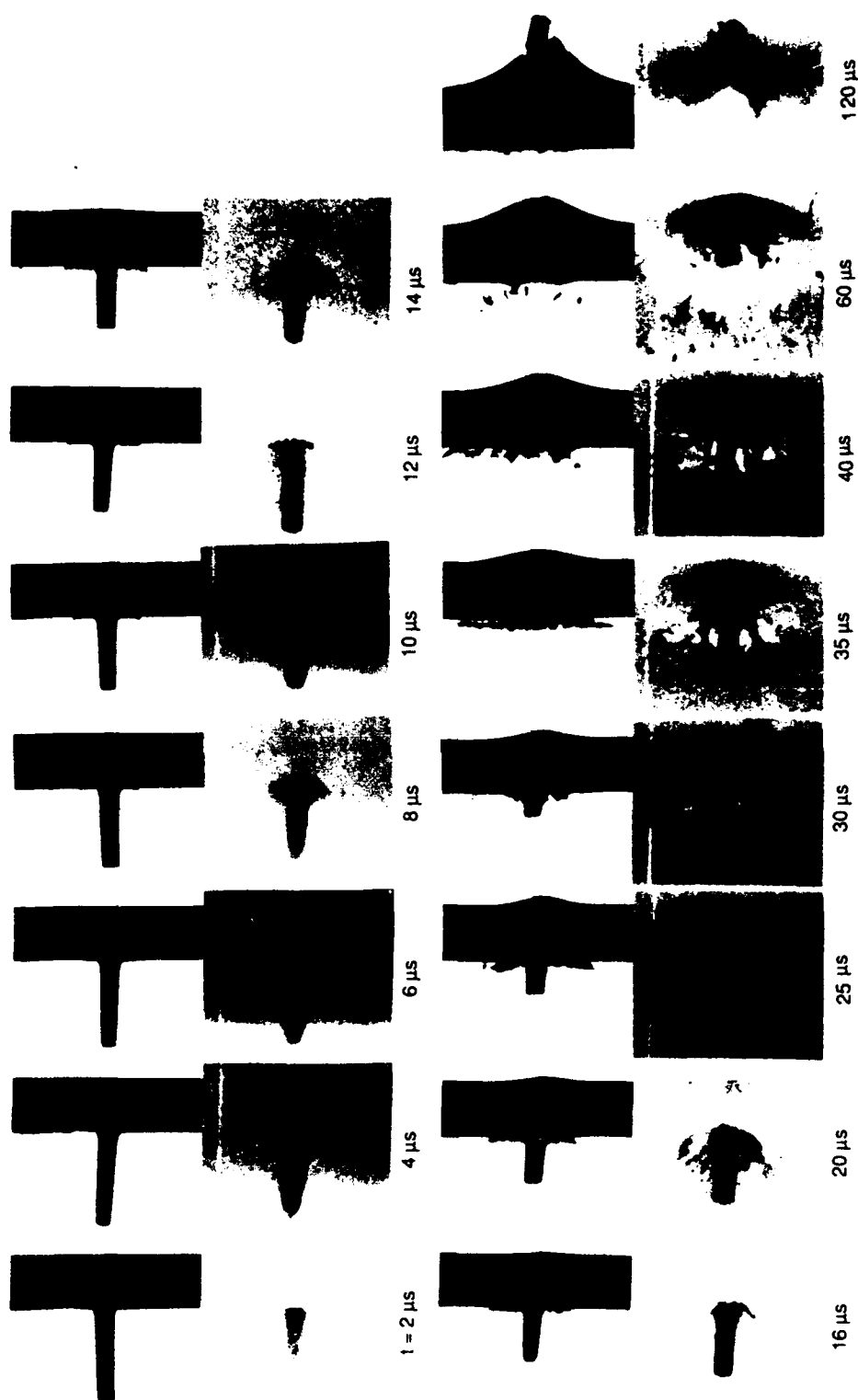


Figure 25 Sequence of normal and oblique (26°) flash radiograph cut-outs showing the projectile/armour interaction of a steel rod impacting 8.1 mm alumina and two 3.0 mm thick layers of aluminium at a velocity above the v_{50} (938 m/s)

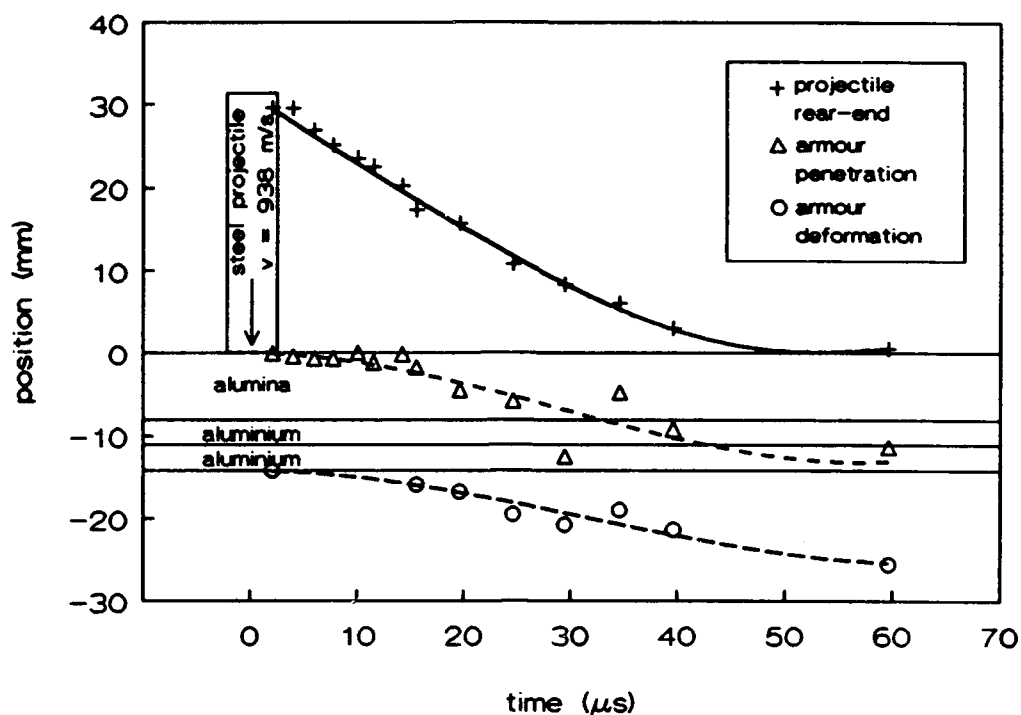


Figure 26 Position-versus-time curves of a steel rod impacting a target of 8.1 mm alumina backed by two 3.0 mm thick layers of aluminium at a velocity above the v_{50} (938 m/s)

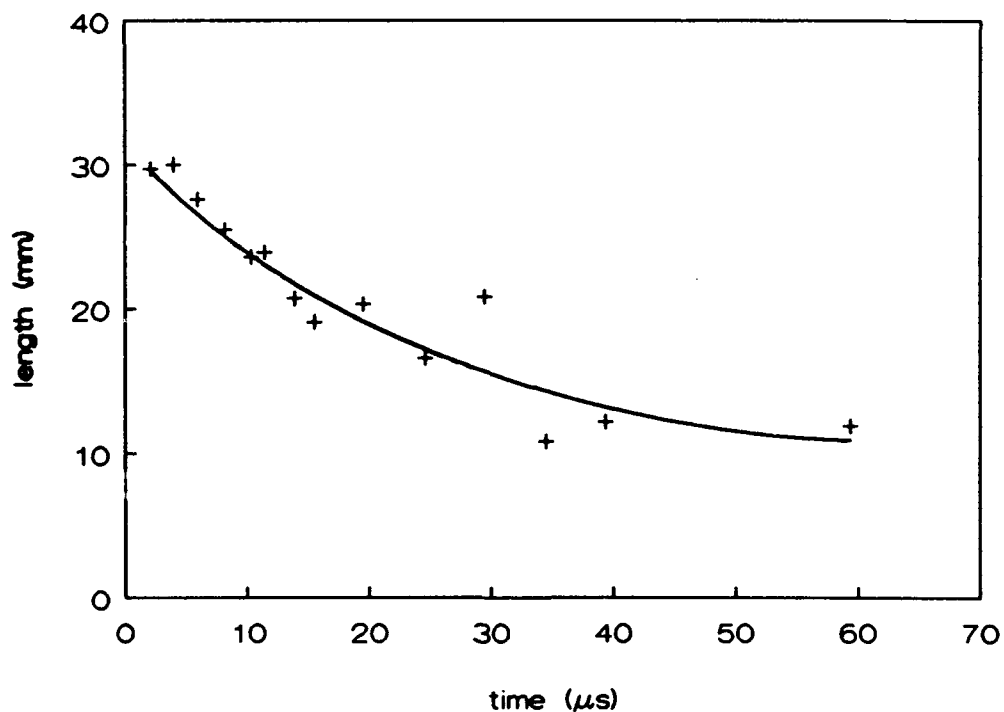


Figure 27 Projectile length-versus-time curve of a steel rod impacting a target of 8.1 mm alumina backed by two 3.0 mm thick layers of aluminium at a velocity above the v_{50} (938 m/s)



Figure 28 Recovered steel rod after impact of a target of 8.1 mm alumina backed by two 3.0 mm thick layers of aluminium at a velocity above the v_{50} (938 m/s)

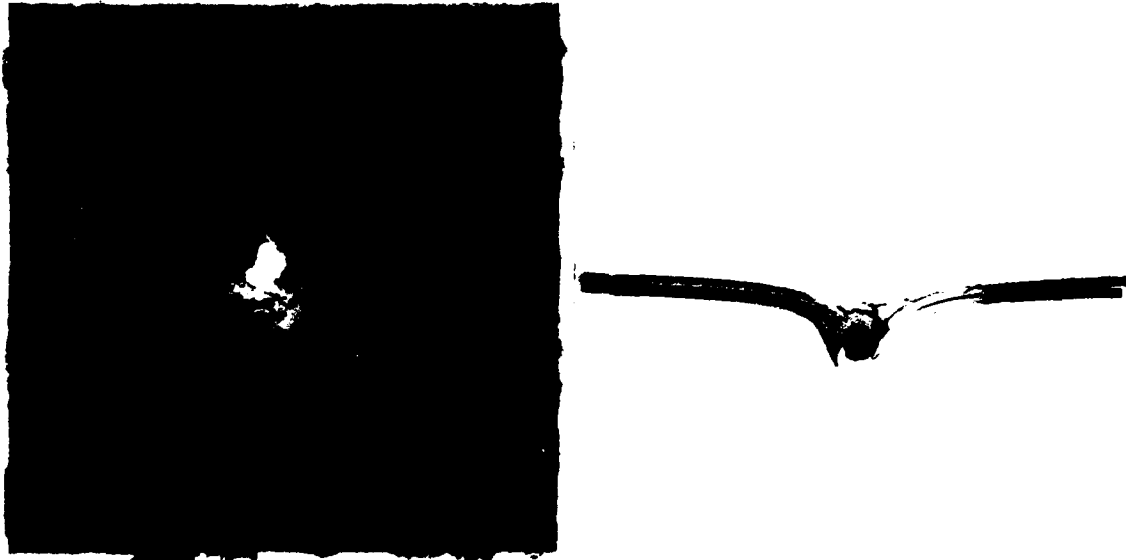


Figure 29 Front and side view (cut through) of a back-up plate recovered after a steel rod impact into 8.1 mm alumina backed by 4.0 mm aluminium at a velocity above the v_{50} (938 m/s)

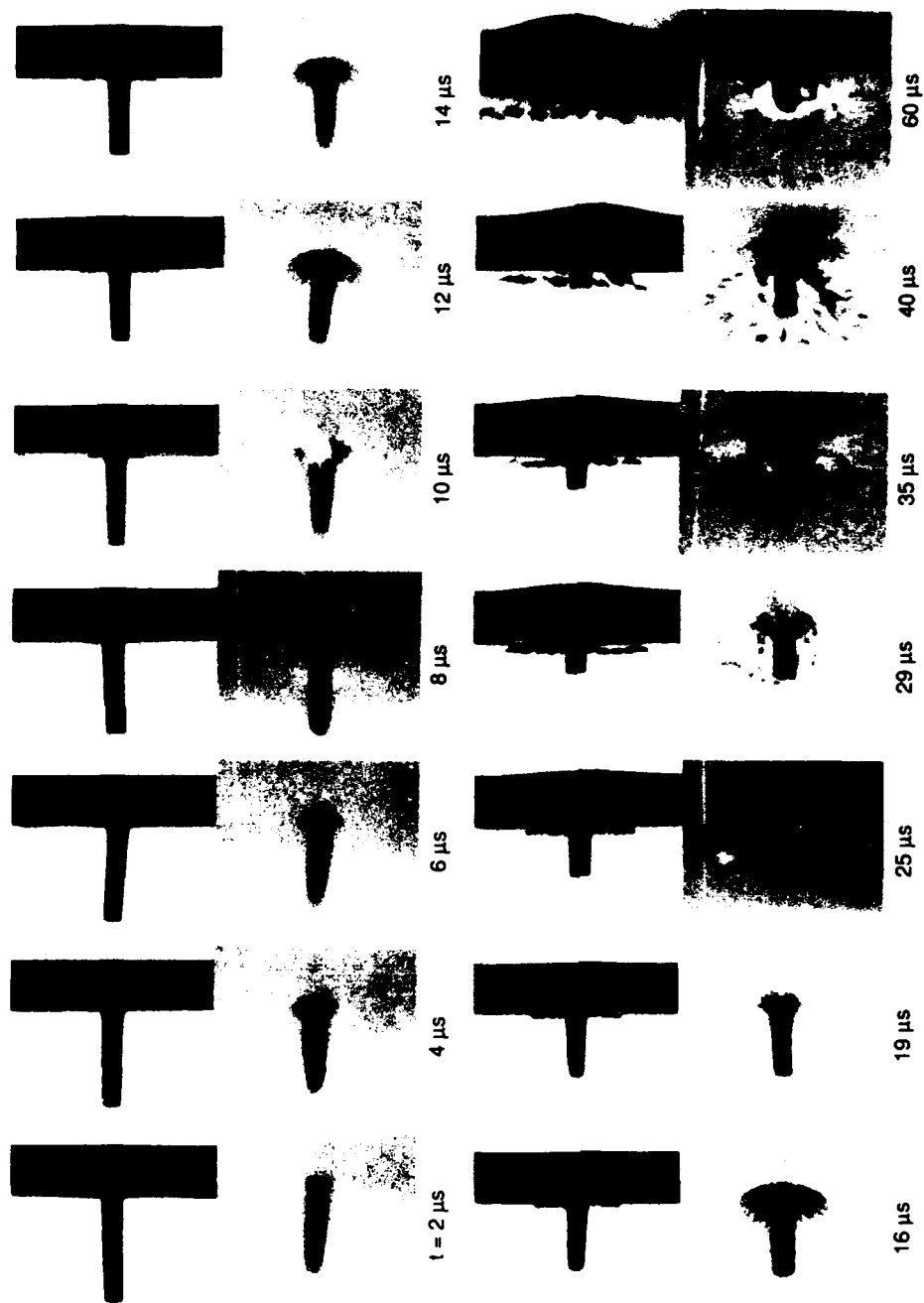


Figure 30 Sequence of normal and oblique (26°) flash radiograph cut-outs showing the projectile/armour interaction of a steel rod impacting 8.1 mm alumina and 4.0 mm aluminium at a velocity below the v_{50} (786 m/s)

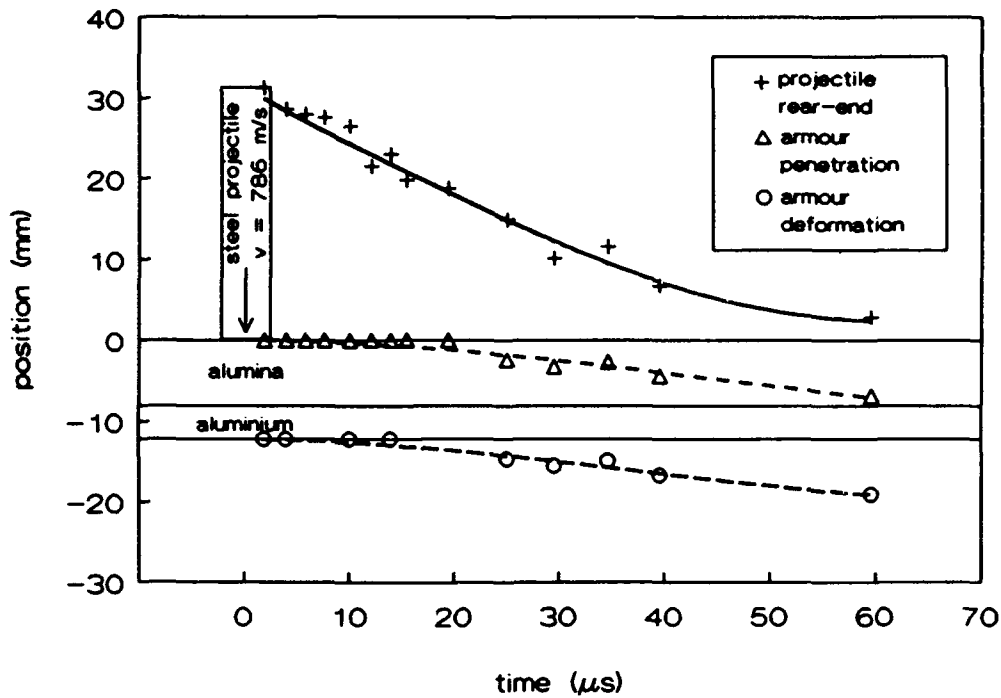


Figure 31 Position versus time curves of the steel rod impacting a target of 8.1 mm alumina backed by 4.0 mm aluminium at a velocity below the v_{50} (786 m/s)

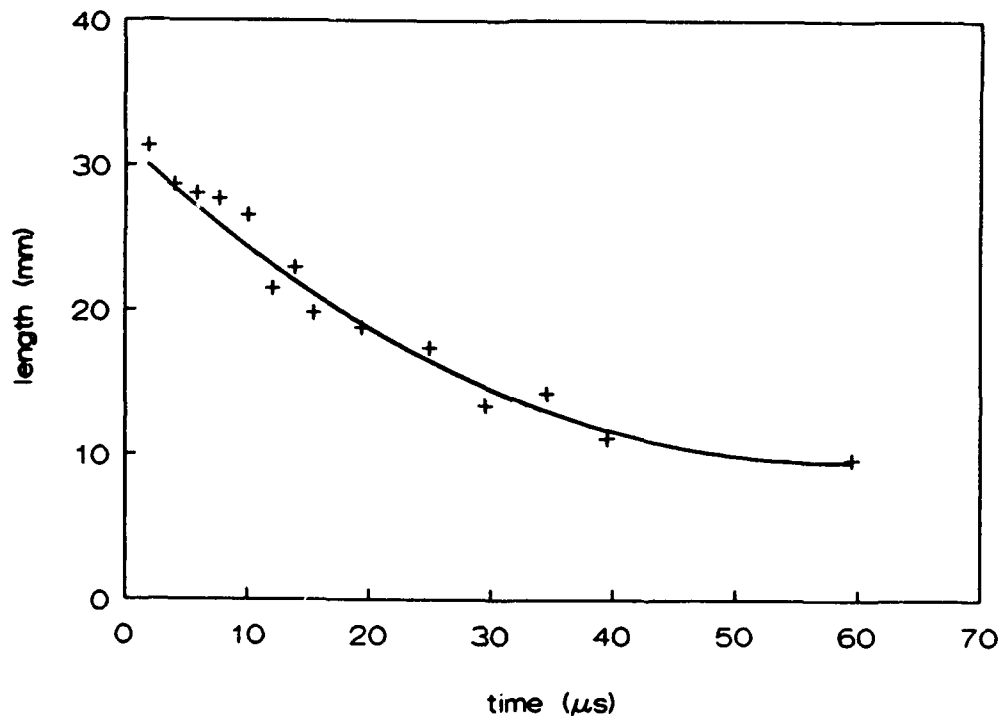


Figure 32 Projectile length-versus-time curve of the steel rod impacting a target of 8.1 mm alumina backed by 4.0 mm aluminium at a velocity below the v_{50} (786 m/s)



Figure 33 Recovered steel rod after impact of a target of 8.1 mm alumina backed by 4.0 mm aluminium at a velocity below the v_{50} (786 m/s)

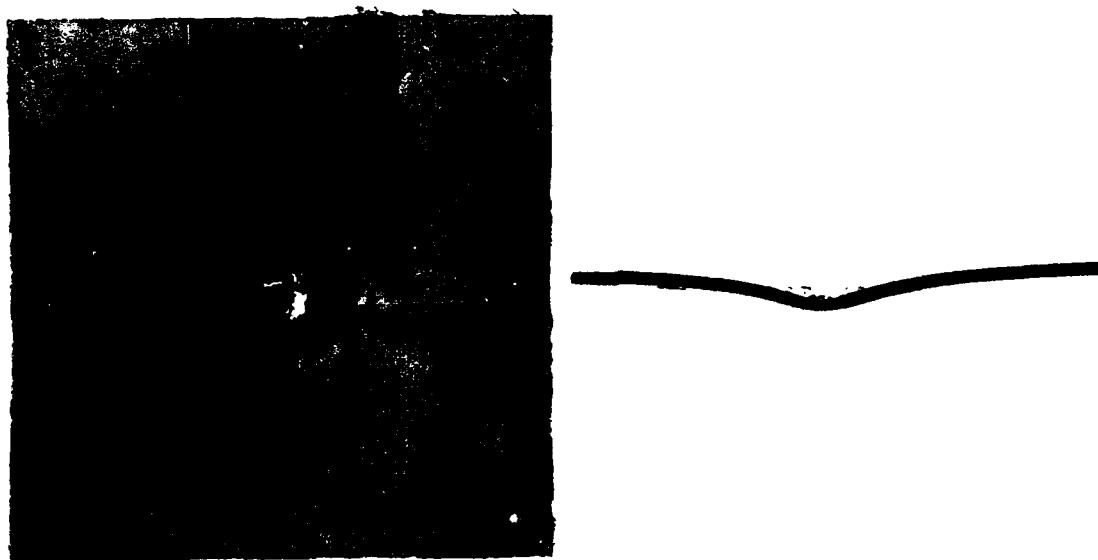


Figure 34 Front and side view (cut through) of a back-up plate recovered after a steel rod impact into 8.1 mm alumina backed by 4.0 mm aluminium at a velocity below the v_{50} (786 m/s)

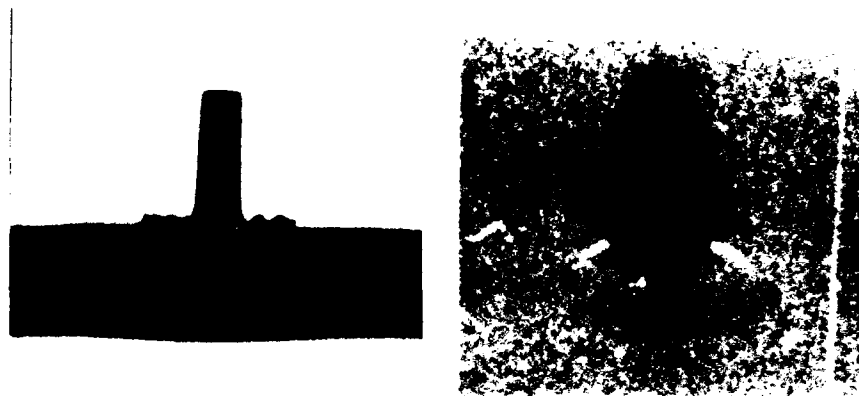


Figure 35 Normal and oblique flash radiograph at 25 μ s after impact of a steel rod impacting 8.1 mm alumina supported by 4.0 mm aluminium. Impact velocity is 576 m/s

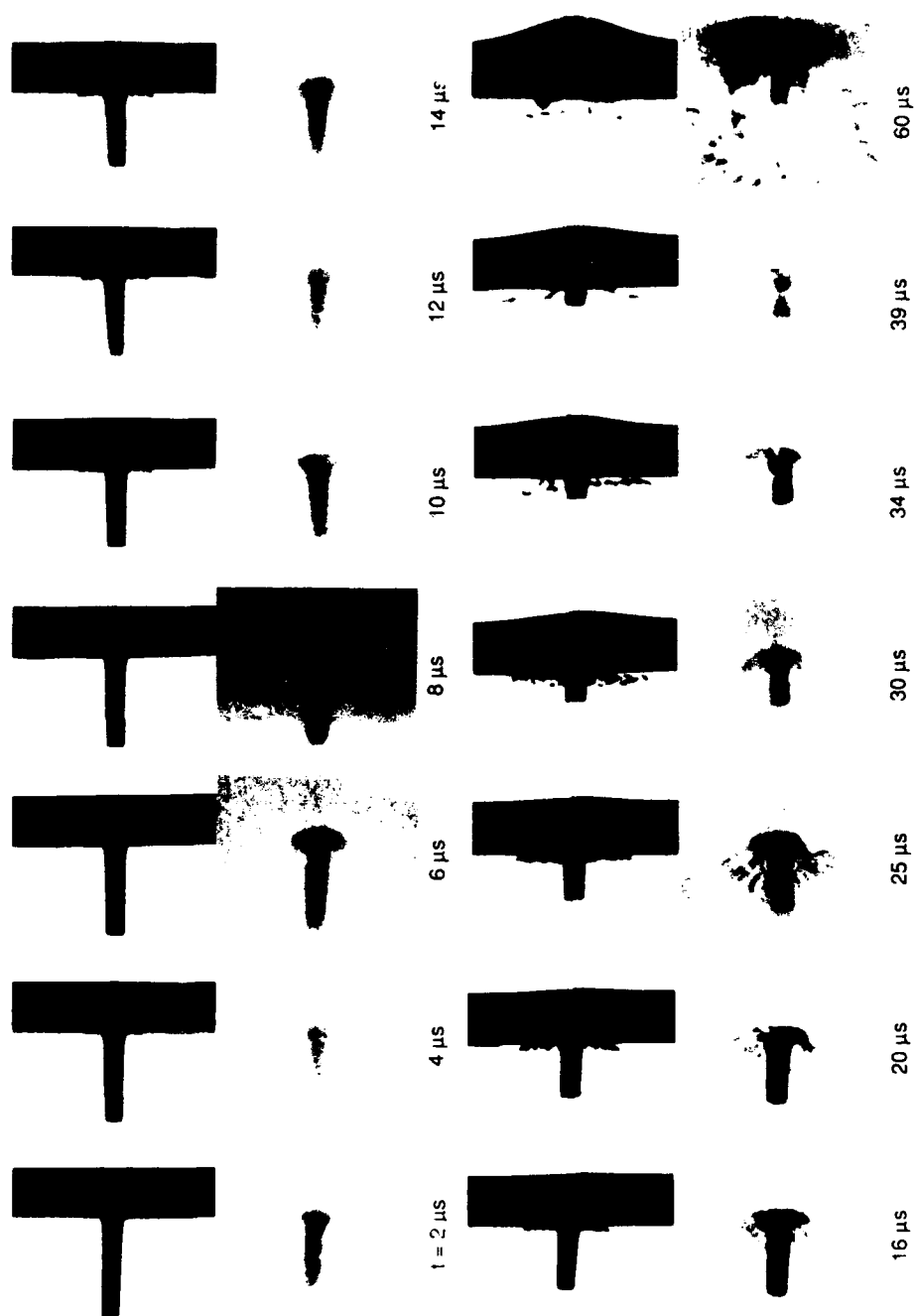


Figure 36 Sequence of normal and oblique (26°) flash radiograph cut-outs showing the projectile/armour interaction of a steel rod impacting 8.1 mm alumina and 4.0 mm aluminium at a velocity above the v_{50} (829 m/s)

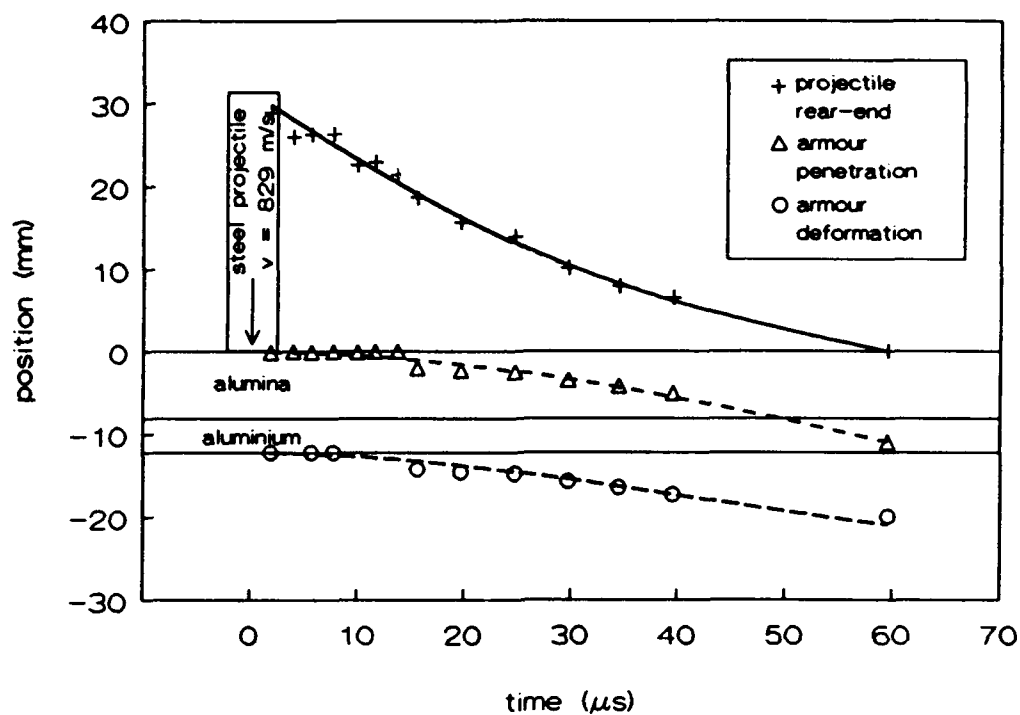


Figure 37 Position-versus-time curves of the steel rod impacting a target of 8.1 mm alumina backed by 4.0 mm aluminium at a velocity above the v_{50} (829 m/s)

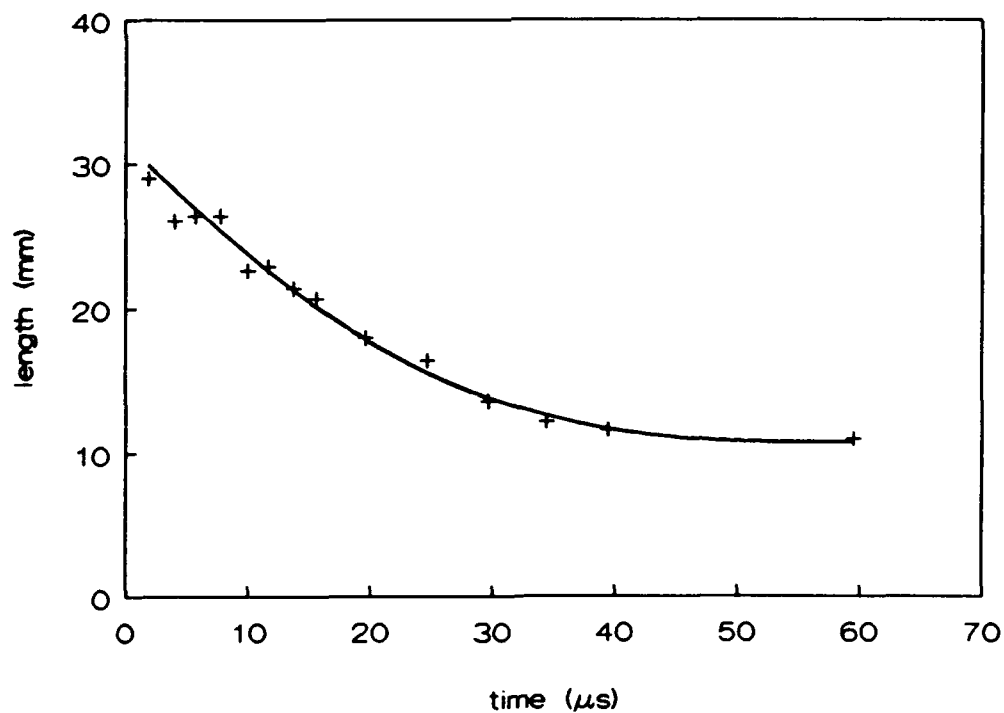


Figure 38 Projectile length versus time curve of the steel rod impacting a target of 8.1 mm alumina backed by 4.0 mm aluminium at a velocity above the v_{50} (829 m/s)

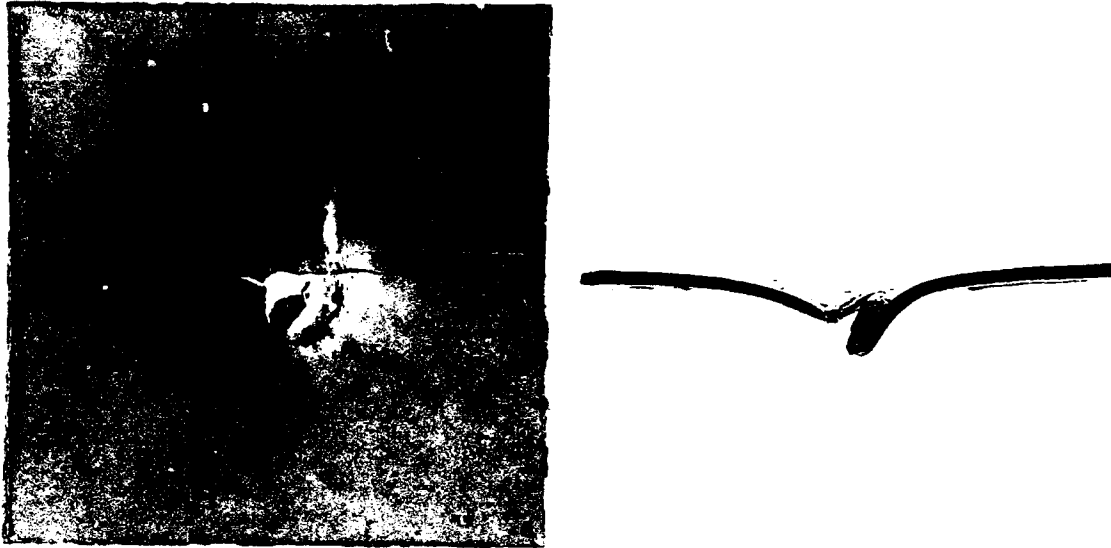


Figure 39 Front and side view (cut through) of a back-up plate recovered after a steel rod impact into 8.1 mm alumina backed by 4.0 mm aluminium at a velocity above the v_{50} (829 m/s)



Figure 40 Recovered steel rod after impact of a target of 8.1 mm alumina backed by 4.0 mm aluminium at a velocity above the v_{50} (829 m/s)

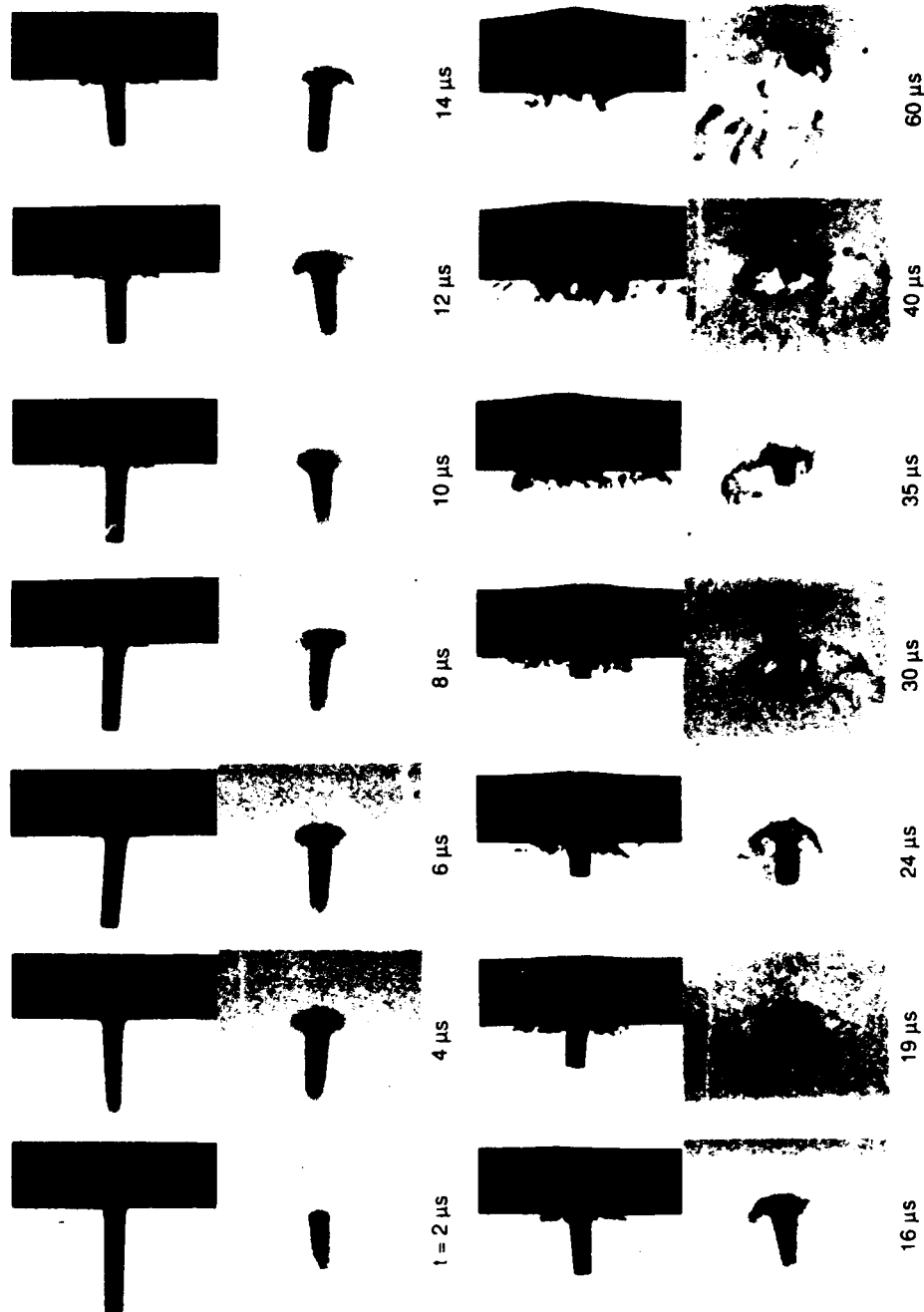


Figure 41 Sequence of normal and oblique (26°) flash radiograph cut-outs showing the projectile/armour interaction of a steel rod impacting 8.1 mm alumina and 8.0 mm aluminium at a velocity below the v_{50} (995 m/s)

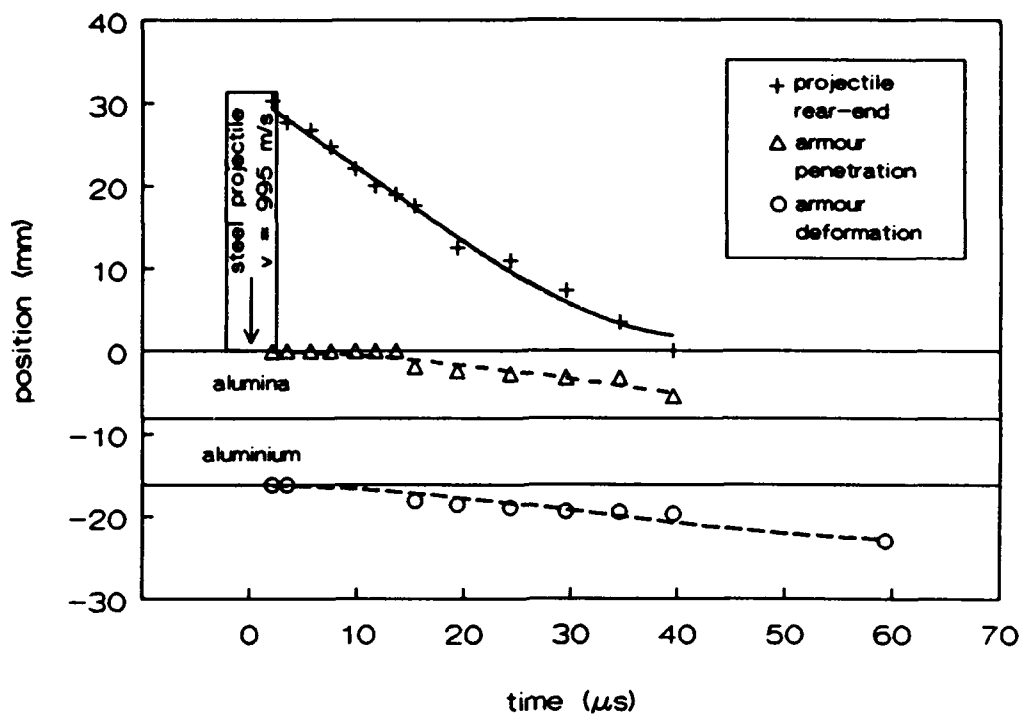


Figure 42 Position versus time curves of the steel rod impacting a target of 8.1 mm alumina backed by 8.0 mm aluminium at a velocity below the v_{50} (995 m/s)

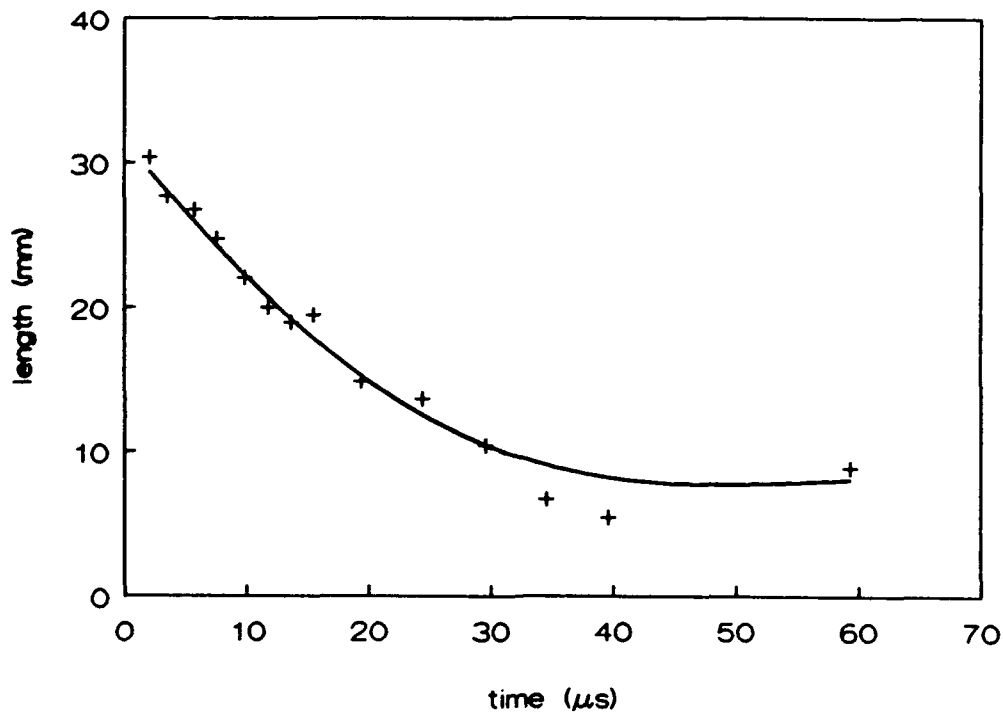


Figure 43 Projectile length versus time curve of the steel rod impacting a target of 8.1 mm alumina backed by 8.0 mm aluminium at a velocity below the v_{50} (995 m/s)



Figure 44 Recovered steel rod after impact of a target of 8.1 mm alumina backed by 8.0 mm aluminium at a velocity below the v_{50} (995 m/s)



Figure 45 Front and side view (cut through) of a back-up plate recovered after a steel rod impact into 8.1 mm alumina backed by 8.0 mm aluminium at a velocity below the v_{50} (995 m/s)

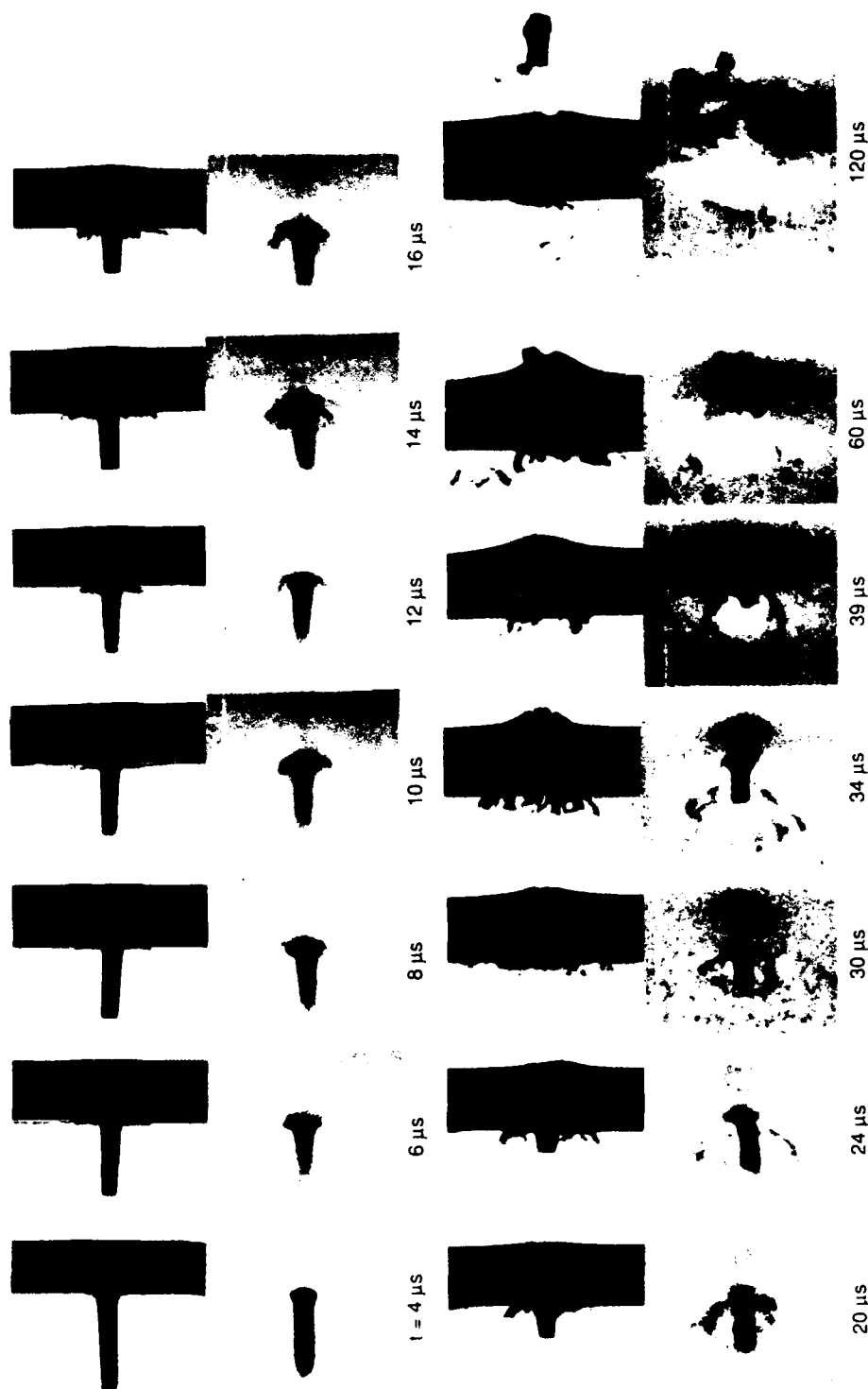


Figure 46 Sequence of normal and oblique (26°) flash radiograph cut-outs showing the projectile/armour interaction of a steel rod impacting 8.1 mm alumina and 8.0 mm aluminium at a velocity above the v_{50} (1091 m/s)

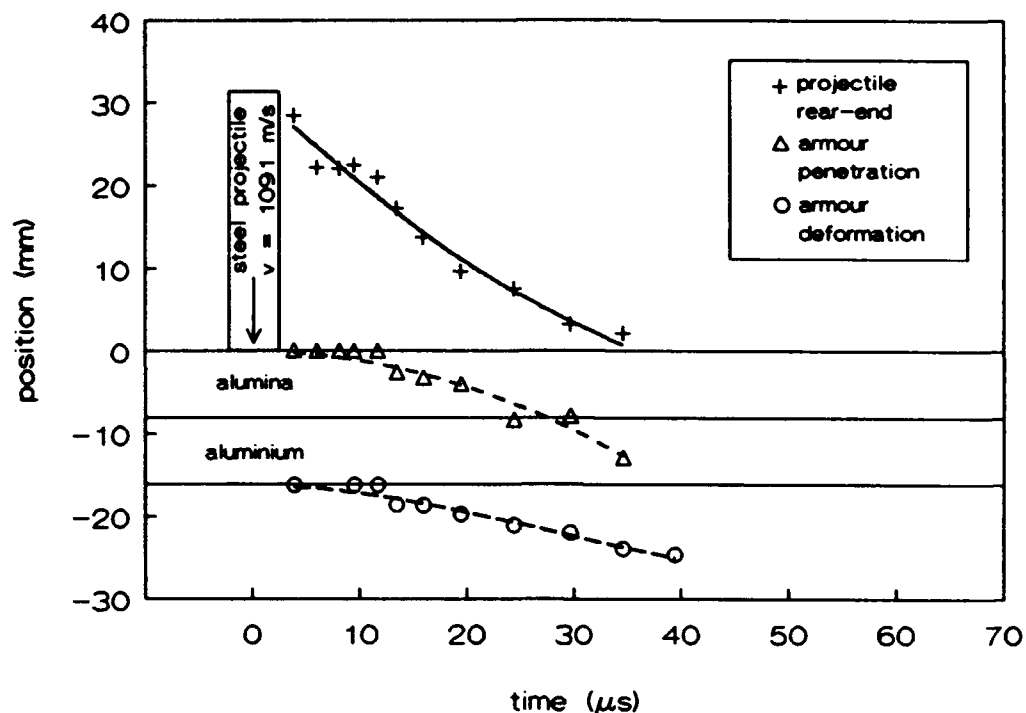


Figure 47 Position-versus-time curves of the steel rod impacting a target of 8.1 mm alumina backed by 8.0 mm aluminium at a velocity above the v_{50} (1091 m/s)

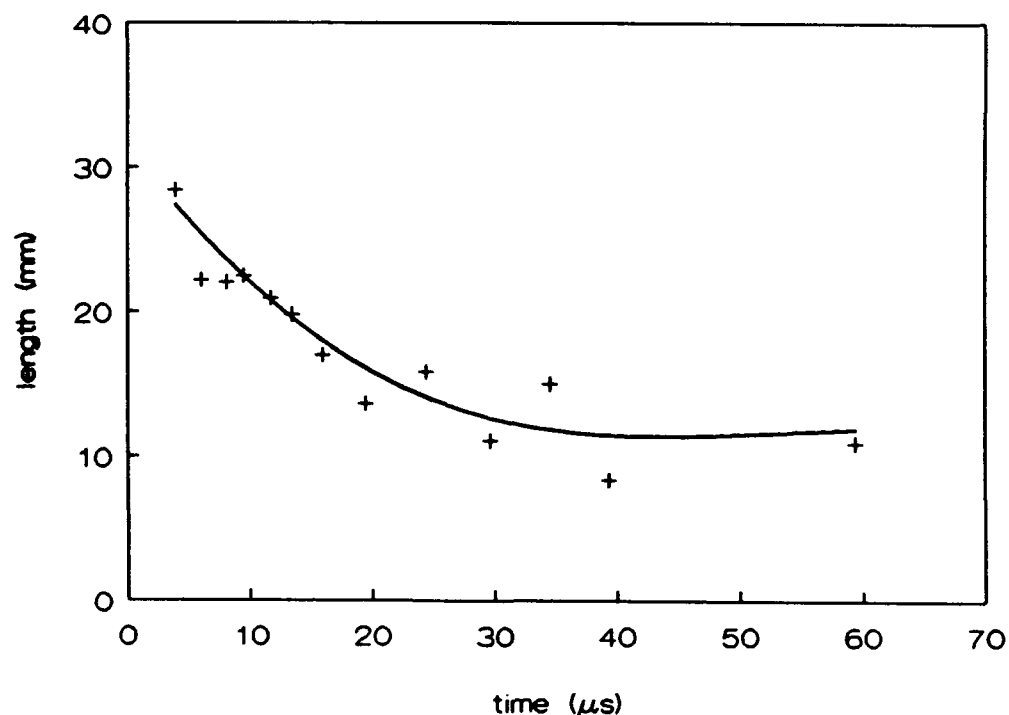


Figure 48 Projectile length-versus-time curve of the steel rod impacting a target of 8.1 mm alumina backed by 8.0 mm aluminium at a velocity above the v_{50} (1091 m/s)

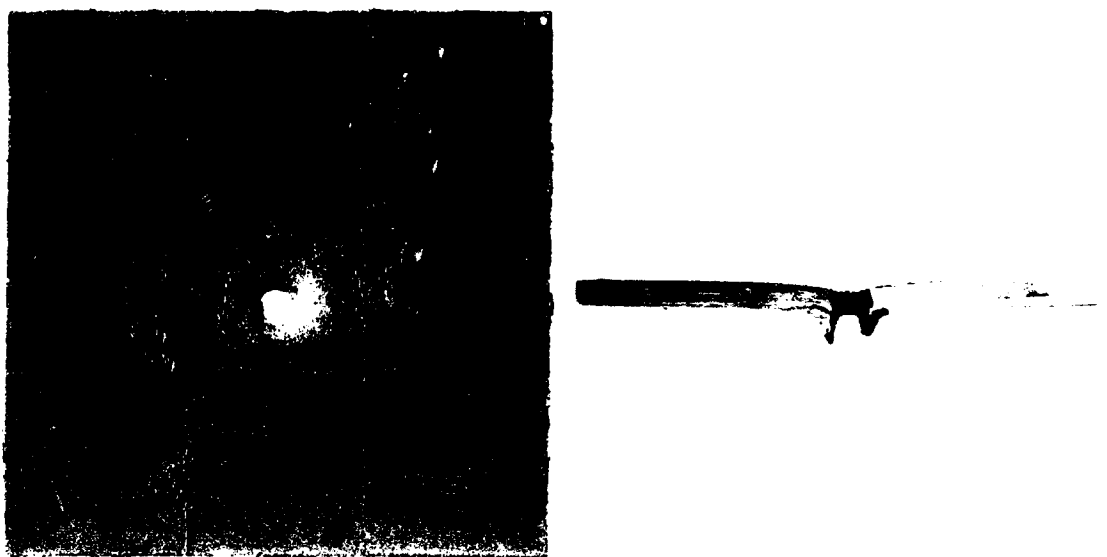


Figure 49 Front and side view (cut through) of a back-up plate recovered after a steel rod impact into 8.1 mm alumina backed by 8.0 mm aluminium at a velocity above the v_{50} (1091 m/s)



Figure 50 Recovered steel rod after impact of a target of 8.1 mm alumina backed by 8.0 mm aluminium at a velocity above the v_{50} (1091 m/s)

80080-51

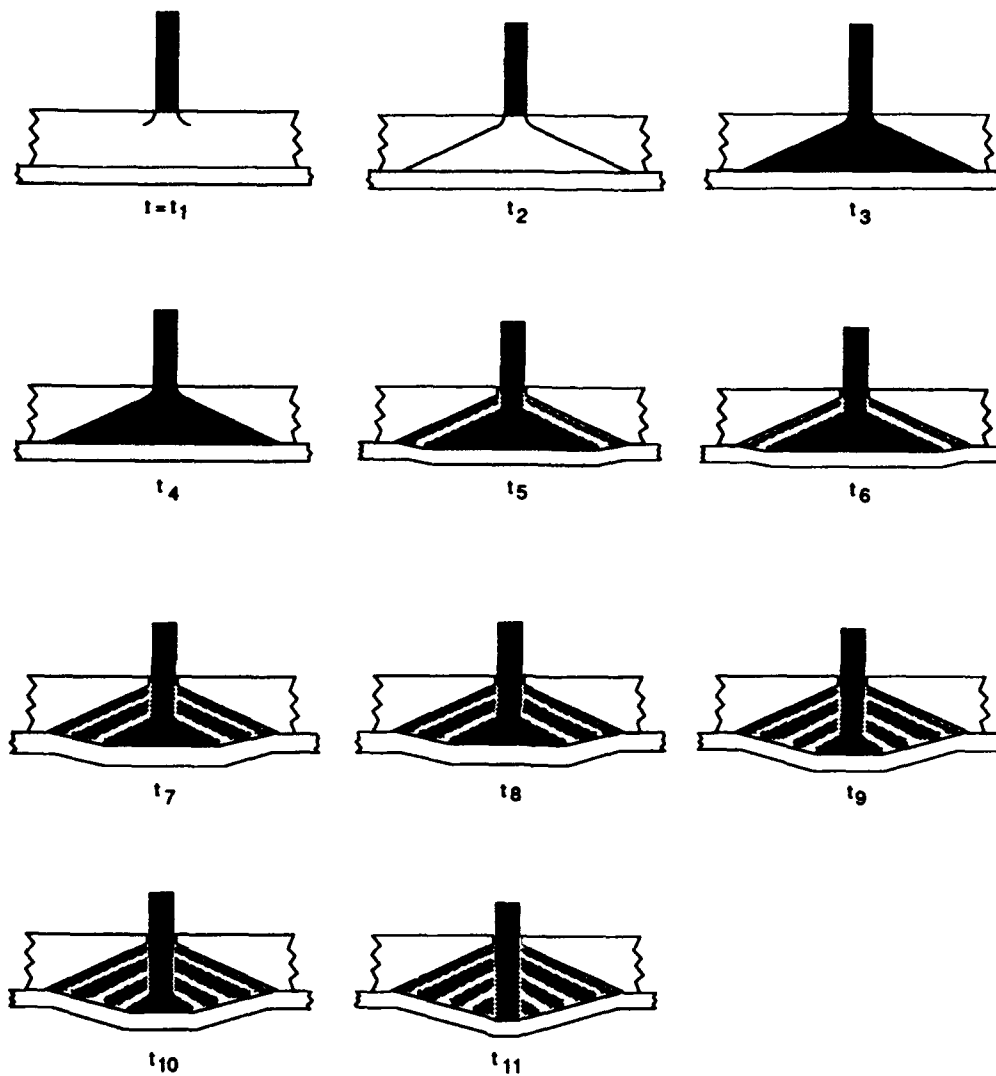


Figure 51 A phenomenological description of the ceramic fracturing process

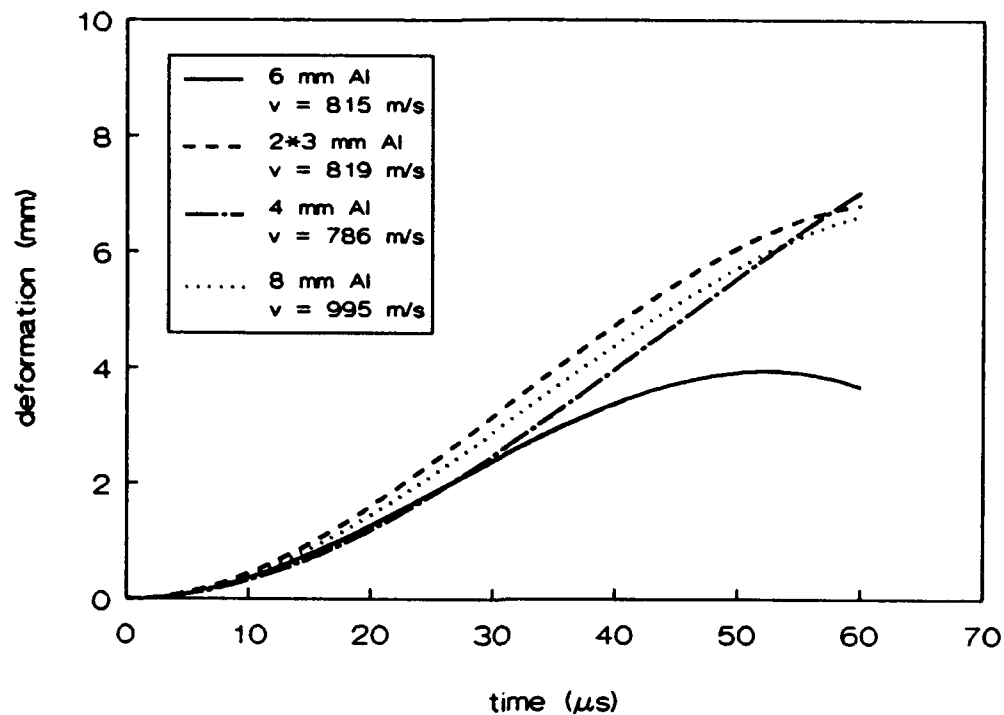


Figure 52 Comparison between the maximum back-up plate deformations of targets of 8.1 mm alumina backed by various aluminium back-up plates, when impacted below their ballistic limit velocities by steel rods

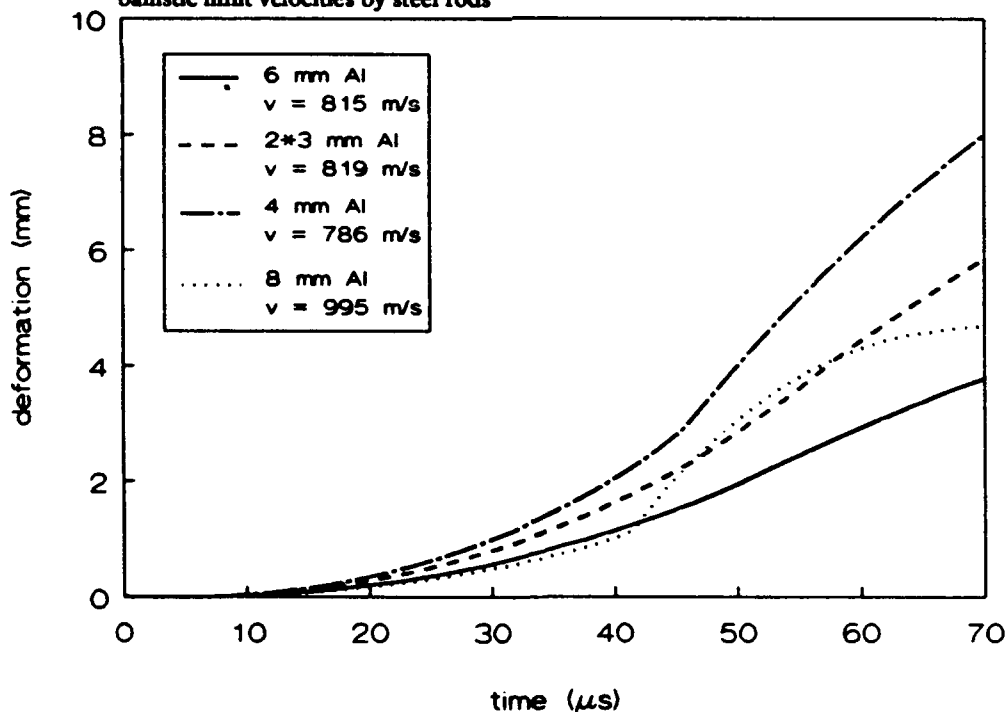


Figure 53 Comparison between the maximum back-up plate deformation velocities of targets of 8.1 mm alumina backed by various aluminium back-up plates, when impacted below their ballistic limit velocities by steel rods

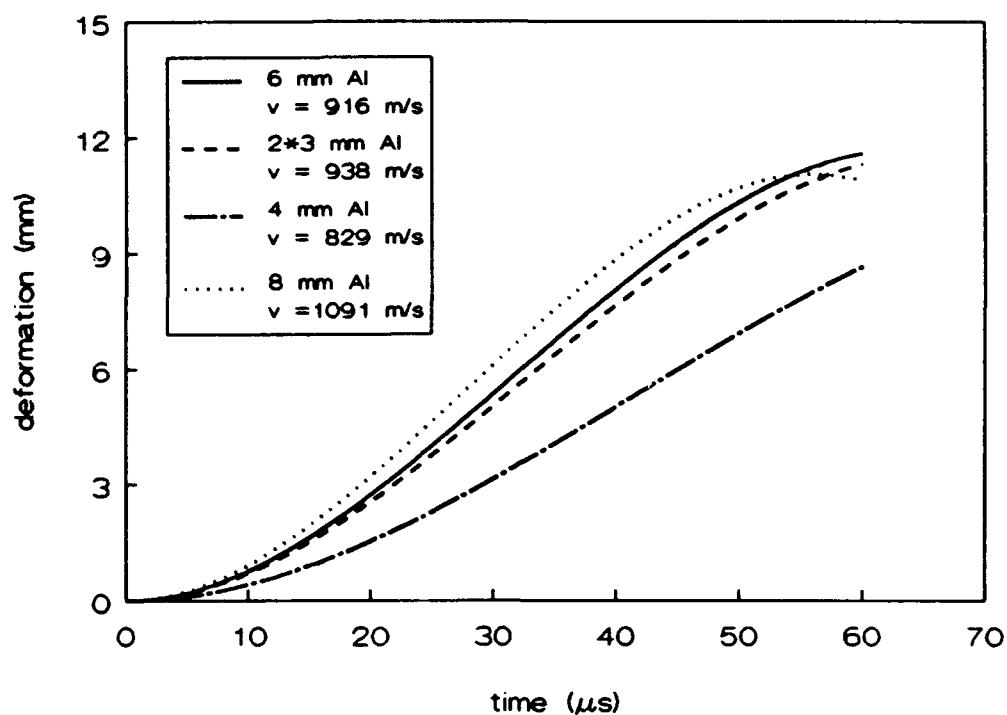


Figure 54 Comparison between the maximum back-up plate deformations of targets of 8.1 mm alumina backed by various aluminium back-up plates, when impacted above their ballistic limit velocities by steel rods

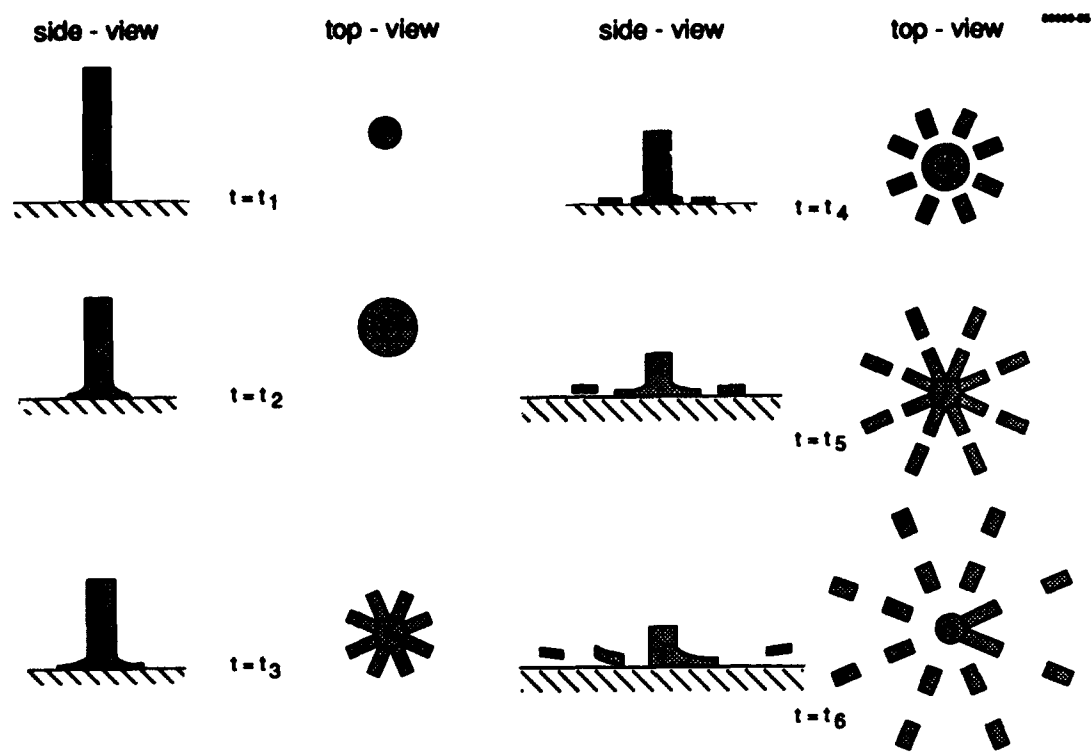


Figure 55 A schematic description of the observed projectile behaviour

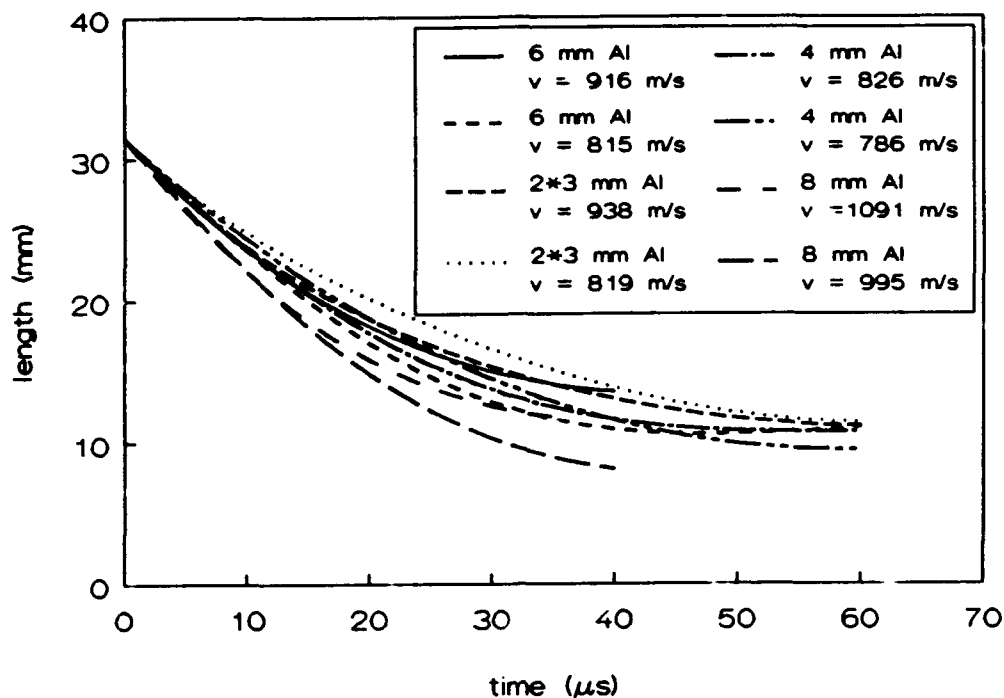


Figure 56 Comparison between the projectile lengths resulting impact at velocities below and above the ballistic limit velocities of targets of 8.1 mm alumina backed by various aluminium back-up plates

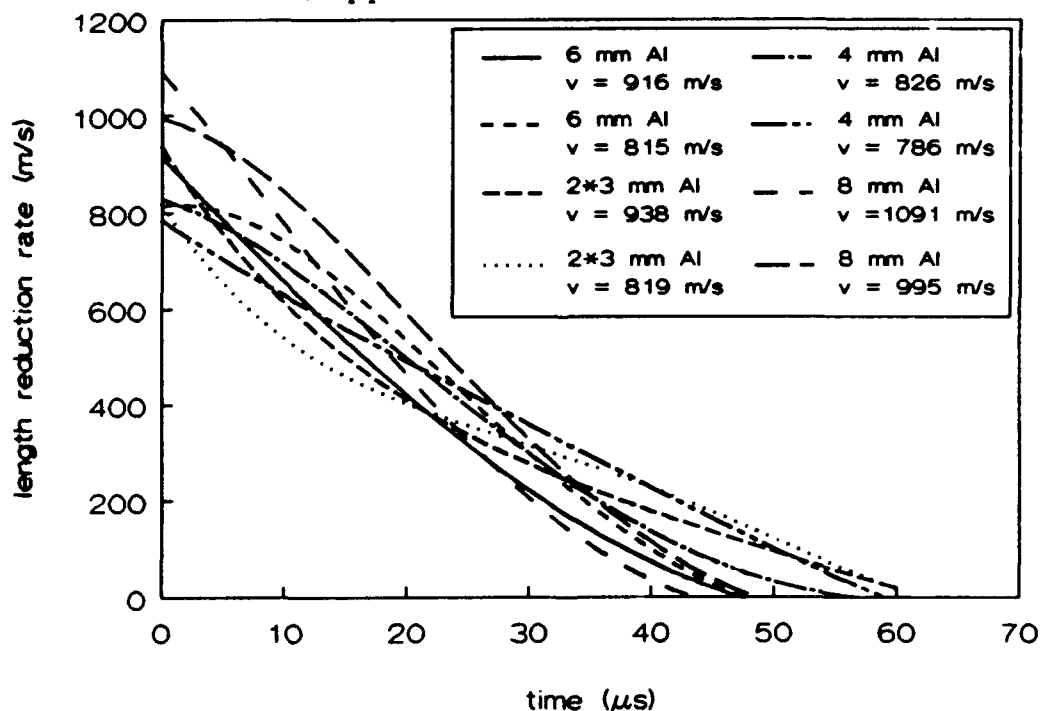


Figure 57 Comparison between the projectile length reduction rates resulting impact at velocities below and above the ballistic limit velocities of targets of 8.1 mm alumina backed by various aluminium back-up plates

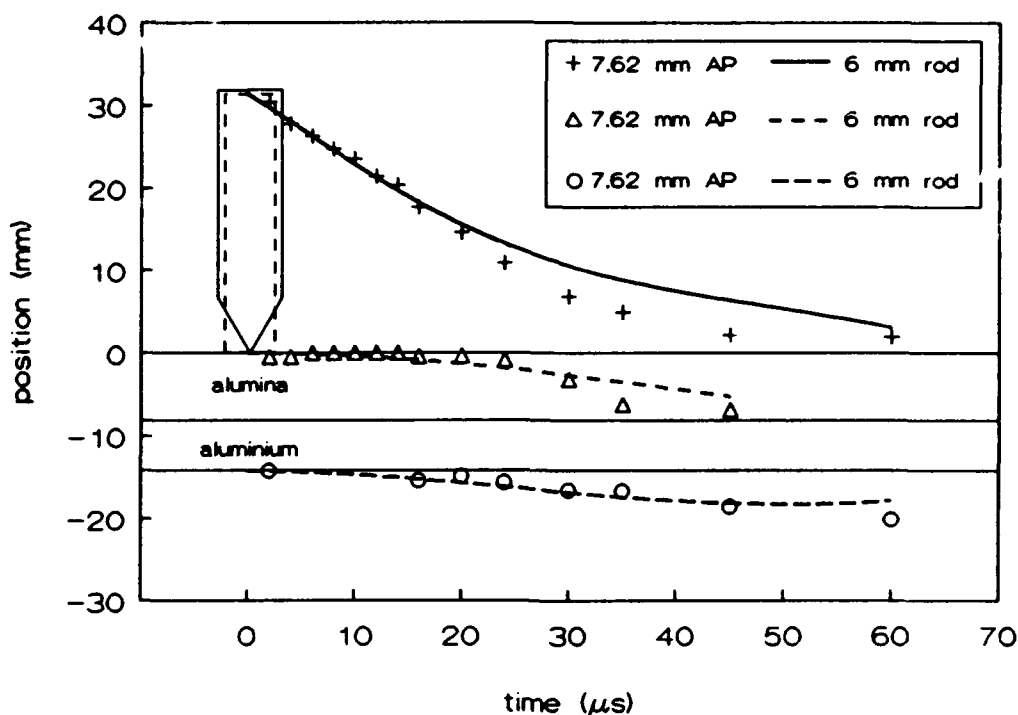


Figure 58 Comparison between the position-versus-time curves of the 7.62 mm AP projectile and the steel rod, for impact on to 8.1 mm alumina backed by 6.0 mm aluminium at a velocity of approximately 820 m/s

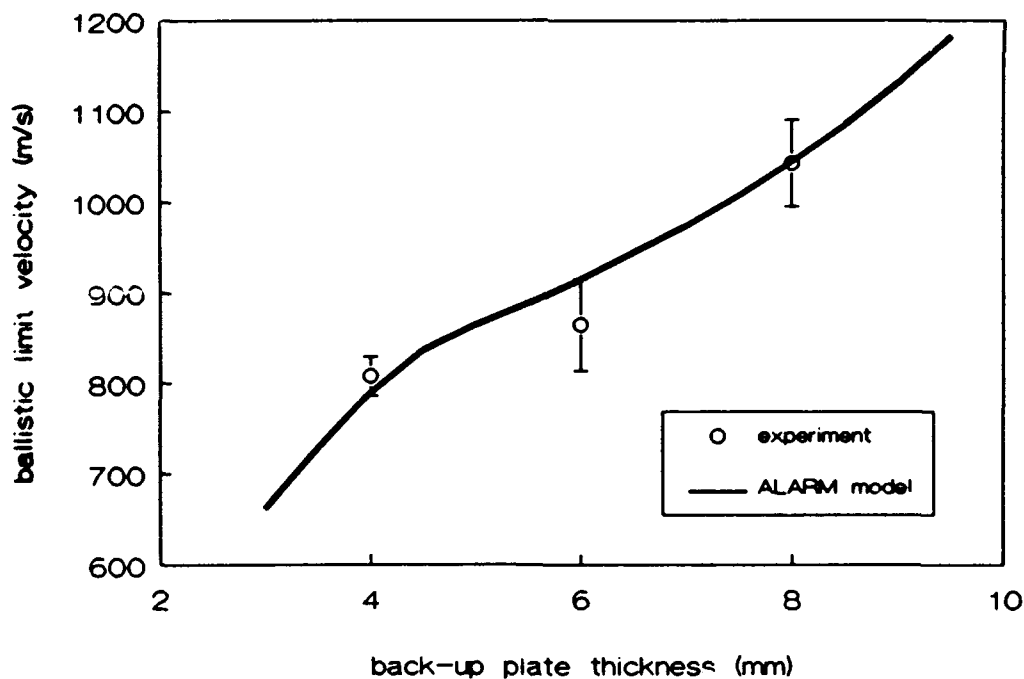


Figure 59 Comparison of ballistic limit velocities obtained by experiments and the ALARM model for targets of 8.1 mm alumina backed by various thicknesses of aluminium when impacted by the steel rod

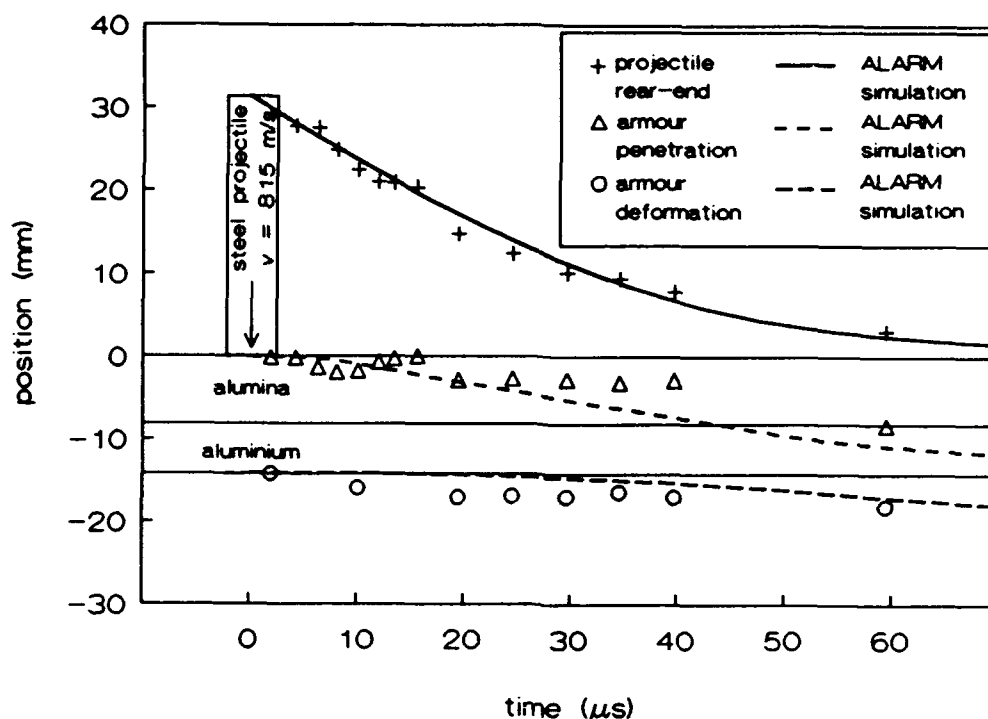


Figure 60a Comparison between predicted (ALARM) and experimentally obtained position-versus-time curves of the steel rod impacting 8.1 mm alumina backed by 6.0 mm aluminium at a velocity below the v_{50} (815 m/s)

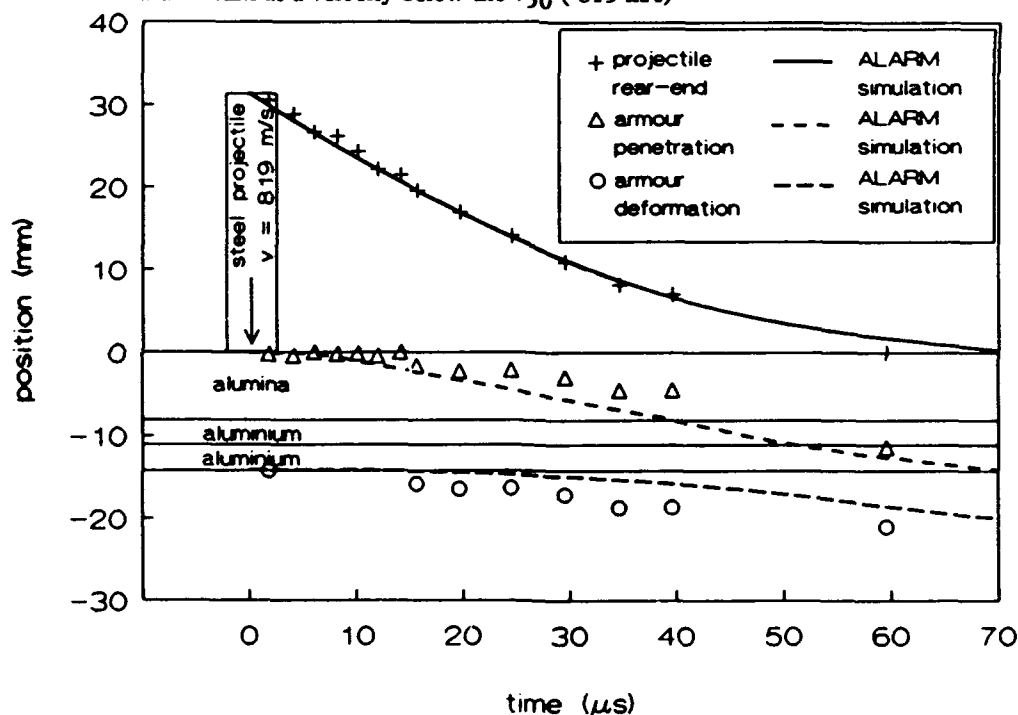


Figure 60b Comparison between predicted (ALARM) and experimentally obtained position-versus-time curves of the steel rod impacting 8.1 mm alumina backed by two 3.0 mm layers aluminium at a velocity below the v_{50} (819 m/s)

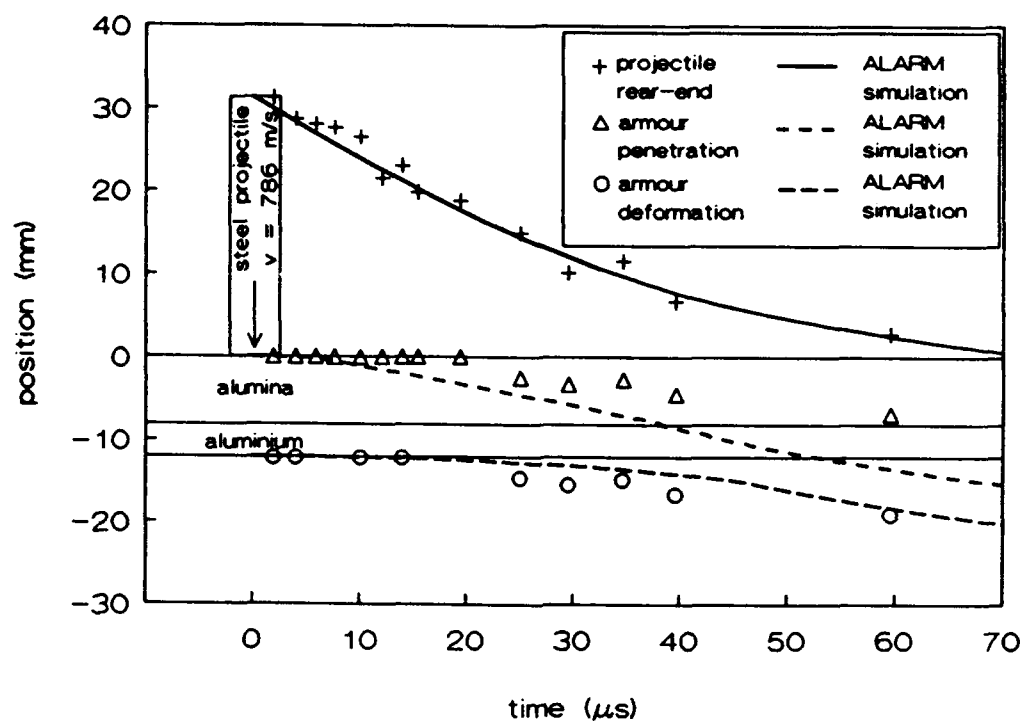


Figure 60c Comparison between predicted (ALARM) and experimentally obtained position-versus-time curves of the steel rod impacting 8.1 mm alumina backed by 4.0 mm aluminium at a velocity below the v_{50} (786 m/s)

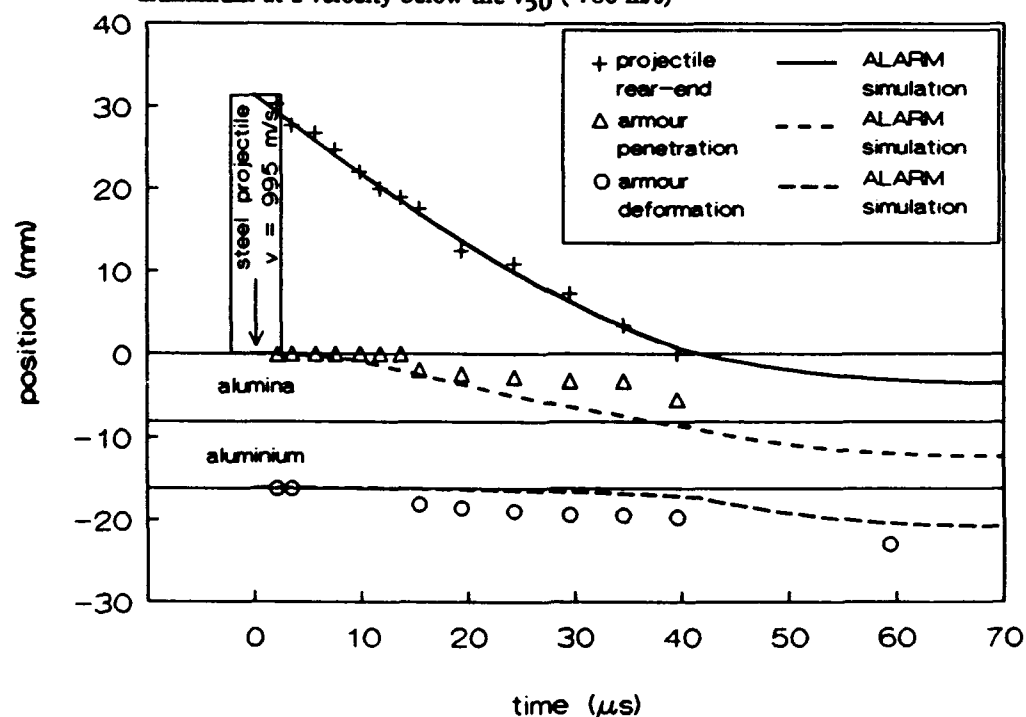


Figure 60d Comparison between predicted (ALARM) and experimentally obtained position-versus-time curves of the steel rod impacting 8.1 mm alumina backed by 8.0 mm aluminium at a velocity below the v_{50} (995 m/s)

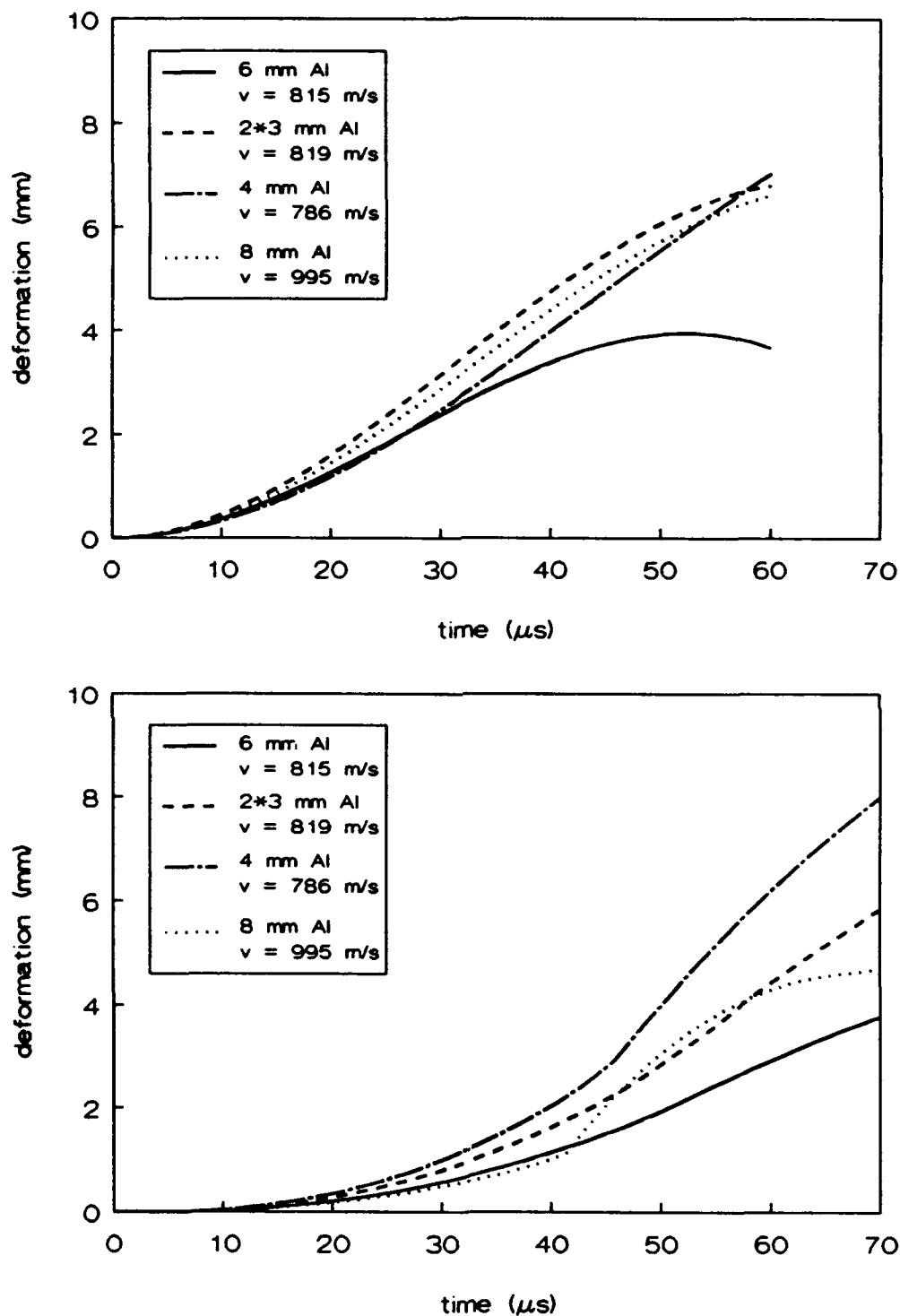


Figure 61 Comparison between predicted (ALARM) and experimentally obtained maximum back-up plate deformations of targets of 8.1 alumina backed by various aluminium back-up plates, when impacted below their ballistic limit velocities by steel rods

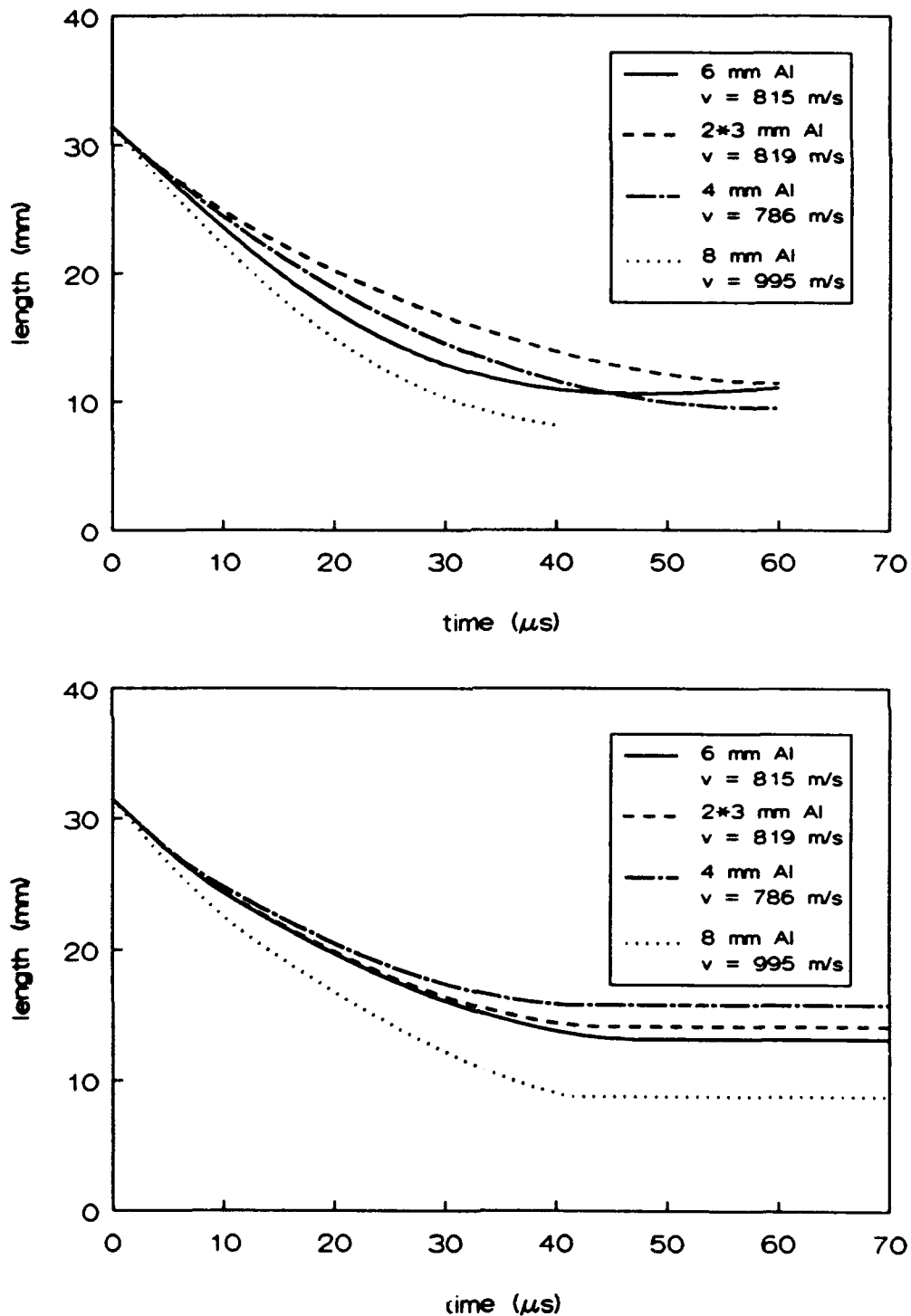


Figure 62 Comparison between predicted (ALARM) and experimentally obtained projectile lengths resulting impacts below the ballistic limit velocities of targets of 8.1 alumina backed by various aluminium back-up plates

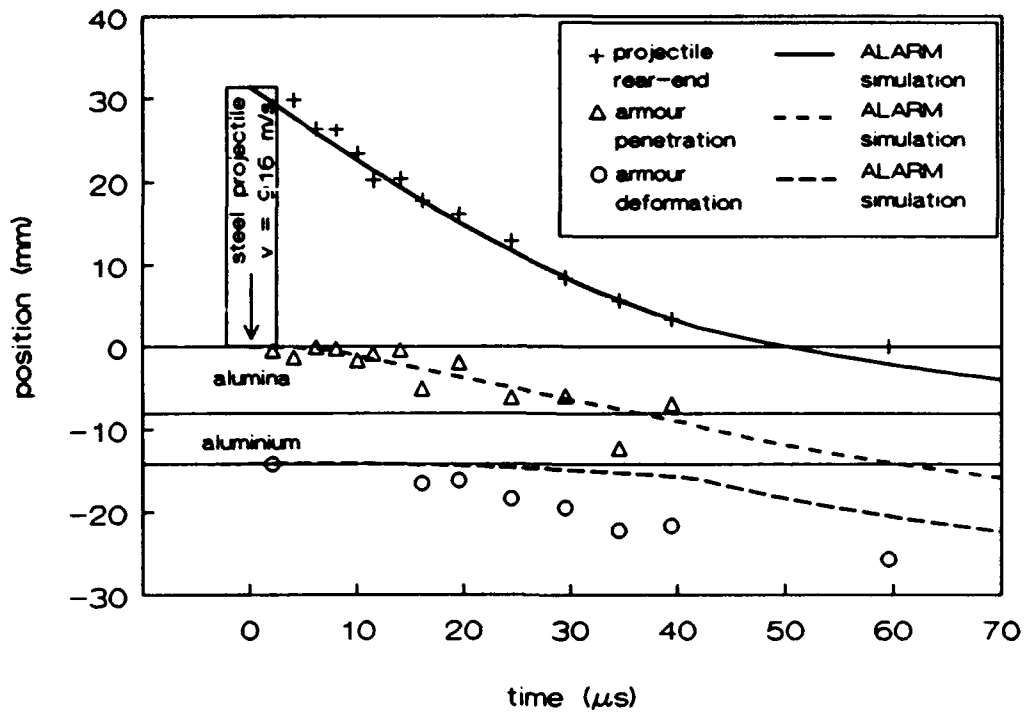


Figure 63a Comparison between predicted (ALARM) and experimentally obtained position-versus-time curves of the steel rod impacting 8.1 mm alumina backed by 6.0 mm aluminium at a velocity above the v_{50} (916 m/s)

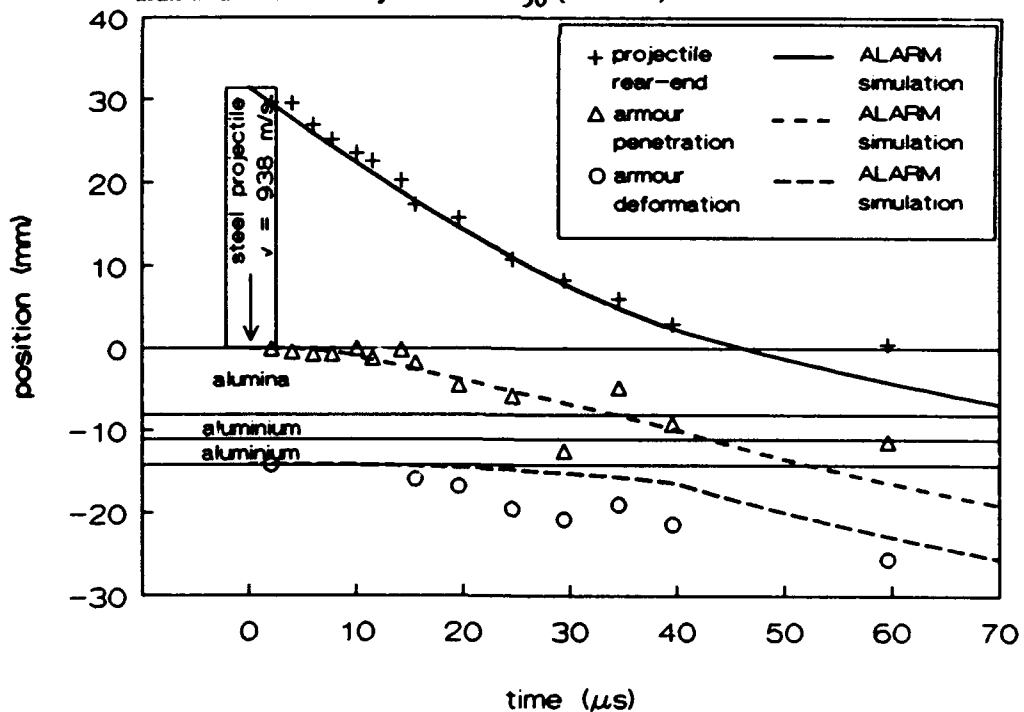


Figure 63b Comparison between predicted (ALARM) and experimentally obtained position-versus-time curves of the steel rod impacting 8.1 mm alumina backed by two 3.0 mm layers aluminium at a velocity above the v_{50} (938 m/s)

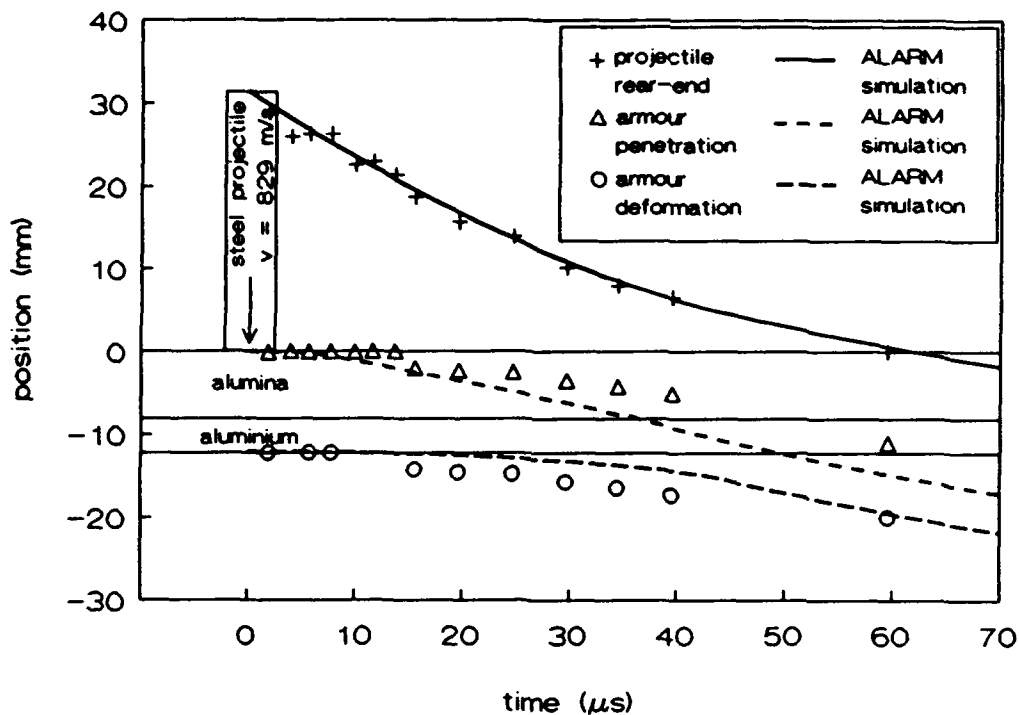


Figure 63c Comparison between predicted (ALARM) and experimentally obtained position-versus-time curves of the steel rod impacting 8.1 mm alumina backed by 4.0 mm aluminium at a velocity above the v_{50} (826 m/s)

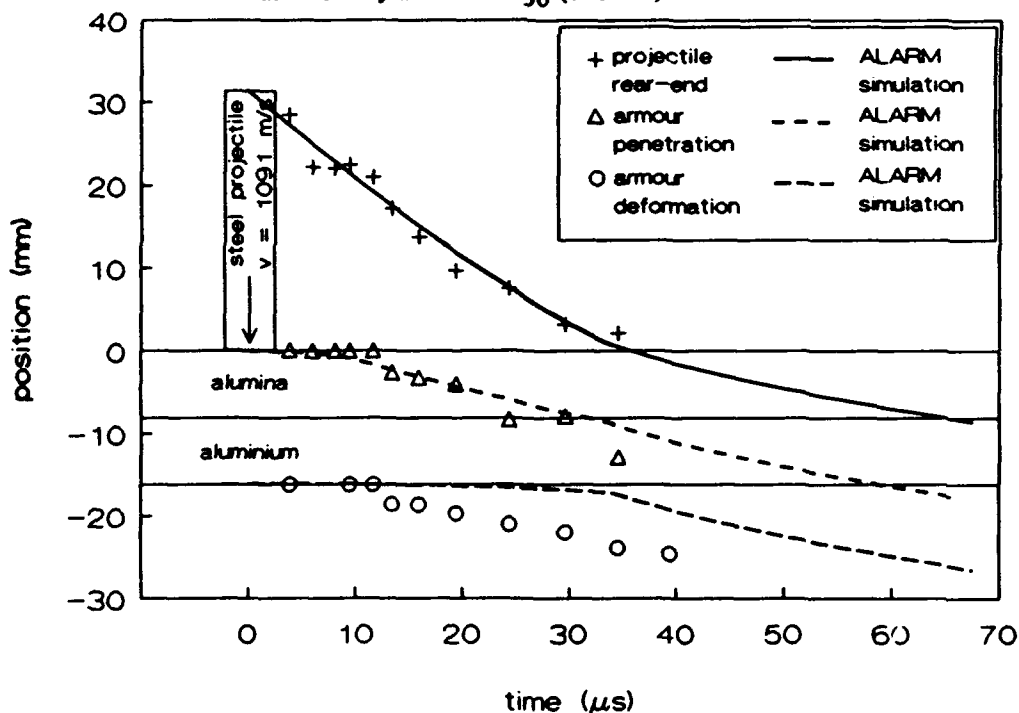


Figure 63d Comparison between predicted (ALARM) and experimentally obtained position-versus-time curves of the steel rod impacting 8.1 mm alumina backed by 8.0 mm aluminium at a velocity above the v_{50} (1091 m/s)

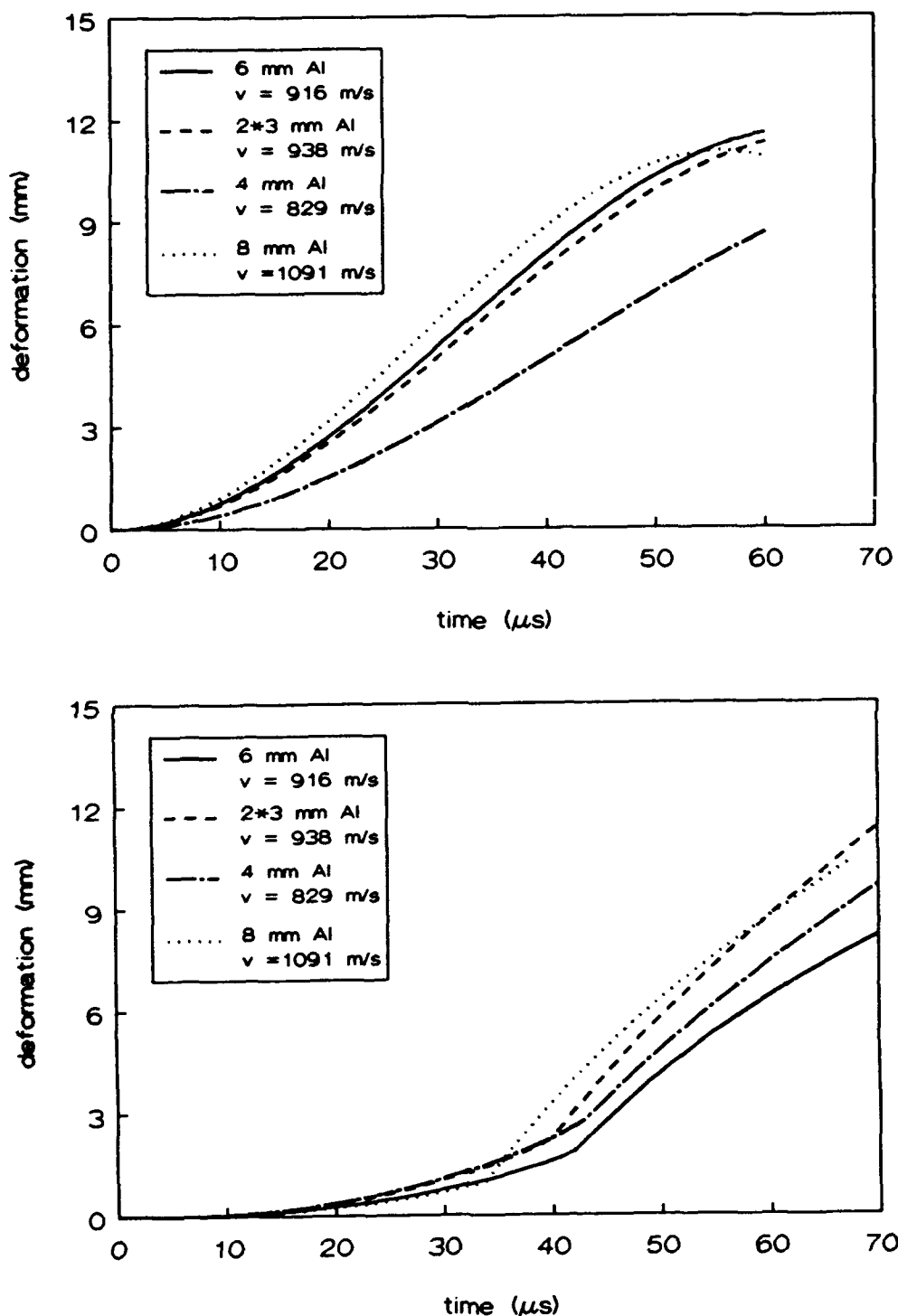


Figure 64

Comparison between predicted (ALARM) and experimentally obtained maximum back-up plate deformations of targets of 8.1 alumina backed by various aluminium back-up plates, when impacted above their ballistic limit velocities by steel rods

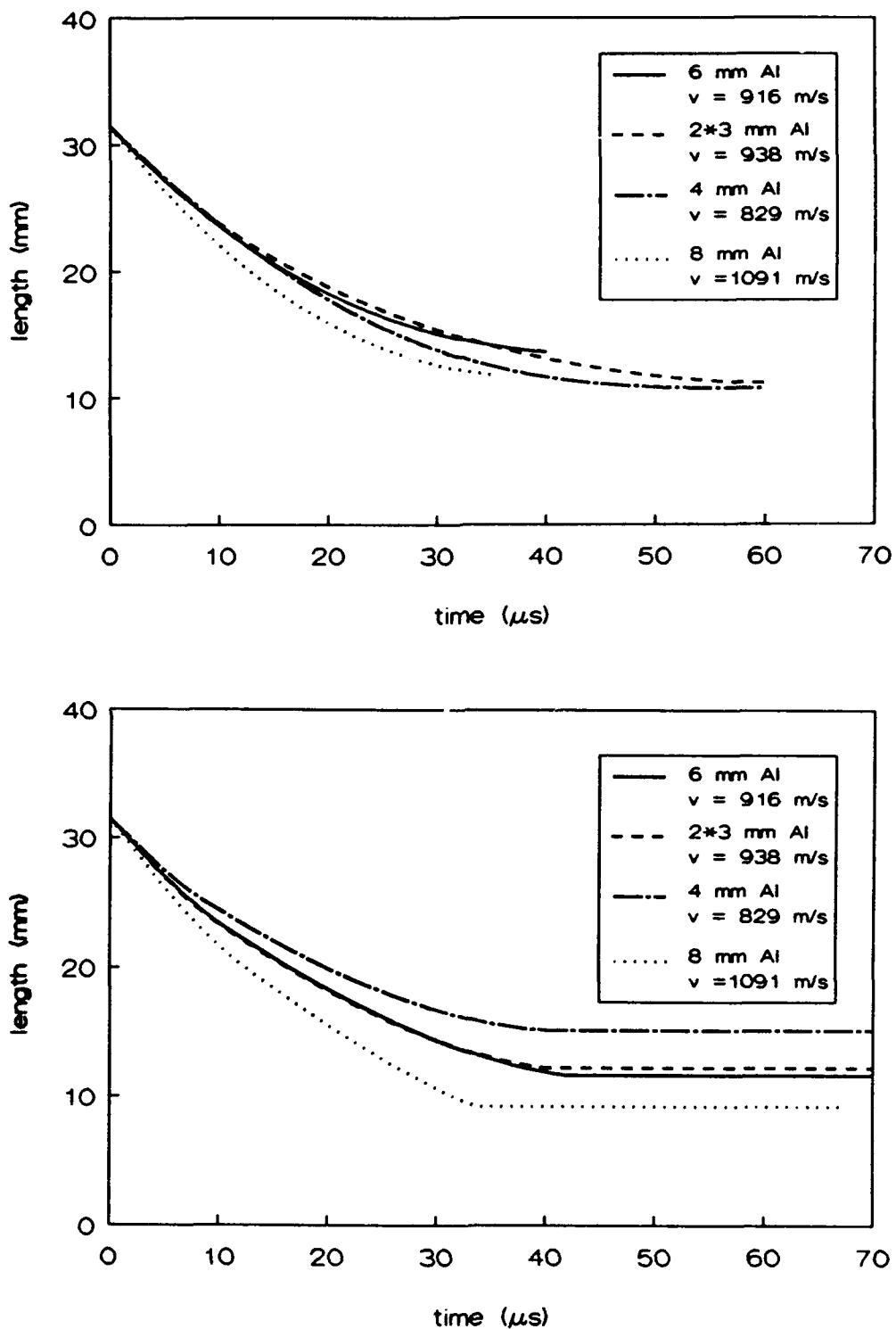


Figure 65 Comparison between predicted (ALARM) and experimentally obtained projectile length reductions resulting impacts above the ballistic limit velocities of targets of 8.1 alumina backed by various aluminium back-up plates

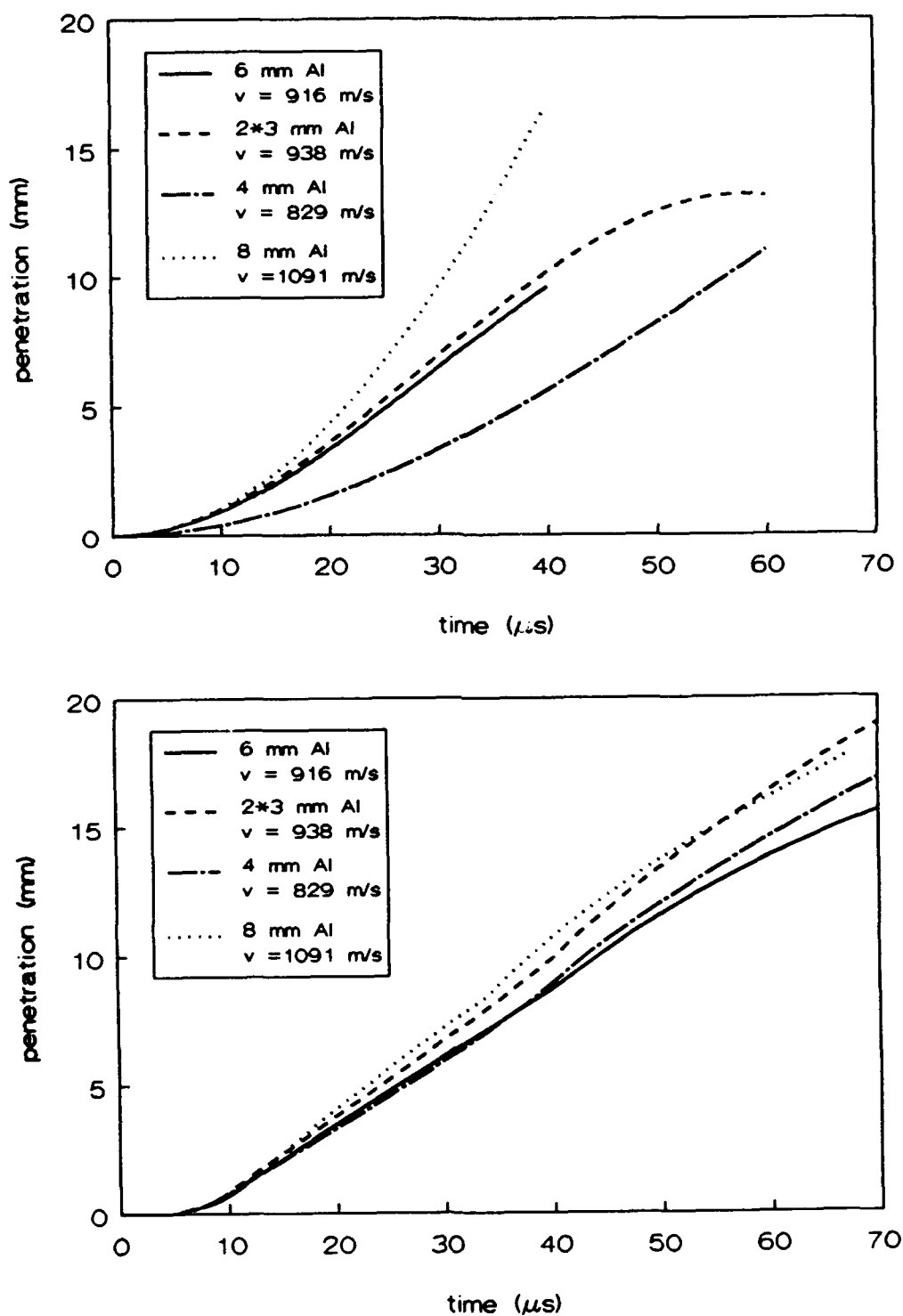


Figure 66 Comparison between predicted (ALARM) and experimentally obtained armour penetration of targets of 8.1 alumina backed by various aluminium back-up plates, when impacted above their ballistic limit velocities by steel rods

ANNEX A MATERIAL PROPERTIES OF ETG-100, HILOX-973 AND AL6061-T6

Table A.1 Properties of ETG-100 steel

density	[kg/m ³]	7800
ultimate yield strength	[N/m ²]	1.030*10 ⁹
ultimate shear strength	[N/m ²]	0.590*10 ⁹
H _{TC}		28
failure strain		0.07

Table A.2 Material properties of Morgan Matroc Hilox 973 alumina

density	[kg/m ³]	3810.0
H _V	[kg/mm ²]	121.±67
Young's modulus	GPa	378±15
longitudinal sonic		
velocity	[mm/μs]	10.82±0.22
grain size	[μm]	1-20

Table A.3 Properties of aluminium 6061-T6

density	[kg/m ³]	2705.0
ultimate yield strength	[N/m ²]	0.310*10 ⁹
ultimate shear strength	[N/m ²]	0.200*10 ⁹
failure strain		0.13

ANNEX B THE EXPERIMENT DATA AND CONSTANTS OF POLYNOMIALS

Table B.1 Results of the analysis of the flash radiographs of steel rods impacting 8.1 mm alumina supported by 6.0 mm aluminium at 815 m/s

time [μs]	proj [mm] ±0.5	pen [mm] ±1.0	wtot [mm] ±0.5	l [mm] ±1.0	shatter [mm] ±0.5
2.0	29.1	0.1	0.0	29.2	6.0
4.3	27.7	0.2	0.0	27.9	7.0
6.4	27.5	1.3	-	28.8	7.0
8.1	24.8	1.9	-	26.7	8.8
10.1	22.4	1.7	1.7	24.2	9.7
12.0	21.0	0.7	-	21.7	11.1
13.5	20.9	0.3	-	21.1	12.0
15.7	20.3	0.0	-	20.3	9.7
19.5	14.8	2.8	2.8	17.6	15.2
24.6	12.4	2.7	2.7	15.1	18.0
29.7	10.1	2.8	2.7	12.9	21.2
34.6	9.4	3.1	2.2	12.5	21.2
39.7	7.9	2.8	2.8	10.7	23.9
59.5	3.1	8.2	3.9	11.4	33.6

Table B.2 Results of the analysis of the flash radiographs of steel rods impacting 8.1 mm alumina supported by 6.0 mm aluminium at 916 m/s

time [μs]	proj [mm] ±0.5	pen [mm] ±1.0	wtot [mm] ±0.5	l [mm] ±1.0	shatter [mm] ±10.5
2.1	29.0	0.5	0.0	29.5	6.0
4.1	29.8	1.3	-	31.1	4.6
6.2	26.4	0.1	-	26.4	7.9
8.1	26.3	0.3	-	26.6	8.4
10.1	23.4	1.6	-	25.1	8.8
11.5	20.2	0.9	-	21.1	12.9
14.1	20.3	0.4	-	20.7	11.1
16.1	17.7	5.1	2.3	22.8	13.9
19.6	16.1	2.0	2.0	18.0	15.7
24.5	12.9	6.2	4.2	19.1	11.5
29.5	8.3	6.0	5.2	14.4	22.1
34.5	5.6	12.3	8.0	17.9	28.6
39.4	3.3	7.0	7.4	10.3	28.1
59.6	0.0	-	11.5	-	45.1

Table B.3 Results of the analysis of the flash radiographs of steel rods impacting 8.1 mm alumina supported by two 3.0 mm layers of aluminium at 819 m/s

time [μs]	proj [mm] ±0.5	pen [mm] ±1.0	wtot [mm] ±0.5	l [mm] ±1.0	shatter [mm] ±0.5
1.8	30.6	0.2	0.0	30.8	3.7
4.1	28.9	0.4	-	29.3	4.6
6.1	26.7	0.0	-	26.7	7.9
8.2	26.2	0.2	-	26.4	8.4
10.1	24.3	0.1	-	24.5	8.8
12.0	22.2	0.4	-	22.6	10.7
14.1	21.5	0.0	-	21.5	10.7
15.7	19.6	1.6	1.6	21.2	12.4
19.7	17.0	2.2	2.2	19.2	14.3
24.5	14.1	2.1	2.1	16.2	16.1
29.6	10.9	2.9	2.9	13.8	19.3
34.0	8.2	4.5	4.5	12.7	21.6
39.6	7.0	4.4	4.4	11.5	24.4
59.6	0.0	11.4	6.8	11.4	23.5

Table B.4 Results of the analysis of the flash radiographs of steel rods impacting 8.1 mm alumina supported by two 3.0 mm layers of aluminium at 938 m/s

time [μs]	proj [mm] ±0.5	pen [mm] ±1.0	wtot [mm] ±0.5	l [mm] ±1.0	shatter [mm] ±0.5
2.1	29.6	0.1	0.0	29.7	6.0
4.0	29.5	0.4	-	29.9	5.6
6.0	27.0	0.7	-	27.6	7.4
7.8	25.2	0.7	-	25.9	8.8
10.1	23.6	0.0	-	23.5	10.2
11.6	22.6	1.1	-	23.7	11.5
14.2	20.3	0.2	-	20.4	12.5
15.6	17.4	1.7	1.7	19.1	15.2
19.6	15.8	4.5	2.6	20.2	16.6
24.6	10.8	5.8	5.3	16.6	19.8
29.5	8.3	12.5	6.6	20.8	23.0
34.6	6.0	4.8	4.8	10.8	24.4
39.6	3.0	9.2	7.2	12.2	29.0
59.6	0.5	11.4	11.4	11.9	41.9

Table B.5 Results of the analysis of the flash radiographs of steel rods impacting 8.1 mm alumina supported by 4.0 mm aluminium at 786 m/s

time [μs]	proj [mm] ±0.5	pen [mm] ±1.0	wtot [mm] ±0.5	l [mm] ±1.0	shatter [mm] ±0.5
1.9	31.3	0.0	0.0	31.3	3.6
4.0	28.7	0.0	0.0	28.7	6.3
5.9	28.0	0.0	-	28.0	6.8
7.7	27.7	0.0	-	27.7	7.2
10.1	26.5	0.0	0.0	26.5	7.7
12.1	21.5	0.0	-	21.5	10.9
14.0	23.0	0.0	0.0	23.0	10.0
15.5	19.8	0.0	-	19.8	12.7
19.4	18.8	0.0	-	18.8	12.7
25.0	14.9	2.4	2.4	17.4	15.4
29.5	10.2	3.3	3.3	13.4	21.7
34.6	11.6	2.7	2.7	14.2	20.8
39.6	6.7	4.4	4.4	11.2	23.5
59.6	2.8	6.9	6.9	9.7	29.8

Table B.6 Results of the analysis of the flash radiographs of steel rods impacting 8.1 mm alumina supported by 4.0 mm aluminium at 829 m/s

time [μs]	proj [mm] ±0.5	pen [mm] ±1.0	wtot [mm] ±0.5	l [mm] ±1.0	shatter [mm] ±0.5
1.9	28.9	0.1	0.0	29.0	4.5
4.0	26.0	0.0	-	26.0	7.7
5.7	26.3	0.0	0.0	26.4	7.7
7.8	26.4	0.0	0.0	26.4	7.7
10.0	22.6	0.0	-	22.6	10.0
11.7	22.9	0.0	-	22.9	10.0
13.8	21.4	0.0	-	21.4	10.9
15.6	18.7	2.0	2.0	20.7	12.7
19.7	15.7	2.3	2.3	18.0	14.5
24.7	13.9	2.5	2.5	16.5	16.3
29.7	10.1	3.5	3.5	13.6	20.3
34.5	8.0	4.2	4.2	12.2	24.0
39.5	6.6	5.1	5.1	11.6	24.4
59.6	0.0	11.0	7.7	11.0	36.2

Table B.7 Results of the analysis of the flash radiographs of steel rods impacting 8.1 mm alumina supported by 2.0 mm aluminium at 995 m/s

time [μs]	proj [mm] ±0.5	pen [mm] ±1.0	wtot [mm] ±0.5	l [mm] ±1.0	shatter [mm] ±0.5
2.1	30.3	0.0	0.0	30.3	3.6
3.5	27.7	0.0	0.0	27.7	7.2
5.7	26.8	0.0	-	26.8	7.7
7.6	24.7	0.0	-	24.7	9.0
9.9	22.1	0.0	-	22.1	11.3
11.8	20.0	0.0	-	20.0	11.8
13.7	18.9	0.0	-	18.9	14.5
15.5	17.6	1.9	1.9	19.5	15.4
19.4	12.5	2.4	2.4	14.9	19.0
24.4	10.9	2.7	2.7	13.7	21.7
29.6	7.2	3.2	3.2	10.4	26.2
34.6	3.4	3.3	3.3	6.7	30.7
39.6	0.0	5.4	3.5	5.4	33.5
59.4	-	-	6.8	8.9	47.5

Table B.8 Results of the analysis of the flash radiographs of steel rods impacting 8.1 mm alumina supported by 8.0 mm aluminium at 1091 m/s

time [μs]	proj [mm] ±0.5	pen [mm] ±1.0	wtot [mm] ±0.5	l [mm] ±1.0	shatter [mm] ±0.5
3.9	28.5	0.1	0.0	28.4	5.4
6.1	22.2	0.0	-	22.2	11.3
8.1	22.0	0.0	-	22.0	10.9
9.5	22.4	0.0	0.0	22.5	12.7
11.7	21.0	0.0	0.0	20.9	14.5
13.5	17.2	2.6	2.4	19.8	14.9
16.0	13.8	3.2	2.4	17.0	19.0
19.5	9.7	4.0	3.5	13.7	23.1
24.4	7.5	8.3	4.8	15.8	24.4
29.7	3.2	7.9	5.8	11.1	27.6
34.6	2.2	12.9	7.7	15.0	35.7
39.4	-	-	8.4	11.5	42.0
59.5	-	-	11.0	11.9	50.6

Table B.9 Constants in polynomials used for curve-fitting the results of the steel rod impacting 8.1 mm alumina and 6.0 mm aluminium at 815 m/s

	rear-end positions	penetration	deformation	proj. length
a0	$0.3150 \cdot 10^2$	0.0	0.0	$0.3150 \cdot 10^2$
a1	$-0.8150 \cdot 10^0$	0.0	0.0	$-0.8150 \cdot 10^0$
a2	$-0.1024 \cdot 10^{-1}$	$0.3577 \cdot 10^{-2}$	$0.4711 \cdot 10^{-2}$	$0.5057 \cdot 10^{-3}$
a3	$0.7881 \cdot 10^{-3}$	$-0.2261 \cdot 10^{-4}$	$-0.6202 \cdot 10^{-4}$	$0.3382 \cdot 10^{-3}$
a4	$-0.1243 \cdot 10^{-4}$	0.0	0.0	$-0.4743 \cdot 10^{-5}$
a5	$0.6203 \cdot 10^{-7}$	0.0	0.0	$0.1922 \cdot 10^{-7}$

Table B.10 Constants in polynomials used for curve-fitting the results of the steel rod impacting 8.1 mm alumina and 6.0 mm aluminium at 916 m/s

	rear-end positions	penetration	deformation	proj. length
a0	$0.3150 \cdot 10^2$	0.0	0.0	$0.3150 \cdot 10^2$
a1	$-0.9160 \cdot 10^0$	0.0	0.0	$-0.9160 \cdot 10^0$
a2	$0.1448 \cdot 10^{-1}$	$0.1280 \cdot 10^{-1}$	$0.9199 \cdot 10^{-2}$	$0.2511 \cdot 10^{-1}$
a3	$-0.7417 \cdot 10^{-3}$	$-0.1634 \cdot 10^{-3}$	$-0.1003 \cdot 10^{-3}$	$-0.6286 \cdot 10^{-3}$
a4	$0.1779 \cdot 10^{-4}$	0.0	0.0	$0.8857 \cdot 10^{-5}$
a5	$-0.1274 \cdot 10^{-6}$	0.0	0.0	$-0.4551 \cdot 10^{-7}$

Table B.11 Constants in polynomials used for curve-fitting the results of the steel rod impacting 8.1 mm alumina and two 3.0 mm layers of aluminium at 819 m/s

	rear-end positions	penetration	deformation	proj. length
a0	$0.3150 \cdot 10^2$	0.0	0.0	$0.3150 \cdot 10^2$
a1	$-0.8190 \cdot 10^0$	0.0	0.0	$-0.8190 \cdot 10^0$
a2	$0.6966 \cdot 10^{-2}$	$0.3649 \cdot 10^{-2}$	$0.5447 \cdot 10^{-2}$	$0.1332 \cdot 10^{-1}$
a3	$-0.1920 \cdot 10^{-3}$	$-0.7862 \cdot 10^{-5}$	$-0.5968 \cdot 10^{-4}$	$-0.3672 \cdot 10^{-3}$
a4	$0.4731 \cdot 10^{-5}$	0.0	0.0	$0.7825 \cdot 10^{-5}$
a5	$-0.3507 \cdot 10^{-7}$	0.0	0.0	$-0.5258 \cdot 10^{-7}$

Table B.12 Constants in polynomials used for curve-fitting the results of the steel rod impacting 8.1 mm alumina and two 3.0 mm layers of aluminium at 938 m/s

	rear-end positions	penetration	deformation	proj. length
a0	$0.3150 \cdot 10^2$	0.0	0.0	$0.3150 \cdot 10^2$
a1	$-0.9380 \cdot 10^0$	0.0	0.0	$-0.9380 \cdot 10^0$
a2	$0.1387 \cdot 10^{-1}$	$0.1204 \cdot 10^{-1}$	$0.8549 \cdot 10^{-2}$	$0.2170 \cdot 10^{-1}$
a3	$-0.6287 \cdot 10^{-3}$	$-0.1400 \cdot 10^{-3}$	$-0.9075 \cdot 10^{-4}$	$-0.3791 \cdot 10^{-3}$
a4	$0.1424 \cdot 10^{-4}$	0.0	0.0	$0.4071 \cdot 10^{-5}$
a5	$-0.9415 \cdot 10^{-7}$	0.0	0.0	$-0.1712 \cdot 10^{-7}$

Table B.13 Constants in polynomials used for curve-fitting the results of the steel rod impacting 8.1 mm alumina and 4.0 mm aluminium at 786 m/s

	rear-end positions	penetration	deformation	proj. length
a0	$0.3150 \cdot 10^2$	0.0	0.0	$0.3150 \cdot 10^2$
a1	$-0.7860 \cdot 10^0$	0.0	0.0	$-0.7860 \cdot 10^0$
a2	$0.1146 \cdot 10^{-1}$	$0.3559 \cdot 10^{-2}$	$0.4173 \cdot 10^{-2}$	$0.8454 \cdot 10^{-2}$
a3	$-0.4457 \cdot 10^{-3}$	$-0.2670 \cdot 10^{-4}$	$-0.3762 \cdot 10^{-4}$	$-0.5921 \cdot 10^{-4}$
a4	$0.8867 \cdot 10^{-5}$	0.0	0.0	$0.9601 \cdot 10^{-6}$
a5	$-0.5386 \cdot 10^{-7}$	0.0	0.0	$-0.6335 \cdot 10^{-8}$

Table B.14 Constants in polynomials used for curve-fitting the results of the steel rod impacting 8.1 mm alumina and 4.0 mm aluminium at 829 m/s

	rear-end positions	penetration	deformation	proj. length
a0	$0.3150 \cdot 10^2$	0.0	0.0	$0.3150 \cdot 10^2$
a1	$-0.8290 \cdot 10^0$	0.0	0.0	$-0.8290 \cdot 10^0$
a2	$-0.7234 \cdot 10^{-3}$	$0.4450 \cdot 10^{-2}$	$0.4710 \cdot 10^{-2}$	$0.3905 \cdot 10^{-2}$
a3	$0.2529 \cdot 10^{-3}$	$-0.2316 \cdot 10^{-4}$	$-0.3803 \cdot 10^{-4}$	$0.2290 \cdot 10^{-3}$
a4	$-0.3398 \cdot 10^{-5}$	0.0	0.0	$-0.3566 \cdot 10^{-5}$
a5	$0.1307 \cdot 10^{-7}$	0.0	0.0	$0.1506 \cdot 10^{-7}$

Table B.15 Constants in polynomials used for curve-fitting the results of the steel rod impacting 8.1 mm alumina and 8.0 mm aluminium at 995 m/s

	rear-end positions	penetration	deformation	proj. length
a0	$0.3150 \cdot 10^2$	0.0	0.0	$0.3150 \cdot 10^2$
a1	$-0.9950 \cdot 10^0$	0.0	0.0	$-0.9950 \cdot 10^0$
a2	$0.1636 \cdot 10^{-1}$	$0.5239 \cdot 10^{-2}$	$0.4831 \cdot 10^{-2}$	$0.3125 \cdot 10^{-2}$
a3	$-0.1191 \cdot 10^{-2}$	$-0.5166 \cdot 10^{-4}$	$-0.5023 \cdot 10^{-4}$	$0.3615 \cdot 10^{-3}$
a4	$0.3529 \cdot 10^{-4}$	0.0	0.0	$-0.5481 \cdot 10^{-5}$
a5	$-0.2948 \cdot 10^{-6}$	0.0	0.0	$0.2316 \cdot 10^{-7}$

Table B.16 Constants in polynomials used for curve-fitting the results of the steel rod impacting 8.1 mm alumina and 8.0 mm aluminium at 1091 m/s

	rear-end positions	penetration	deformation	proj. length
a0	$0.3150 \cdot 10^2$	0.0	0.0	$0.3150 \cdot 10^2$
a1	$-0.1091 \cdot 10^1$	0.0	0.0	$-0.1091 \cdot 10^1$
a2	$-0.6754 \cdot 10^{-2}$	$0.1125 \cdot 10^{-1}$	$0.1061 \cdot 10^{-1}$	$0.1437 \cdot 10^{-1}$
a3	$0.6483 \cdot 10^{-3}$	$-0.2085 \cdot 10^{-4}$	$-0.1264 \cdot 10^{-3}$	$0.1291 \cdot 10^{-3}$
a4	$-0.8906 \cdot 10^{-5}$	0.0	0.0	$-0.3758 \cdot 10^{-5}$
a5	$0.1987 \cdot 10^{-7}$	0.0	0.0	$0.1925 \cdot 10^{-7}$

ANNEX C THE COMPLETE SET OF ALARM INPUT PARAMETERS

In this annex, a number of tables are presented which were used for the ALARM computations presented in this report.

Table C.1 Hilox-973 alumina properties

ceramic density	[kg/m ³]	3810.
bulk modulus	[N/m ²]	$0.242 \cdot 10^{12}$
elastic wave velocity	[m/s]	10820.

Table C.2 The steel rod projectile

length	[m]	0.0315
diameter	[m]	0.006
density	[kg/m ³]	7800
yield	[N/m ²]	$0.172 \cdot 10^{10}$
elastic wave velocity	[m/s]	500
plastic wave velocity	[m/s]	133

Table C.3 The ceramic rubble resistance parameters for Hilox-973

β		$0.1 \cdot 10^8$
γ		$0.135 \cdot 10^{10}$
r_{hole}	[m]	0.0030

Table C.4 Additional data used for ALARM computations, relating ceramic thickness and ceramic conoid angle to R, the radius of the section of back-up plate influenced by the impact, and $R_{\text{rigid}} (= \text{AKSIC} \cdot R)$, the initial position of the moving plastic hinge

H_c [m]	R [m]	AKSIC
0.0081	0.033	0.60

Table C.5 Modified aluminium properties for use with the ALARM model

H_b [m]	M_{plas} [N]	N [N/m]	Q [N/m]	fail [%]
0.0030	0465.0	0.093d+07	0.060d+07	0.13
0.0035	0632.9	0.109d+07	0.070d+07	0.13
0.0040	0826.7	0.124d+07	0.080d+07	0.13
0.0045	1093.3	0.143d+07	0.092d+07	0.13
0.0050	1291.7	0.155d+07	0.100d+07	0.13
0.0055	1562.9	0.171d+07	0.110d+07	0.13
0.0060	1860.0	0.186d+07	0.120d+07	0.13
0.0065	2182.9	0.202d+07	0.130d+07	0.13
0.0070	2531.7	0.217d+07	0.140d+07	0.13
0.0072	2678.4	0.223d+07	0.144d+07	0.13
0.0075	2906.3	0.233d+07	0.150d+07	0.13
0.0078	3143.4	0.242d+07	0.156d+07	0.13
0.0080	3306.7	0.248d+07	0.160d+07	0.13
0.0085	3732.9	0.264d+07	0.170d+07	0.13
0.0090	4185.0	0.279d+07	0.180d+07	0.13
0.0094	4565.3	0.291d+07	0.188d+07	0.13
0.0095	4662.9	0.295d+07	0.190d+07	0.13

with: N the normal load, Q the shearload and M_{plas} the bending moment per unit length along the periphery of a plate section.

Table C.6 Integration and general input parameters

input parameter	value
DELT	$0.125 \cdot 10^{-6}$
TEND	$0.200 \cdot 10^{-3}$
EBAR1	$0.250 \cdot 10^{-3}$
EBAR2	-
EBAR3	$0.100 \cdot 10^{-2}$
EBAR4	$0.100 \cdot 10^{-3}$
EBAR5	-

The ALARM input-deck such as the one presented below for the ballistic limit computation of a lightweight armour consisting of an 8.1 mm Al_2O_3 (Hilox-973) facing supported by a 6.0 mm thick aluminium 6061-T6 back-up plate can be constructed from the data given above.

balrod hc= 8.1 mm hb= 6.0 mm

.00810 3.810E+03 3.330E-02 6.000E-01 1.000E+00 2.420E+11 1.082E+04 0.000E+00

1

.00600 2.705E+03 1.860E+03 1.860E+06 1.200E+06 1.300E-01

.03150 .00600 7.800E+03 .99 5.000E+02 1.330E+02 9.050E+02 1.725E+09 3.000E-03

1.250E-07 2.000E-04 2.500E-04 2.500E+01 1.000E-03 1.000E-04 1.500E+00

50 200 0

2

1 0.000E+00 0.000E+00 1.000E+07 1.350E+09

REPORT DOCUMENTATION PAGE

(MOD NL)

1. DEFENSE REPORT NUMBER (MOD-NL) TD91-1682	2. RECIPIENT'S ACCESSION NUMBER	3. PERFORMING ORGANIZATION REPORT NUMBER PML1991-28
4. PROJECT/TASK/WORKUNIT NO. 253391142	5. CONTRACT NUMBER -	6. REPORT DATE January 1993
7. NUMBER OF PAGES 104 (3 Annexes)	8. NUMBER OF REFERENCES 50	9. TYPE OF REPORT AND DATES COVERED Final
10. TITLE AND SUBTITLE An experimental and analytical study on the penetration of rods into ceramic faced armours. (Een experimentele en analytische studie naar het penetratieproces van staven in keramische pantsers.)		
11. AUTHOR(S) Paul C. den Reijer		
12. PERFORMING ORGANIZATION NAME(S) AND ADDRESS(ES) TNO Prins Maurits Laboratory P.O. Box 45, 2280 AA Rijswijk, The Netherlands		
13. SPONSORING AGENCY NAME(S) AND ADDRESS(ES)		
14. SUPPLEMENTARY NOTES Ongerubriceerd is equivalent to: Unclassified		
15. ABSTRACT (MAXIMUM 200 WORDS (1044 BYTE)) AKZO's ballistic Arall programme has led to the development of an analytic lightweight armour response model (ALARM) which can be used to predict the behaviour of these armour systems when impacted by various projectiles. In order to verify and improve the understanding of phenomena governing the projectile-armour interaction process, an experimental programme was proposed and set up. This report deals with the second and final phase of this programme. The impact of steel rod projectiles into four types of ceramic faced armours with velocities above and below the armour's ballistic limit velocity is studied using a flash X-ray technique. The experimental results are discussed extensively and compared with the ALARM model predictions. Recommendations for future improvement of the analytic model and for experimental research on ceramic faced armours are presented too.		
16. DESCRIPTORS Ceramics Penetration Armour Piercing Projectiles Impact Experimental Investigation Radiography Comparison		IDENTIFIERS Lightweight Armour
17A. SECURITY CLASSIFICATION (OF REPORT) ONGERUBRICEERD	17B. SECURITY CLASSIFICATION (OF PAGE) ONGERUBRICEERD	17C. SECURITY CLASSIFICATION (OF ABSTRACT) ONGERUBRICEERD
18. DISTRIBUTION AVAILABILITY STATEMENT Unlimited Distribution		17D. SECURITY CLASSIFICATION (OF TITLES) ONGERUBRICEERD

Distributielijst

- 1 DWOO
- 2 HWO-KL
- 3/4 HWO-KLu
- 5 HWO-KM
- 6/11 AKZO Vezels en Polymeren Divisie, Jhr. Drs. E.W.A. Albarda van Ekenstein
- 12/14 TDCK
- 15 Hoofddirecteur DO-TNO
- 16 Lid Instituuts Advies Raad PML
Prof. drs. P.J. van den Berg
- 17 Lid Instituuts Advies Raad PML
Prof. ir. M.A.W. Scheffelaar
- 18 Lid Instituuts Advies Raad PML
Prof. ir. H. Wittenberg
- 19 PML-TNO, Directeur; daarna reserve
- 20 PML-TNO, Directeur Programma; daarna reserve
- 21/22 PML-TNO, Divisie Wapens en Platforms, Ballistiek
- 23 Dr. P.C. den Reijer
- 24 PML-TNO, Documentatie
- 25 PML-TNO, Archief